DESIGN AND EXPERIMENTAL INVESTIGATION OF A WIND TUNNEL GUST GENERATOR

A THESIS SUBMITTED TO
THE GRADUATE SCHOOL OF NATURAL AND APPLIED SCIENCES
OF
MIDDLE EAST TECHNICAL UNIVERSITY

BY

İMGE YIĞILI

IN PARTIAL FULFILLMENT OF THE REQUIREMENTS
FOR
THE DEGREE OF MASTER OF SCIENCE
IN
AEROSPACE ENGINEERING

SEPTEMBER 2022

Approval of the thesis:

DESIGN AND EXPERIMENTAL INVESTIGATION OF A WIND TUNNEL GUST GENERATOR

submitted by **İMGE YIĞILI** in partial fulfillment of the requirements for the degree of **Master of Science in Aerospace Engineering Department, Middle East Technical University** by,

Prof. Dr. Halil Kalıpçılar
Dean, Graduate School of **Natural and Applied Sciences** _____

Prof. Dr. Serkan Özgen
Head of Department, **Aerospace Engineering** _____

Assist. Prof. Dr. Mustafa Perçin
Supervisor, **Aerospace Engineering, METU** _____

Examining Committee Members:

Prof. Dr. Sinan Eyi
Aerospace Engineering, METU _____

Assist. Prof. Dr. Mustafa Perçin
Aerospace Engineering, METU _____

Prof. Dr. Oğuz Uzol
Aerospace Engineering, METU _____

Assoc. Prof. Dr. Münir Elfarra
Aerospace Engineering, Ankara YBU _____

Assist. Prof. Dr. Onur Baş
Mechanical Engineering, TEDU _____

Date: 01.09.2022

I hereby declare that all information in this document has been obtained and presented in accordance with academic rules and ethical conduct. I also declare that, as required by these rules and conduct, I have fully cited and referenced all material and results that are not original to this work.

Name, Surname: İmge Yığılı

Signature :

ABSTRACT

DESIGN AND EXPERIMENTAL INVESTIGATION OF A WIND TUNNEL GUST GENERATOR

Yığılı, İmge
M.S., Department of Aerospace Engineering
Supervisor: Assist. Prof. Dr. Mustafa Perçin

September 2022, 129 pages

In the design, certification and operation cycles of air vehicles, wind turbines, etc., it is critically important to quantitatively demonstrate the capability of the vehicle to withstand any environmental and meteorological condition. Of several atmospheric conditions, one very common and significant one is the atmospheric gust. Therefore, capacity to generate gust in a fully controlled manner is of utmost importance. In wind tunnels, gust generation is done by means of gust generators, which are devices positioned upstream of the wind tunnel test sections to produce gusts of desired profiles and magnitudes. In this context, the focus of this thesis is the design and manufacturing of a double vane gust generator and investigation of the changes in the flow field with different actuation parameters and distance between the gust vanes. One novel contribution of this study to existing work is that full field information is obtained by using Particle Image Velocimetry technique instead of using pointwise measurement techniques such as hot wire anemometry. Spatial and temporal behavior of the gust flow for various actuation parameters and vane spacing values are explored and presented in this thesis. Experimental results are compared to numerical results and computational investigation of the gust generator is also shown. Finally, as an

application, a porous disk and a model wind turbine that have the same thrust coefficient are positioned downstream of the gust generator. Wake flows of the two models are then compared under a transverse gust loading and the capacity of the porous disk in mimicking the wind turbine wake under a gusty inflow condition is tested. Outcomes of this study will serve as a starting point for a gust generator which will be placed in the Large Scale Wind Tunnel of METU Center for Wind Energy Research (RÜZGEM).

Keywords: Gust Generation, Wind Tunnel, Particle Image Velocimetry

ÖZ

RÜZGAR TÜNELİ SAĞANAK AKIŞ ÜRETECİ TASARIMI VE DENEYSEL İNCELEMESİ

Yığılı, İmge
Yüksek Lisans, Havacılık ve Uzay Mühendisliği Bölümü
Tez Yöneticisi: Dr. Öğr. Üyesi. Mustafa Perçin

Eylül 2022 , 129 sayfa

Hava araçları, rüzgar türbinleri, vb. tasarımı, sertifikasyonu ve operasyon döngülerinde, aracın herhangi bir çevresel ve meteorolojik koşula dayanıklılığını göstermek kritik bir öneme sahiptir. Birçok atmosferik koşul arasında en yaygın ve önemlilerinden biri ise atmosferik sağanaktır. Dolayısıyla, tamamen kontrollü bir ortam ve biçimde sağanak üretebilmek oldukça önemlidir. Rüzgar tünellerinde sağanak akış üretimi, test kesitinin girişine konan ve istenilen büyüklük ve profilde sağanak üreten sağanak akış üreteçleri vasıtasıyla yapılmaktadır. Bu bağlamda, bu tezin odağı iki kanatçıklı bir sağanak akış üretecinin tasarımı, üretimi ve değişen hareket parametreleri ve kanatçıklar arası mesafe ile akış alanının değişiminin incelenmesidir. Bu çalışmanın varolan çalışmalara katkısı, diğer çalışmalarda kullanılan sıcak tel anemometresi gibi tek noktalı ölçüm teknikleri yerine tüm alan bilgisinin Parçacık Görüntülemeli Hız Ölçme tekniği ile elde edilmesidir. Sağanak akışın uzay ve zamandaki davranışı, farklı hareket parametreleri ve kanatçık arası mesafelerde incelenmiş, sonuçlar bu tezde gösterilmiştir. Sağanak akış üretecinin hesaplamalı analizleri yapılmış, deneysel sonuçlar nümerik sonuçlarla karşılaştırılmıştır. Son olarak, sağanak akış üretecinin

uygulaması aynı itme katsayısına sahip delikli bir disk ve model türbin üzerinde yapılmıştır. İki modelin iz bölgesi akışa dik sağanak altında karşılaştırılmış, delikli diskin model türbine benzer bir iz bölgesi oluşturma kapasitesi bu koşullar altında test edilmiştir. Bu çalışmanın sonuçları RÜZGEM Büyük Rüzgar Tüneli için bir sağanak akış üreteci tasarım ve üretimi için bir başlangıç noktası olarak kullanılacaktır.

Anahtar Kelimeler: Sağanak Akış Üreteci, Rüzgar Tüneli, Parçacık Görüntülemeli Hız Ölçme

To all the women struggling in this man's world

ACKNOWLEDGMENTS

To begin with, I would like to express my deepest gratitude to my supervisor Assist. Prof. Dr. Mustafa Perçin, who tirelessly guided me through this journey. Thanks to his energy, patience and invaluable experience, this work is completed. Also, without the support, enthusiasm and vision of Prof. Dr. Oğuz Uzol, this work would have been far deficient compared to what it is now. These two instructors changed my point of view thoroughly and helped this academic journey finally come to an end.

I wish to thank all my colleagues for the unforgettable, sleepless nights at RÜZGEM Aerolab. Without the support and friendship we had, I for sure would give up. Thanks to Dr. Anas Abdulrahim, who introduced me to experimental aerodynamics practises and has been there for me all the time, and never hesitated to come to the lab even in curfew days. Thanks to M. Tuğrul Akpolat, for sharing his experience in PIV with me, although not with patience, but with an enlightening technical competency. Thanks to Mert Ali Andırın, Buğrahan Öztürk and Burcu Erol, with whom we have started this journey as colleagues, but ended up as close friends with lots of memories of tears, blood and joy. Last but not least, thanks to all the crew in RÜZGEM, who offered help, experience and astonishing ideas.

Finally, I am more than grateful to have two amazing people as my parents, Aliye and Ahmet Yığılı, without whose never-failing sympathy, love and encouragement, this thesis would not even exist. They are the sole reason of my dreams, goals and will to keep going.

TABLE OF CONTENTS

ABSTRACT v

ÖZ vii

ACKNOWLEDGMENTS x

TABLE OF CONTENTS xi

LIST OF TABLES xiv

LIST OF FIGURES xv

LIST OF ABBREVIATIONS xxvii

CHAPTERS

1 INTRODUCTION 1

1.1 Overview of Gust Problem 1

1.2 Certification Requirements 5

1.3 Gust Generator Design 8

1.4 Computational Investigation of Gust Generators 16

1.5 An Application Regarding Wind Turbines: Porous Disk Approach . . 18

1.6 Objectives and Scope of the Thesis 19

2 METHODOLOGY 21

2.1 Wind Tunnel 21

2.2 Gust Generator 21

2.2.1 Conceptual Design of the Gust Generator 22
2.2.1.1 Design of the Gust Vanes 22
2.2.1.2 Motor Sizing 24
2.2.1.3 Design of the Frame 25
2.2.2 CFD Analyses of the Gust Generator 26
2.2.2.1 Validation of the CFD Methodology 29
2.2.2.2 CFD Analyses for the Characterization of the Gust Generator 30
2.2.3 Experimental Investigation of the Gust Generator 31
2.2.3.1 Flow Field Measurements via Particle Image Velocimetry 33
2.2.3.2 Measurement Procedure 35
2.2.3.3 Data Analysis 36
2.2.3.4 Uncertainty Analysis 36
2.3 Application 37
3 RESULTS AND DISCUSSION 41
3.1 Variations in the Gust Ratio 42
3.2 Comparison of Numerical and Experimental Results 46
3.3 Spatial Variations in the Flow Field 50
3.3.1 Effect of Reduced Frequency 50
3.3.1.1 Effect of the Pitching Frequency 54
3.3.1.2 Effect of the Freestream Velocity 61
3.3.2 Effect of the Vane Spacing 64
3.3.3 Effect of the Pitching Amplitude 67

3.4 Temporal Variations in the Flow Field 70
3.4.1 Effect of Reduced Frequency 71
3.4.1.1 Effect of the Pitching Frequency 72
3.4.1.2 Effect of the Freestream Velocity 75
3.4.2 Effect of the Vane Spacing 77
3.4.3 Effect of the Maximum Pitching Amplitude 78
3.5 An Application Regarding Wind Turbines: Porous Disk Approach . . 79
3.5.1 Comparison of the Uniform Inflow Case and Average of the Phases 83
4 CONCLUSION AND FUTURE WORK 87
REFERENCES 91
APPENDICES
A CONTOUR PLOTS OF ALL TEST CASES 97

LIST OF TABLES

TABLES

Table 1.1 Gust vane parameters of vane-type gust generator setups 14

Table 1.2 Actuation parameters of vane-type gust generator setups 15

Table 1.3 Actuation parameters of vane-type gust generator setups 15

Table 2.1 Properties of the grids 27

Table 2.2 Test matrix 32

Table 2.3 PIV experimental parameters 34

Table 2.4 Properties of the models 38

Table 3.1 RMS normalized by the freestream velocity of the difference of wake velocity distributions of the porous disk and the model turbine 82

LIST OF FIGURES

FIGURES

Figure 1.1 Three categories of discrete gust encounters [6]. 2

Figure 1.2 Downwash induced by the gust [9]. 3

Figure 1.3 Küssner's model [5]. 4

Figure 1.4 Duhamel superposition applied to an arbitrary gust shape [5]. . . 4

Figure 1.5 Flight envelope limited by gust loading [13]. 6

Figure 1.6 Gust ratios experienced by vehicles and animals for different atmospheric conditions [24]. 7

Figure 1.7 Extreme operating gust (EOG). $N = 1$, where N is the period in years, rotor diameter is 42 m, hub height is 30 m and hub velocity is 25 m/s [22]. 7

Figure 1.8 Gust generator designed for the Open Jet Facility in Deft University of Technology [28]. 9

Figure 1.9 Disturbance generator mounted in the wind tunnel contraction in Virginia Tech Stability Wind Tunnel [30]. 10

Figure 1.10 Conceptual sketch of the gust generator built for the large wind tunnel at the University of Bath [32]. 11

Figure 1.11 Gust generator located at the S3Ch transonic wind tunnel at ONERA [16]. 12

Figure 1.12 Schematic of the apparatus and the experimental setup [16]. . . . 12

Figure 1.13 Schematic of the test section [33]. 13

Figure 1.14 Technical drawing of the 2D active grid, i.e., gust generator [34]. 14

Figure 1.15 Extent of the gust vane tip wake when the gust vanes are not full span. There is a 70 mm gap at both walls resulting in a wake flow that extends up to 400 mm from the wall [27]. 16

Figure 1.16 Structured 2D mesh grid [28]. 17

Figure 1.17 Boundary conditions and mesh grid [36]. 17

Figure 1.18 Results of the magnitude of flow velocity for the case when the airfoils are at 10° of angle of attack [36]. 18

Figure 1.19 Two porous disk models based on the simplest wind turbine model: the actuator disk concept [43]. 19

Figure 2.1 Wind tunnel parts and definition of the coordinate system. 22

Figure 2.2 The maximum gust angle measured for different chord lengths [28]. 24

Figure 2.3 CAD drawing of the gust generator system. Side, front and isometric views respectively. 25

Figure 2.4 Gust generator integrated into the entrance of the test section of the C1 wind tunnel at RÜZGEM. 26

Figure 2.5 Boundary conditions, domain specifications (top), and mesh grid used in the simulations (bottom). 26

Figure 2.6 Grid convergence study performed with three grids of different sizes. 27

Figure 2.7 Results of the time-step convergence study. 28

Figure 2.8 Turbulence model convergence study performed with three different turbulence models. 28

Figure 2.9 CFD results of the gust generator in the Open Jet Facility in Delft University obtained via the current methodology (left) and the study [28] (right). Full line in the right plot stands for the case with $d = 0.7\ m$. $c = 0.3$ m, $V_{ref} = 25$ m/s, $f = 5$ Hz and $\delta_{max} = \pm 10°$. . . . 29

Figure 2.10 Comparison of the experimental and CFD results demonstrated in [28]. 30

Figure 2.11 The maximum gust ratio values 3 chords downstream of the trailing edge of the gust vanes for different reduced frequencies. 31

Figure 2.12 Sampling point locations demonstrated on a period of motion. . . 32

Figure 2.13 PIV measurement setup. 33

Figure 2.14 PIV measurement domain showing the windows with the overlap region and the field of view dimensions. 35

Figure 2.15 The model wind turbine (left) and the porous disk (right). 37

Figure 2.16 PIV measurement domain showing the windows with the overlap region and the field of view dimensions. 38

Figure 3.1 Maximum transverse and streamwise gust ratio values at $x/c = 3$ for different reduced frequencies. Effect of varying pitching frequency and freestream velocity while other actuation parameters are identical, are also shown. 43

Figure 3.2 Maximum transverse and streamwise gust ratio values at $x/c = 2$ for different reduced frequencies. Effect of varying pitching frequency and freestream velocity while other actuation parameters are identical, are also shown. 44

Figure 3.3 Maximum transverse and streamwise gust ratio values at $x/c = 3$ for different Strouhal numbers. Effect of varying pitching amplitude and vane spacing while other actuation parameters are identical, are also shown. 45

Figure 3.4 Maximum transverse and streamwise gust ratio values at $x/c = 2$ for different Strouhal numbers. Effect of varying pitching amplitude and vane spacing while other actuation parameters are identical, are also shown. 46

Figure 3.5 Streamwise and transverse gust ratio values at each phase of the period obtained by numerical and experimental studies. 47

Figure 3.6 Contours of transverse velocity component (v-velocity) obtained via CFD runs (left) and PIV measurements (right), for the phase when $\theta = 0^\circ$ for the baseline case. 47

Figure 3.7 Contours of transverse velocity component (v-velocity) obtained via CFD runs (left) and PIV measurements (right), for the phase when $\theta = 12^\circ$ for the baseline case. 48

Figure 3.8 Contours of transverse velocity component (v-velocity) obtained via CFD runs (left) and PIV measurements (right), for the phase when $\theta = 0^\circ$ for the baseline case. 48

Figure 3.9 Contours of transverse velocity component (v-velocity) obtained via CFD runs (left) and PIV measurements (right), for the phase when $\theta = -12^\circ$ for the baseline case. 49

Figure 3.10 Effect of different actuation parameters and the same reduced frequency on the streamwise component of velocity. Columns represent the test cases for which frequency is different and other parameters are identical. Rows represent the phase angle of the period. One period of motion starts from 0°, peaks at θ_{max}, becomes 0° again and goes to minimum (θ_{min}). 51

Figure 3.11 Effect of different actuation parameters and the same reduced frequency on the transverse component of velocity. Columns represent the test cases for which frequency is different and other parameters are identical. Rows represent the phase angle of the period. One period of motion starts from 0°, peaks at θ_{max}, becomes 0° again and goes to minimum (θ_{min}). 52

Figure 3.12 Effect of different actuation parameters and the same reduced frequency on out-of-plane vorticity. Columns represent the test cases for which frequency is different and other parameters are identical. Rows represent the phase angle of the period. One period of motion starts from 0°, peaks at θ_{max}, becomes 0° again and goes to minimum (θ_{min}). 53

Figure 3.13 Effect of pitching frequency on the streamwise component of velocity. Columns represent the test cases for which frequency is different and other parameters are identical. Rows represent the phase angle of the period. One period of motion starts from 0°, peaks at θ_{max}, becomes 0° again and goes to minimum (θ_{min}). 55

Figure 3.14 Effect of pitching frequency on the streamwise component of velocity. Columns represent the test cases for which frequency is different and other parameters are identical. Rows represent the phase angle of the period. One period of motion starts from 0°, peaks at θ_{max}, becomes 0° again and goes to minimum (θ_{min}). 56

Figure 3.15 Effect of pitching frequency on the transverse component of velocity. Columns represent the test cases for which frequency is different and other parameters are identical. Rows represent the phase angle of the period. One period of motion starts from 0°, peaks at θ_{max}, becomes 0° again and goes to minimum (θ_{min}). 57

Figure 3.16 Effect of pitching frequency on the transverse component of velocity. Columns represent the test cases for which frequency is different and other parameters are identical. Rows represent the phase angle of the period. One period of motion starts from 0°, peaks at θ_{max}, becomes 0° again and goes to minimum (θ_{min}). 58

Figure 3.17 Effect of pitching frequency on vorticity. Columns represent the test cases for which frequency is different and other parameters are identical. Rows represent the phase angle of the period. One period of motion starts from 0°, peaks at θ_{max}, becomes 0° again and goes to minimum (θ_{min}). 59

Figure 3.18 Effect of pitching frequency on vorticity. Columns represent the test cases for which frequency is different and other parameters are identical. Rows represent the phase angle of the period. One period of motion starts from 0°, peaks at θ_{max}, becomes 0° again and goes to minimum (θ_{min}). 60

Figure 3.19 Effect of freestream velocity on the streamwise component of velocity. Columns represent the test cases for which frequency is different and other parameters are identical. Rows represent the phase angle of the period. One period of motion starts from 0°, peaks at θ_{max}, becomes 0° again and goes to minimum (θ_{min}). 61

Figure 3.20 Effect of freestream velocity on the transverse component of velocity. Columns represent the test cases for which frequency is different and other parameters are identical. Rows represent the phase angle of the period. One period of motion starts from 0°, peaks at θ_{max}, becomes 0° again and goes to minimum (θ_{min}). 62

Figure 3.21 Effect of freestream velocity on vorticity. Columns represent the test cases for which frequency is different and other parameters are identical. Rows represent the phase angle of the period. One period of motion starts from 0°, peaks at θ_{max}, becomes 0° again and goes to minimum (θ_{min}). 64

Figure 3.22 Effect of vane spacing on the streamwise component of velocity. Columns represent the test cases for which frequency is different and other parameters are identical. Rows represent the phase angle of the period. One period of motion starts from 0°, peaks at θ_{max}, becomes 0° again and goes to minimum (θ_{min}). 65

Figure 3.23 Effect of vane spacing on the transverse component of velocity. Columns represent the test cases for which frequency is different and other parameters are identical. Rows represent the phase angle of the period. One period of motion starts from 0°, peaks at θ_{max}, becomes 0° again and goes to minimum (θ_{min}). 66

Figure 3.24 Effect of vane spacing on vorticity. Columns represent the test cases for which frequency is different and other parameters are identical. Rows represent the phase angle of the period. One period of motion starts from 0°, peaks at θ_{max}, becomes 0° again and goes to minimum (θ_{min}). 67

Figure 3.25 Effect of maximum amplitude on the streamwise component of velocity. Columns represent the test cases for which frequency is different and other parameters are identical. Rows represent the phase angle of the period. One period of motion starts from 0°, peaks at θ_{max}, becomes 0° again and goes to minimum (θ_{min}). 68

Figure 3.26 Effect of maximum amplitude on the transverse component of velocity. Columns represent the test cases for which frequency is different and other parameters are identical. Rows represent the phase angle of the period. One period of motion starts from 0°, peaks at θ_{max}, becomes 0° again and goes to minimum (θ_{min}). 69

Figure 3.27 Effect of maximum amplitude on vorticity. Columns represent the test cases for which frequency is different and other parameters are identical. Rows represent the phase angle of the period. One period of motion starts from 0°, peaks at θ_{max}, becomes 0° again and goes to minimum (θ_{min}). 70

Figure 3.28 Streamwise and transverse gust ratio values at each phase of the period for the baseline case. 71

Figure 3.29 Streamwise and transverse gust ratio values at each phase of the period for the two cases with the same reduced frequency, but different actuation parameters. 72

Figure 3.30 Streamwise and transverse gust ratio values at each phase of the period. Each line represents a case where pitching frequency is altered and other actuation parameters are identical. ($U_\infty = 10$ m/s, $d = 2c$ and $\bar{\theta} = 12°$.) 72

Figure 3.31 Transverse gust ratio values at each phase of the period. Dashed lines with symbols correspond to experimental data, while solid line corresponds to CFD results. ($f = 2.5$ Hz, $U_\infty = 10$ m/s, $d = 2c$ and $\bar{\theta} = 12°$.) 73

Figure 3.32 Streamwise and transverse gust ratio values at each phase of the period. Each line represents a case where pitching frequency is altered and other actuation parameters are identical. ($U_\infty = 10$ m/s, $d = 2c$ and $\bar{\theta} = 12°$.) 73

Figure 3.33 Transverse gust ratio values at each phase of the period obtained via CFD runs. Each line represents a case where pitching frequency is altered and other actuation parameters are identical. ($U_\infty = 10$ m/s, $d = 2c$ and $\bar{\theta} = 12°$.) 74

Figure 3.34 Imaginary and real parts of the Theodorsen function [50]. 75

Figure 3.35 Streamwise and transverse gust ratio values at each phase of the period. Each line represents a case where freestream velocity is altered and other actuation parameters are identical. ($f = 10$ Hz, $d = 2c$ and $\bar{\theta} = 12°$.) 76

Figure 3.36 Transverse gust ratio values at each phase of the period obtained via CFD runs. Each line represents a case where freestream velocity is altered and other actuation parameters are identical. ($f = 10$ Hz, $d = 2c$ and $\bar{\theta} = 12°$.) 76

Figure 3.37 Streamwise and transverse gust ratio values at each phase of the period. Each line represents a case where vane spacing is altered and other actuation parameters are identical. ($U_\infty = 10$ m/s, $f = 10$ Hz and $\bar{\theta} = 12°$.) 77

Figure 3.38 Streamwise and transverse gust ratio values at each phase of the period. Each line represents a case where maximum pitching amplitude is altered and other actuation parameters are identical. ($U_\infty = 10$ m/s, $f = 10$ Hz and $d = 2c$.) 78

Figure 3.39 Left column: Porous disk under uniform flow, porous disk under gusty inflow. Right column: Model turbine under uniform flow, model turbine under gusty inflow. Gust vanes are at 0°, 12°, 0° and -12° angle of attack, respectively. 79

Figure 3.40 Wake deficit comparisons in terms of non-dimensional velocity at different x/D locations ($x/D = 1, 2, 3, 4$) under uniform and gusty inflow conditions at different phase angles for both porous disk (PD) and model turbine (MT). 81

Figure 3.41 Wake centerline dynamics of the porous disk and the model turbine subjected to gusty inflow. α represents the phases of the sinusoidal motion of the vanes. 82

Figure 3.42 Non-dimensional streamwise velocity contours of the porous disk under uniform inflow (left) and the average of the phases of the motion of the gust vanes (right). 83

Figure 3.43 Wake deficit comparisons in terms of non-dimensional velocity at different x/D locations ($x/D = 1, 2, 3, 4$) under uniform inflow condition and average of the phases of the motion of the gust vanes for the porous disk. 84

Figure 3.44 Non-dimensional streamwise velocity contours of the model turbine under uniform inflow (left) and the average of the phases of the motion of the gust vanes (right). 84

Figure 3.45 Wake deficit comparisons in terms of non-dimensional velocity at different x/D locations ($x/D = 1, 2, 3, 4$) under uniform inflow condition and average of the phases of the motion of the gust vanes for the model turbine. 85

Figure A.1 PIV measurement results for the case $f = 2.5$ Hz, $U_\infty = 10$ m/s, $d = 2c$, $\bar{\theta} = 12°$. Variation of streamwise velocity component. 97

Figure A.2 PIV measurement results for the case $f = 2.5$ Hz, $U_\infty = 10$ m/s, $d = 2c$, $\bar{\theta} = 12°$. Variation of transverse velocity component. 98

Figure A.3 PIV measurement results for the case $f = 2.5$ Hz, $U_\infty = 10$ m/s, $d = 2c$, $\bar{\theta} = 12°$. Variation of vorticity. 99

Figure A.4 PIV measurement results for the case $f = 5$ Hz, $U_\infty = 10$ m/s, $d = 2c$, $\bar{\theta} = 12°$. Variation of streamwise velocity component. 100

Figure A.5 PIV measurement results for the case $f = 5$ Hz, $U_\infty = 10$ m/s, $d = 2c$, $\bar{\theta} = 12°$. Variation of transverse velocity component. 101

Figure A.6 PIV measurement results for the case $f = 5$ Hz, $U_\infty = 10$ m/s, $d = 2c$, $\bar{\theta} = 12°$. Variation of vorticity. 102

Figure A.7 PIV measurement results for the case $f = 7.5$ Hz, $U_\infty = 10$ m/s, $d = 2c$, $\bar{\theta} = 12°$. Variation of streamwise velocity component. 103

Figure A.8 PIV measurement results for the case $f = 7.5$ Hz, $U_\infty = 10$ m/s, $d = 2c$, $\bar{\theta} = 12°$. Variation of transverse velocity component. 104

Figure A.9 PIV measurement results for the case $f = 7.5$ Hz, $U_\infty = 10$ m/s, $d = 2c$, $\bar{\theta} = 12°$. Variation of vorticity. 105

Figure A.10 PIV measurement results for the case $f = 10$ Hz, $U_\infty = 5$ m/s, $d = 2c$, $\bar{\theta} = 12°$. Variation of streamwise velocity component. 106

Figure A.11 PIV measurement results for the case $f = 10$ Hz, $U_\infty = 5$ m/s, $d = 2c$ $\bar{\theta} = 12°$. Variation of transverse velocity component. 107

Figure A.12 PIV measurement results for the case $f = 10$ Hz, $U_\infty = 5$ m/s, $d = 2c$ $\bar{\theta} = 12°$. Variation of vorticity. 108

Figure A.13 PIV measurement results for the case $f = 10$ Hz, $U_\infty = 10$ m/s, $d = 2c$, $\bar{\theta} = 12°$ (baseline case). Variation of streamwise velocity component. 109

Figure A.14 PIV measurement results for the case $f = 10$ Hz, $U_\infty = 10$ m/s, $d = 2c$, $\bar{\theta} = 12°$ (baseline case). Variation of transverse velocity component. 110

Figure A.15 PIV measurement results for the case $f = 10$ Hz, $U_\infty = 10$ m/s, $d = 2c$, $\bar{\theta} = 12°$ (baseline case). Variation of vorticity. 111

Figure A.16 PIV measurement results for the case $f = 10$ Hz, $U_\infty = 15$ m/s, $d = 2c$ $\bar{\theta} = 12°$. Variation of streamwise velocity component. 112

Figure A.17 PIV measurement results for the case $f = 10$ Hz, $U_\infty = 15$ m/s, $d = 2c$ $\bar{\theta} = 12°$. Variation of transverse velocity component. 113

Figure A.18 PIV measurement results for the case $f = 10$ Hz, $U_\infty = 15$ m/s, $d = 2c$ $\bar{\theta} = 12°$. Variation of vorticity. 114

Figure A.19 PIV measurement results for the case $f = 10$ Hz, $U_\infty = 10$ m/s, $d = 1c$ $\bar{\theta} = 12°$. Variation of streamwise velocity component. 115

Figure A.20 PIV measurement results for the case $f = 10$ Hz, $U_\infty = 15$ m/s, $d = 1c$ $\bar{\theta} = 12°$. Variation of transverse velocity component. 116

Figure A.21 PIV measurement results for the case $f = 10$ Hz, $U_\infty = 15$ m/s, $d = 1c$ $\bar{\theta} = 12°$. Variation of vorticity. 117

Figure A.22 PIV measurement results for the case $f = 10$ Hz, $U_\infty = 10$ m/s, $d = 2.5c$, $\bar{\theta} = 12°$. Variation of streamwise velocity component. 118

Figure A.23 PIV measurement results for the case $f = 10$ Hz, $U_\infty = 15$ m/s, $d = 2.5c$, $\bar{\theta} = 12°$. Variation of transverse velocity component. 119

Figure A.24 PIV measurement results for the case $f = 10$ Hz, $U_\infty = 15$ m/s, $d = 2.5c$, $\bar{\theta} = 12°$. Variation of vorticity. 120

Figure A.25 PIV measurement results for the case $f = 10$ Hz, $U_\infty = 10$ m/s, $d = 2c$, $\bar{\theta} = 8°$. Variation of streamwise velocity component. 121

Figure A.26 PIV measurement results for the case $f = 10$ Hz, $U_\infty = 15$ m/s, $d = 2c$, $\bar{\theta} = 8°$. Variation of transverse velocity component. 122

Figure A.27 PIV measurement results for the case $f = 10$ Hz, $U_\infty = 15$ m/s, $d = 2c$, $\bar{\theta} = 8°$. Variation of vorticity. 123

Figure A.28 PIV measurement results for the case $f = 10$ Hz, $U_\infty = 10$ m/s, $d = 2c$, $\bar{\theta} = 16°$. Variation of streamwise velocity component. 124

Figure A.29 PIV measurement results for the case $f = 10$ Hz, $U_\infty = 15$ m/s, $d = 2c$, $\bar{\theta} = 16°$. Variation of transverse velocity component. 125

Figure A.30 PIV measurement results for the case $f = 10$ Hz, $U_\infty = 15$ m/s, $d = 2c$, $\bar{\theta} = 16°$. Variation of vorticity. 126

Figure A.31 PIV measurement results for the case $f = 5$ Hz, $U_\infty = 5$ m/s, $d = 2c$, $\bar{\theta} = 12°$. Variation of streamwise velocity component. 127

Figure A.32 PIV measurement results for the case $f = 5$ Hz, $U_\infty = 5$ m/s, $d = 2c$, $\bar{\theta} = 12°$. Variation of transverse velocity component. 128

Figure A.33 PIV measurement results for the case $f = 5$ Hz, $U_\infty = 5$ m/s, $d = 2c$, $\bar{\theta} = 12°$. Variation of vorticity. 129

LIST OF ABBREVIATIONS

w_a	downwash velocity
w_g	gust velocity
x	position in streamwise direction
U_∞	freestream velocity
t	time
b	half chord length
k	reduced frequency
ω	circular frequency
f	motion frequency
c	chord length
K	Küssner response function
s	distance penetrated in gust
GR	gust ratio
u	streamwise velocity component
v	transverse velocity component
2D	two-dimensional
2C	two-component
MAV	micro air vehicle
CFD	Computational Fluid Dynamics
PIV	Particle Image Velocimetry
2D2C	two dimensional two component
D	diameter
α	angle of attack
d	distance between the vanes

I	moment of inertia
θ	angular position
$\bar{\theta}$	amplitude of motion
TTL	Transistor-Transistor-Logic
FOV	Field of View
St	Strouhal number
L	characteristic length
ζ	out-of-plane vorticity
C_T	thrust coefficient
RMS	root mean square

CHAPTER 1

INTRODUCTION

Quantitative specification of the environment in which the airplanes, micro air vehicles, wind turbines, etc. are intended to operate is critically important in the design, certification and operation cycles of the vehicle. Environmental and meteorological conditions are known to have a significant influence on aviation safety. Of several weather conditions such as icing, heavy rain, etc., atmospheric gust or turbulence is the most common one encountered by aircraft [1]. Consequently, the effects of atmospheric gusts or turbulence in aviation are being investigated for more than a century [2],[3]. It is no surprise that such effort is being spent to accurately model or generate gusty flow conditions in a controlled environment, as a gust of wind is the reason for the severe structural damage and end of test flights of the Wright Flyer, i.e., the world's first successful powered airplane [4]. Thus, this thesis is concerned with the design, computational and experimental investigations of a wind tunnel gust generator that is built with the purpose of producing gusty flows of desired profile, magnitude and fully known temporal and spatial behavior. The outcomes of this study will serve as a starting point for the design of a gust generator which will be placed in the Large Scale Wind Tunnel of METU Center for Wind Energy Research (RÜZGEM).

1.1 Overview of Gust Problem

An air vehicle subjected to gust loading is a common phenomenon occurring as a result of turbulent flows in the atmospheric boundary layer [5]. Depending on the magnitude, gusts may cause flow separation and other complexities when they interact with the lifting surfaces of air vehicles [6]. Gusts influencing air vehicles can be

categorized based on the gust velocity direction relative to the vehicle. Vortex gusts, for instance, are characterized by coherent vortex structures that result in a specific velocity distribution [7]. Streamwise gusts arise as a result of the changes in the freestream velocity [8] while for transverse gusts, gust velocity acts normal to the vehicle's cruise direction. Each of these discrete gust phenomena interacts with the lifting surface in a different way to generate unsteady disturbances in the effective angle of attack and camber distribution. Transverse gusts are particularly responsible for unsteady and separated flows [5] and result in the generation of large loads. This is also crucial for vehicle control and needs to be carefully investigated.

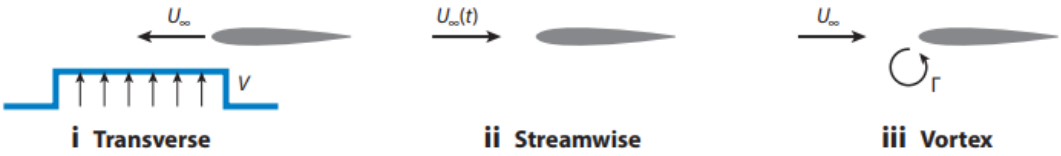


Figure 1.1: Three categories of discrete gust encounters [6].

In terms of modeling, an airfoil subjected to gust loading undergoes a motion that consists of an arbitrary rotation about any arbitrary point and arbitrary heaving [9]. Thus, unlike an airfoil undergoing an impulsive motion, the behavior of an airfoil under gust cannot be modeled with the downwash at the three-quarter chord point.

The downwash varies with time and position of the airfoil as the gust encounter continues. Hence, downwash induced due to gust encounter can be modeled as:

$$w_a(x,t) = w_a(x - U_\infty t) \tag{1.1}$$

The downwash and gust velocity have opposite signs:

$$w_a(x - Ut) = -w_g(x - U_\infty t) \tag{1.2}$$

For a gust with a constant gust speed of w_0, the time-dependent gust function can be modeled as:

$$w_g(x - Ut) = \begin{cases} 0 & U_\infty t < x + b \\ w_0 & U_\infty t \geq x + b \end{cases} \tag{1.3}$$

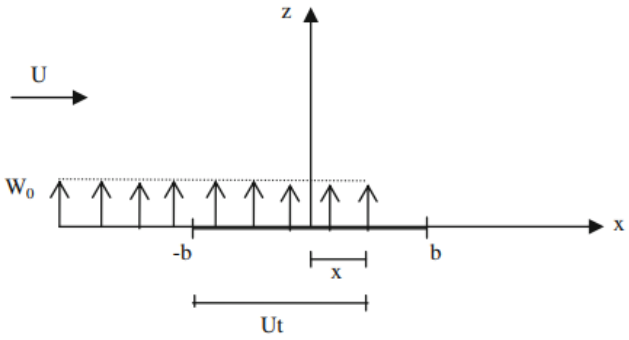


Figure 1.2: Downwash induced by the gust [9].

An important parameter in the characterization of the gust flow is the reduced frequency. Physically, it is the number of oscillations in radians per half chord travel of the airfoil [9]. Thus, it is regarded as a dimensionless measure of unsteadiness and is defined as:

$$k = \frac{\omega b}{U_\infty} \tag{1.4}$$

where ω is the circular frequency, b is the half chord length and U_∞ is the freestream velocity.

$$\omega = 2\pi f \tag{1.5}$$

where f is the frequency of the motion.

To predict the forces induced due to a sharp-edged transverse gust on a wing, Küssner's model is a simple yet powerful linear model [10]. The lift response predicted by Küssner's model is:

$$C_l\left(\frac{s}{c}\right) = 2\pi GR\, K\left(\frac{s}{c}\right) \tag{1.6}$$

where s/c is the distance in chords from the wing leading edge to the beginning of gust and K is the Küssner response function and GR is the gust ratio.

$$GR = \frac{v}{U_\infty} \tag{1.7}$$

Arbitrary gust shapes, on the other hand, can be predicted utilizing the Duhamel superposition [11] while the Küssner response function is derived for a step change. For an arbitrary gust shape, summation of the step response of all the incremental elements that have influenced the wing at previous times, τ should be calculated.

$$C_l\left(\frac{s}{c}\right) = 2\pi \int_0^{s/c} \frac{\mathrm{d}K(\tau)}{\mathrm{d}\tau} GR\left(\frac{s}{c} - \tau\right) \mathrm{d}\tau \tag{1.8}$$

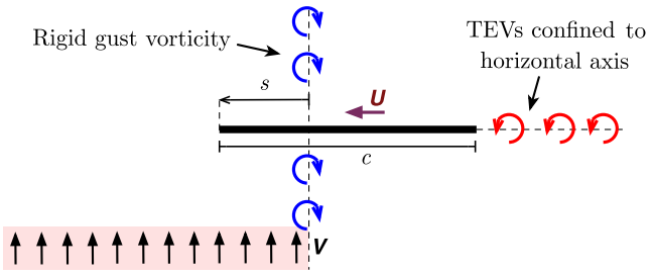


Figure 1.3: Küssner's model [5].

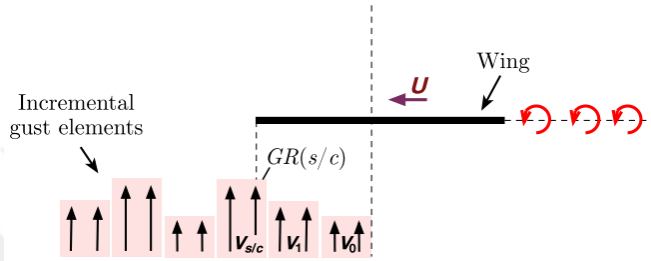


Figure 1.4: Duhamel superposition applied to an arbitrary gust shape [5].

Although Küssner's model is a simple but powerful linear model and has been validated for a wide variety of gust ranges, the fact that it is derived under many assumptions makes its accuracy questionable for high-amplitude gusts especially. Assumptions of the model, as illustrated in Figure 1.3 are as follows:

1. Flow is inviscid and incompressible.
2. No vorticity is shed from the leading edge.
3. Vortices shed from the trailing edge are on the horizontal plane aligned with the wing.
4. Disturbances are small, hence, small angle approximations are valid.
5. Gust shear layer is rigid and no deflection of the shear layer occurs during the encounter of the wing with gust.

Thus, Küssner's model may fail to predict the forces on a wing with full accuracy when it is submerged in gust, especially when leading edge separation or trailing edge

wake distortion are present. This is one of the main reasons why a gust generator that is capable of creating gusts in a fully controlled manner is significantly necessary.

1.2 Certification Requirements

The operational envelope of air vehicles is typically limited by maximum structural loads and the capability to control the vehicle under any disturbance encountered during flight. Identifying the maximum gust that a vehicle might encounter is thus of utmost importance [6]. Therefore, in the design and certification processes for the aircraft, gust encounters are critical and require significant attention.

For fixed-wing aircraft, civilian certification and military qualification require the evaluation of maximum loads on lifting and control surfaces and the ability to recover from discrete gusts. For large airplanes, for example, certification specifications of European Aviation Safety Agency (EASA) defines the following gust shape in CS-25 [12]:

$$U = \frac{U_{ds}}{2}\left(1 - \cos\frac{\pi s}{H}\right) \tag{1.9}$$

where U_{ds} is the design gust velocity, s is the distance penetrated in gust and H is the gust gradient which is the distance parallel to the airplane's flight path for the gust to reach its peak velocity. The airplane is assumed to encounter symmetrical vertical and lateral gusts in level flight. The limit loads as a result of the gust of specified shape should be proven to be lower than critical loads.

For a very light aircraft, which is also assumed to be subjected to symmetrical vertical gusts in level flight, for which the shape of the gust is defined by [13]:

$$U = \frac{U_{de}}{2}\left(1 - \cos\frac{2\pi S}{25\bar{C}}\right) \tag{1.10}$$

where S is the distance penetrated into gust, $\bar{C}$ is the mean geometric chord of the wing and U_{de} is the derived gust velocity.

Design gust velocities are varied based on flight altitude while the maximum gust velocity is assumed to occur once in 70000 flight hours. Gust loads should be calculated for a range of gust speeds and altitudes for certification.

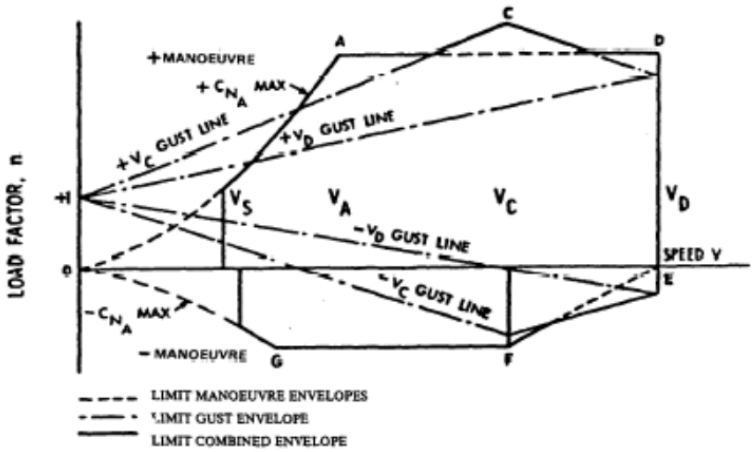


Figure 1.5: Flight envelope limited by gust loading [13].

Military specifications also require a load analysis under a $1 - \cos$ shaped gust loading, both in transverse and longitudinal directions [14]. For flight controls, U.S. military standard MIL-STD-1797A (USDOD 2004) demands a rigid body analysis of the response of the vehicle to both discrete and continuous gusts. Exact distributions instead of discrete gusts are analyzed to investigate the potential resonance of the vehicle when the range of disturbance frequencies is close to a structural mode frequency.

For rotorcraft, on the other hand, both normal and transport civilian vehicles should be proven to have substantiated loads for all airspeeds from hover to 1.1 times the never-exceed speed for vertical gusts of 30 ft/s [15]. This constant gust velocity results in a gust ratio range of 0.25 to 5. The gust profile is assumed to be a sharp-edged gust.

In addition to certification requirements for gust encounters, low to medium gust induced aerodynamic loads may lead to passenger discomfort, deterioration of payload, etc. [16]. The severity of gust is quantified in terms of Δn, which is the increase in load factor expressed in terms of gravity and it should not exceed 2.5 g at the pilot's seat for safety [17].

Apart from conventional large aircraft, MAVs are subjected to gust loading more frequently as they operate at lower altitudes and in city environments. Therefore, a thorough understanding of wing-gust encounters is critical for MAV design and gust mitigation techniques [23]. Also, it is shown in Figure 1.6 that a decrease in the size

of the vehicle results in a greater gust ratio for the same atmospheric condition. This demonstrates that gust response investigation is even more significant for vehicles of smaller scale.

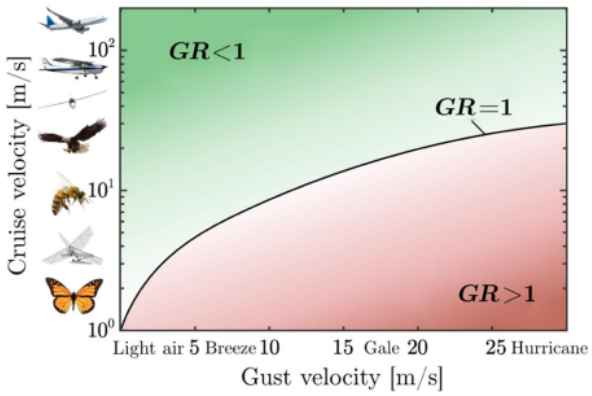


Figure 1.6: Gust ratios experienced by vehicles and animals for different atmospheric conditions [24].

On the other hand, the performance of wind turbines is inevitably affected by ambient atmospheric occurrences such as gusts [18]. Atmospheric gusts may reduce the effectiveness of wind turbines extremely [19], therefore it is crucial to investigate the turbine performance under gust loading. It becomes even more critical to explore the influence of atmospheric gusts in wind farms where turbine-wake flow interactions are of significance regarding the annual energy production of the farm [20].

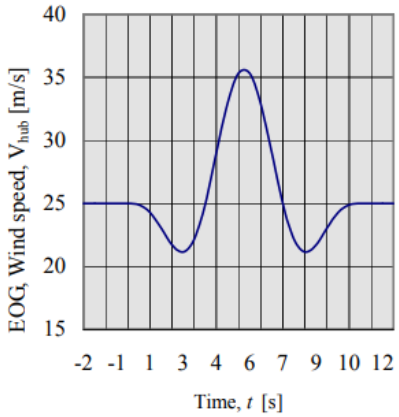


Figure 1.7: Extreme operating gust (EOG). $N = 1$, where N is the period in years, rotor diameter is 42 m, hub height is 30 m and hub velocity is 25 m/s [22].

Turbulence impinging on the turbine, especially in the root section, and the resulting

velocity fluctuations are the main reasons of dynamic effects for a wind turbine. These effects act as a change in the direction of the incoming flow, leading to the formation of dynamic loads on the blades. These loads eventually result in enhanced structural fatigue in the entire system and a shortening of the service life [19]. The possibility for the amplitude of the variation in the angle of incidence due to transverse gusts to exceed several degrees is significantly high, depending on the turbine operating conditions and span position [21]. Therefore, gust response is an important criterion in the certification and design of wind turbines.

For the certification, wind conditions are specified such that wind loads acting on the wind turbine can be calculated. A wind turbine should be designed to withstand the wind conditions safely and hence, extreme wind conditions such as gusts should be utilized to determine the wind loads acting on the wind turbine [22].

The maximum gust ratio, GR, in the example shown in Figure 1.7 equals approximately 0.65.

Consequently, for the certification of fixed-wing aircraft, rotorcraft, MAVs, and wind turbines, the gust response is critical and needs to be investigated.

1.3 Gust Generator Design

Artificial gust generating systems are essential for the studies in which the unsteady response of lift-producing surfaces is investigated. The fact that they can be implemented to a wide variety of wind tunnels has made them popular among the researchers who are interested in the gust response of wind turbines, helicopters, micro-air vehicles and fixed-wing aircraft [25], and have caused institutions to design their own gust generating systems that can be employed in conventional wind tunnels.

Gust generators are devices which are positioned upstream of wind tunnel test sections and capable of generating gusts of desired profiles and magnitudes. They are generally composed of oscillating vanes which can be controlled to perform specific motion kinematics such that a desired gust profile is obtained at the test section. As the vanes oscillate, the flow direction in the test section alters as a result of the syn-

thesis of two flows, i.e., the main flow of the wind tunnel and the flow induced by the oscillating vanes in the transversal direction.

Different gust profiles can be obtained by varying the maximum deflection angle of the vanes and the frequency at which the vanes oscillate [26]. There are many studies in the literature discussing the design and development of gust generation systems. A combined experimental and numerical study investigates the design parameters that affect the gust generator performance and accordingly, a gust generation system has been built for the large low-speed wind tunnel located at the University of Bristol [27]. Their work stresses the effectiveness of two design parameters, i.e., chord length of the vanes and distance between the vanes, on the gust amplitudes. Increasing the chord length and decreasing the distance between the vanes result in an increase in the gust amplitude, yet a decrease in the vane spacing results in a decrease in the useful area of the test section at which the experiments can be conducted. The study also reveals that the gust profiles obtained in the test section of the wind tunnel have a square shape rather than a sinusoidal shape for frequencies higher than 8 Hz.

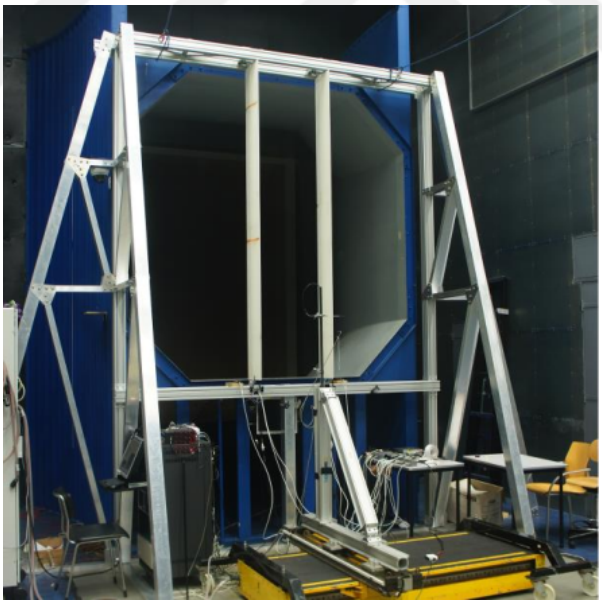


Figure 1.8: Gust generator designed for the Open Jet Facility in Deft University of Technology [28].

Another gust generator system has been designed for the Delft University of Technology Open Jet Facility which has a 2.85 m$\times$2.85 m test section and a maximum

flow velocity of 35 m/s [28]. The preliminary work done for the design of the gust generator revealed that in addition to the design parameters mentioned previously, the reduced frequency, which is the ratio of chord length to the wavelength of the vortex shed from the flapping wing, and the maximum deflection angle are of importance in the design of gust generators.

Dynamic response of an elastic wing model to a gust induced by a single NACA0010 shape vane gust generator is investigated in a transonic wind tunnel at DLR [29]. Comparison of the experimental and computational results demonstrates that using Computational Fluid Dynamics (CFD), to be able to obtain the gust velocity measured via Particle Image Velocimetry (PIV), aerodynamic mesh in the wake region of the gust generator should have a high quality. Furthermore, generation of a uniform gust is critical for the repeatability of the experiment and ease of computation of the gust response of the wing. However, use of a single gust vane results in the creation of a shear flow region in the wake behind the gust generator, and this shear flow region due to the airfoil boundary layer reduces the uniformity of gust in space. Consequently, addition of a second gust vane is suggested to increase gust uniformity [28].



Figure 1.9: Disturbance generator mounted in the wind tunnel contraction in Virginia Tech Stability Wind Tunnel [30].

A computerized gust generator has been developed and tested for the Virginia Tech Stability Wind Tunnel [30]. The system consists of 10 gust vanes placed from the

bottom to the top of the contraction of the wind tunnel. The system is shown to be capable of generating both continuous and impulsive disturbances, utilizing stepper motors to drive the vanes independently. An increase in the motion amplitude results in an acceleration in the gust weakening and thus, a more rounded disturbance shape is encountered. This is explained by enhanced wall dampening at larger amplitudes.

Another example of a gust generator has been designed for an open jet, closed return wind tunnel [31]. The system consists of six mechanically interconnected oscillating vanes mounted in a frame and fixed to the wind tunnel nozzle. Vane profile is NACA0015 and the upper limit for pitching is 12°, to avoid stalling. Pitching frequency of the vanes varies between 0.5 Hz and 2.0 Hz. Experimental results show that a good approximation to a sine wave can be obtained directly behind the vanes. Further downstream of the vanes, peaks and troughs of the sinusoidal variations in the transverse velocity component become flattened due to the influence of the vane wake.

A small oscillating fence in a wind tunnel is proposed as a gust vane to overcome the limitation of high mechanical frequency [32] for a novel gust generator. The setup consists of two fences as gust vanes, which can be actuated to produce angles β_1 and β_2 between 0° and 90°. While still able to deflect the freestream, the small oscillating fence could partially overcome the limitations of large inertia and power requirement.

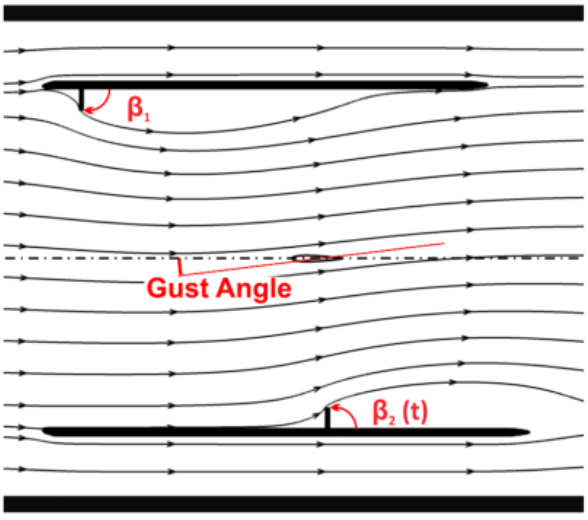


Figure 1.10: Conceptual sketch of the gust generator built for the large wind tunnel at the University of Bath [32].

The gust generator apparatus designed for the S3Ch transonic wind tunnel at ONERA consists of a tandem of oscillating airfoils positioned horizontally right before the entrance of the test section [16]. The setup is composed of two identical NACA0012 airfoils positioned at the nozzle part of the wind tunnel. They are made of an optimized architecture combining composite and metallic parts such that the inertia is reduced and high frequencies of actuation under heavy aerodynamic loading can be obtained. The vanes are driven by four servohydraulic jacks and pitch about their quarter chord point at frequencies up to 80 Hz in air streams up to Mach 0.73 for atmospheric stagnation conditions.

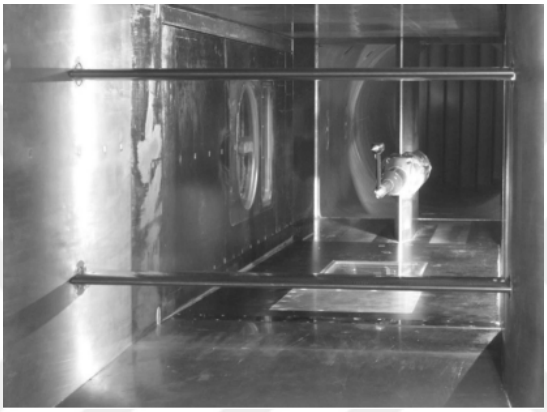


Figure 1.11: Gust generator located at the S3Ch transonic wind tunnel at ONERA [16].

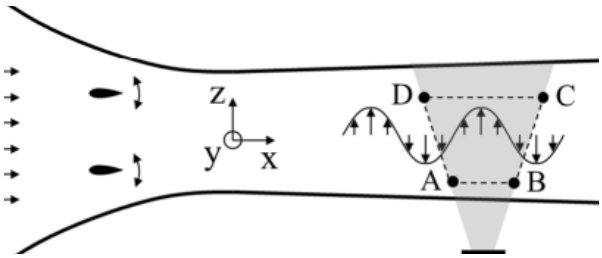


Figure 1.12: Schematic of the apparatus and the experimental setup [16].

To generate a fluctuating transverse velocity component in the test section, i.e. a transverse gust, a suction duct on top of the test section is added to the Andrew Fejer Unsteady Wind Tunnel [33]. Individually controlled louvers placed at the inlet of the suction duct are utilized to distribute the suction produced on top. This results in a variation of the velocity components both temporally and spatially. Thus, transverse,

steady and traveling-wave flows can be generated in the test section. The fact that fluctuation in the transverse velocity component is in one direction only results in the generation of a gust flow having a $1 - \cos$ form. The system consists of 4 louvers positioned at the downstream end of the test section, whose main function is to control the freestream velocity. The ceiling of the test section contains 10 louvers, each controlled individually by servo motors. Rotation of the louvers results in a variation in the blockage of the channel, ranging from fully open to fully blocked. The mechanism of gust generation for this setup is attributed to the flow diverging from the main flow due to the suction that is generated.

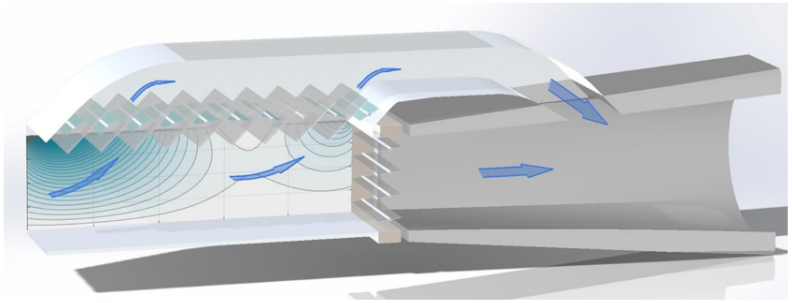


Figure 1.13: Schematic of the test section [33].

To generate well-defined two-dimensional inflow conditions for wind tunnel experiments, a 2D active grid, i.e., a gust generator is designed in the University of Oldenburg [34]. The focus is on the generation of sinusoidal transverse and streamwise gusts with high amplitudes and frequencies. Three different configurations regarding the vane number, chord, and spacing have been tested in a reduced frequency range from 0.07 to 0.85.

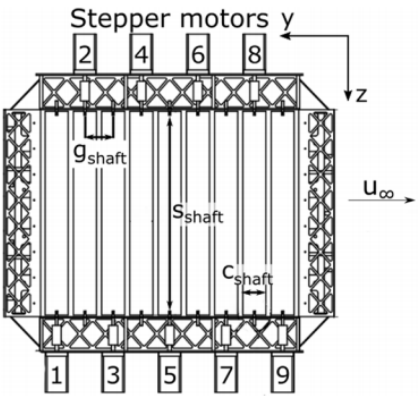


Figure 1.14: Technical drawing of the 2D active grid, i.e., gust generator [34].

The study reveals that a significant factor regarding transverse gust amplitude is the arrangement of the vanes. To obtain larger amplitudes, the vanes should be distributed over the entire width of the test section. Also, the ratio of vane spacing to chord length should be approximately 1.1-1.5. With an increase in the vane number, blockage variation increases. Thus, streamwise gust amplitude increases. Moreover, an improvement in flow quality can be obtained by using aerodynamically shaped vanes instead of flat plates. Finally, streamwise gust can be significantly reduced and an isolated transverse gust can be generated if the vanes are not installed on the centerline of the test section. However, this comes with a penalty in the maximum achievable amplitude.

Table 1.1: Gust vane parameters of vane-type gust generator setups

Study	Number	Profile	Chord/Span	Spacing
Buell (1969) [26]	6	NACA0015	0.159	1.04
Grissom (2004) [30]	10	NACA0018	0.192	1.41
Neumann (2013) [29]	1	NACA0010	0.300	N/A
Brion (2015) [16]	2	NACA0012	0.248	1.8
Saddington (2015) [31]	6	NACA0015	0.100	2.22
Lancelot (2015) [28]	2	NACA0014	0.104	1.33
Wood (2017) [27]	2	NACA0012	0.150	1.66
French (2021) [36]	2	NACA0018	0.200	1.53

Table 1.2: Actuation parameters of vane-type gust generator setups

Study	Amplitude [°]	Frequency [Hz]	U_∞ [m/s]
Buell (1969) [26]	16	5-15	15-75
Grissom (2004) [30]	45	10-50	15
Neumann (2013) [29]	2.1	37.89	249.73
Brion (2015) [16]	5	20-80	102-248
Saddington (2015) [31]	12	0.5-2	7-14
Lancelot (2015) [28]	10	0.6-4.2	15-25
Wood (2017) [27]	20	2-14	8-24
French (2021) [36]	10	0.5-2	18

Table 1.3: Actuation parameters of vane-type gust generator setups

Study	k_{max}	Motion
Buell (1969) [26]	0.15	$\sin$
Grissom (2004) [30]	1.44	Discrete $\sin$
Neumann (2013) [29]	0.14	$\sin$
Brion (2015) [16]	0.49	$\sin$
Saddington (2015) [31]	0.10	$\sin$
Lancelot (2015) [28]	0.188	$\sin$
Wood (2017) [27]	1.65	$1 - \cos$
French (2021) [36]	0.05	$\sin$

1.4 Computational Investigation of Gust Generators

To evaluate different design alternatives, several researchers have run CFD analyses on gust generators. In the combined experimental and numerical study for the gust generator designed for the Large Low Speed Wind Tunnel for the University of Bristol, an initial 2D CFD analysis is run to investigate the behavior of tip vortices [27].

A 3D CFD model is also designed for the characterization studies of the gust generator. Wind tunnel background contains approximately 8 million mesh elements while the mesh structure is of prism layers growing from the boundaries of no-slip condition. A second order solver is utilized with a time step of 0.001 s. An incompressible Reynolds-Averaged Navier Stokes paradigm is selected to run the simulations and the realizable $k - \varepsilon$ model is used for turbulence closure.

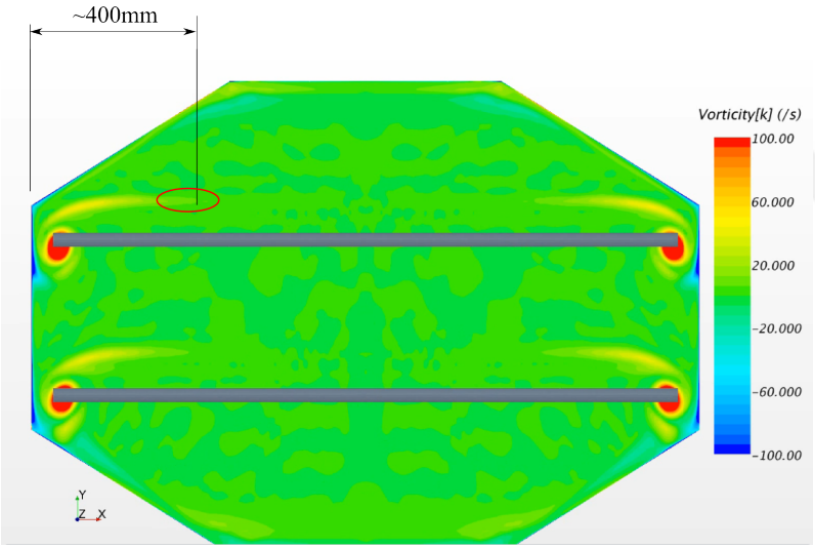


Figure 1.15: Extent of the gust vane tip wake when the gust vanes are not full span. There is a 70 mm gap at both walls resulting in a wake flow that extends up to 400 mm from the wall [27].

A structured 2D grid is created for the simulations of the gust generator designed for the Open Jet Facility at Delft University [28]. The final grid obtained after a grid convergence study consists of 10^5 deformable rectangular elements. A pressure-based Spalart Allmaras turbulence model is used. Time step is set to be 0.002 seconds. The vane motion is simulated by moving the boundaries of the airfoils around the quarter

chord location of the airfoils.

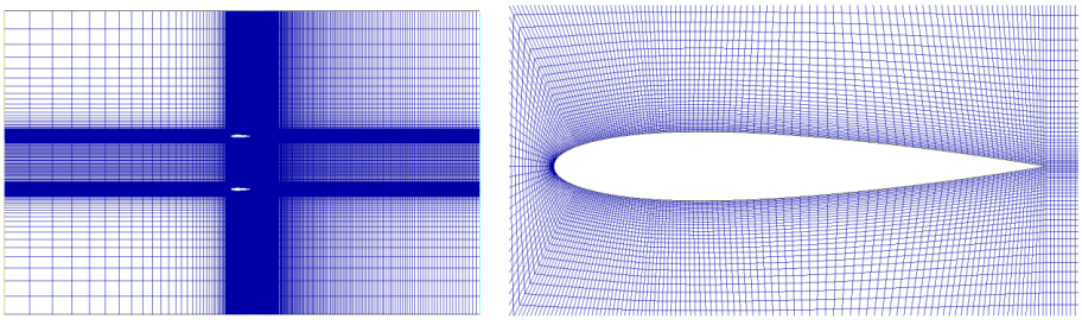


Figure 1.16: Structured 2D mesh grid [28].

The numeric evaluation of different designs has been conducted using STAR CCM+ v12.04 (Siemens PLM software) and ANSYS CFX CFD software packages for the gust generator designed for The University of Maine Crosby Hall Wind Tunnel [36]. As the gust vanes span the whole test section, flow is approximated as 2D. Curvature meshing and controlling the boundary layer resolution on the airfoils have been adapted to increase the mesh density around the gust vanes. The domain mesh contains tetrahedral elements with a minimum allowable size of 10^{-3} mm and a maximum size of 5 mm. A mesh convergence study has also been conducted over five mesh grids. The tunnel walls and the airfoil surfaces are defined as no-slip boundaries while the outlet flow condition is set to 0 Pa gauge pressure.

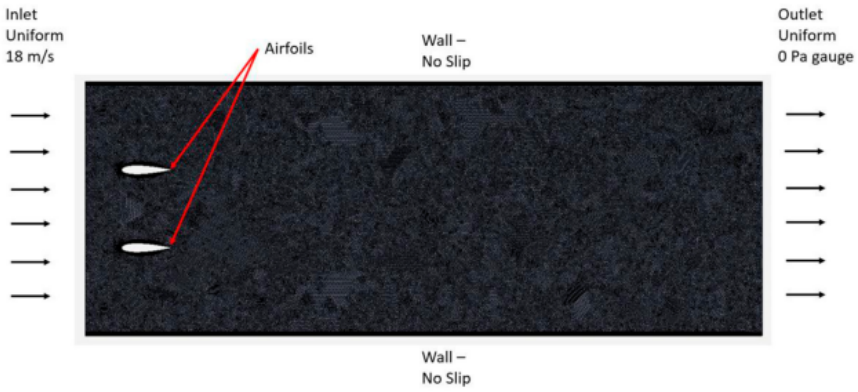


Figure 1.17: Boundary conditions and mesh grid [36].

Steady-state simulations are run for the cases when the gust vanes are at 0°, $\pm 5°$ and $\pm 10°$ of angle of attack. As the motion frequency is low, (0.5-1 Hz), a quasi-steady condition is present and steady-state solutions can be sought. A second-order upwind

scheme has been utilized with $k - \omega$ SST turbulence model.

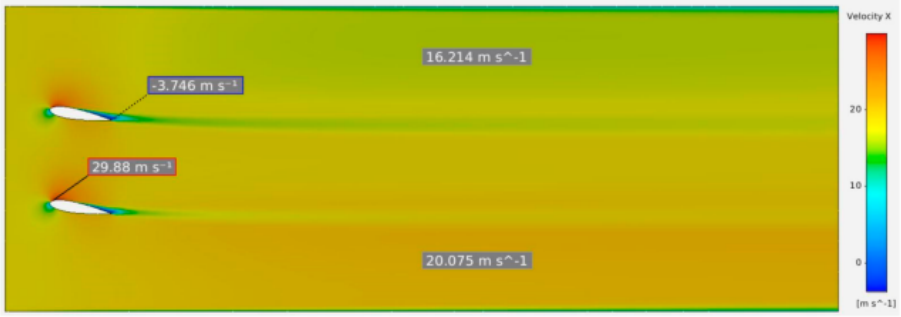


Figure 1.18: Results of the magnitude of flow velocity for the case when the airfoils are at 10° of angle of attack [36].

1.5 An Application Regarding Wind Turbines: Porous Disk Approach

It is a common practice to use porous disks to simulate the far wakes of wind turbines in wind tunnels [37], as wakes of a rotating model and a porous disk developing in the modeled atmospheric boundary layer are indistinguishable after three rotor diameters downstream of the rotor disks [38]. Under low turbulence inflow conditions, comparison of the near wake (from $x/D = 0.1$ to $x/D = 2.2$) characteristics of a porous disk with a wind turbine having the same diameter and thrust coefficient by means of stereoscopic PIV reveals that porous discs can be employed to emulate the wake velocity profiles of a wind turbine also in the near wake region [39]. On the other hand, a significant difference in the wake growth characteristics of porous disks and wind turbines at fairly low ambient turbulence intensities have been reported [40].

In order to assess the similarities in the mean kinetic energy transport within a wind farm, wind tunnel measurements on an array of model wind turbines and porous disks are also performed [41]. It is revealed that the mean kinetic energy transport can be emulated by the porous disk, especially in the far wake. Comparison of near wake characteristics under different inflow conditions shows that up to 4 diameters downstream, turbine and porous disk have similar wake characteristics [42]. Thus, it can be deduced that porous disks can be used to emulate wind turbine wake flows in wind tunnel tests.

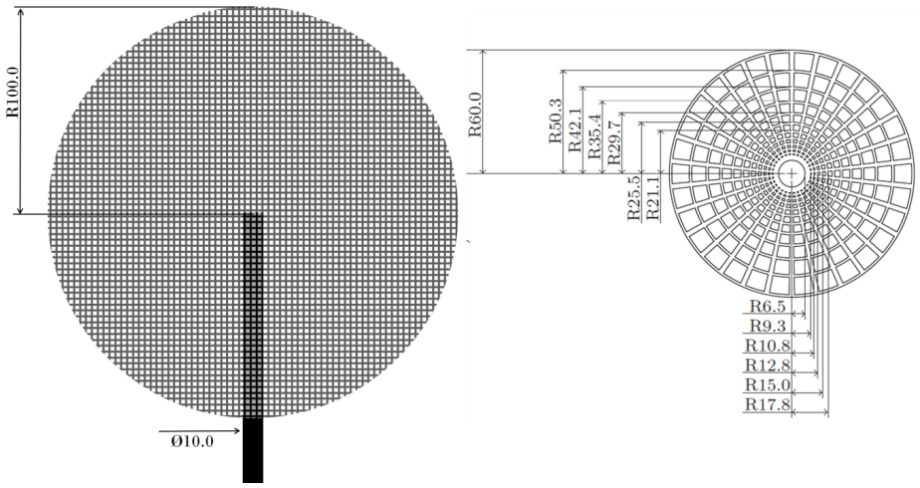


Figure 1.19: Two porous disk models based on the simplest wind turbine model: the actuator disk concept [43].

Two sample porous disks are shown in Figure 1.19, where the disk on the left is made of metallic mesh and has a uniform porosity of 57% while the disk on the right is made of plywood with a radially non-uniform porosity [43].

Although porous disks have been tested under different inflow conditions in terms of inflow wind shear and turbulence intensity levels, their performance in gusty inflow conditions, i.e., their fidelity in mimicking a wind turbine under gust loading, in a wind tunnel has not been assessed yet in the literature.

1.6 Objectives and Scope of the Thesis

Several researchers have proposed and implemented methods to produce deterministic gust flows in wind tunnels. In practice, gusts are a combination of many flow structures such as shear layers, coherent vortices, updrafts, downdrafts, and turbulence [6]. In a laboratory, producing these complex flow phenomena is critical to make the problem more tractable and mimic the flight environment that air vehicles encounter. In this respect, a two-vane gust generator is designed, manufactured, and integrated into a small-size open-loop wind tunnel to generate deterministic gust disturbances in the closed test section, both in streamwise and transverse directions. Design and characterization studies of the gust generator have been performed based

on the studies described in the previous section and are explained in further detail in this thesis. This gust generator will also constitute a basis for a large-scale gust generator to be implemented in the Large Scale Wind Tunnel in the METU Center for Wind Energy Research (RÜZGEM).

In the design, CFD simulations have been utilized to evaluate different design alternatives and determine the operating range of the gust generator. For the characterization, two-dimensional and two-component (2D2C) phase-locked PIV measurements have been performed by discretizing a period of motion into a minimum of 13 phases.

Several design parameters have been varied and the resulting gust behavior both in a spatial and temporal sense has been investigated. The effects of motion frequency, freestream velocity, spacing between the vanes, and motion amplitude on the resulting gust flow have been analyzed both by experimental and computational means. Full characterization of the gust generator has been completed. Then, as an application, a porous disk and a model wind turbine having the same thrust coefficient are placed downstream of the gust generator. Wake flows of the two models under a sinusoidal transverse gust loading have been compared.

The first chapter provides an overview of the gust problem, as well as a literature review of the gust generators designed by several other institutions. The second chapter details the design process, as well as the computational and experimental methods adopted in the study. In the third chapter, experimental and computational results are presented along with the findings of the study. Finally, a discussion regarding the presented results and suggestions for future work are demonstrated in the fourth chapter.

CHAPTER 2

METHODOLOGY

2.1 Wind Tunnel

Measurements are conducted in the C1 wind tunnel located at the METU Center for Wind Energy Research (RÜZGEM). It is an open-circuit suction-type wind tunnel with a maximum freestream velocity of 25 m/s and an inlet turbulence intensity of 0.5%.

Incoming air flow passes through a honeycomb, a screen, and a 1 m long settling chamber before the contraction section with a 9:1 contraction ratio. The test section has a square cross-section of 34×34 cm^2 and is 100 cm long. Its walls are made of plexiglass with a thickness of 1 cm. The flow is diffused through a 2 m long diffuser afterward. The divergence angle is 2.43° to avoid an excessive adverse pressure gradient. The flow in the wind tunnel is driven by a fan and a 4 kW electric motor. Finally, a 1.7 m long adapter converts the square cross-section into a circular one, to hold the fan. A Pitot-static tube is placed at the end of the contraction section to measure the flow velocity at the inlet of the test section.

2.2 Gust Generator

In this section, design, computational, and experimental investigation methods of the gust generator are presented. The gust generator consists of two oscillating-vanes controlled by servo motors. It has been built and integrated into the C1 wind tunnel at RÜZGEM with the purpose of generating gusts of desired amplitude and profile in the test section.

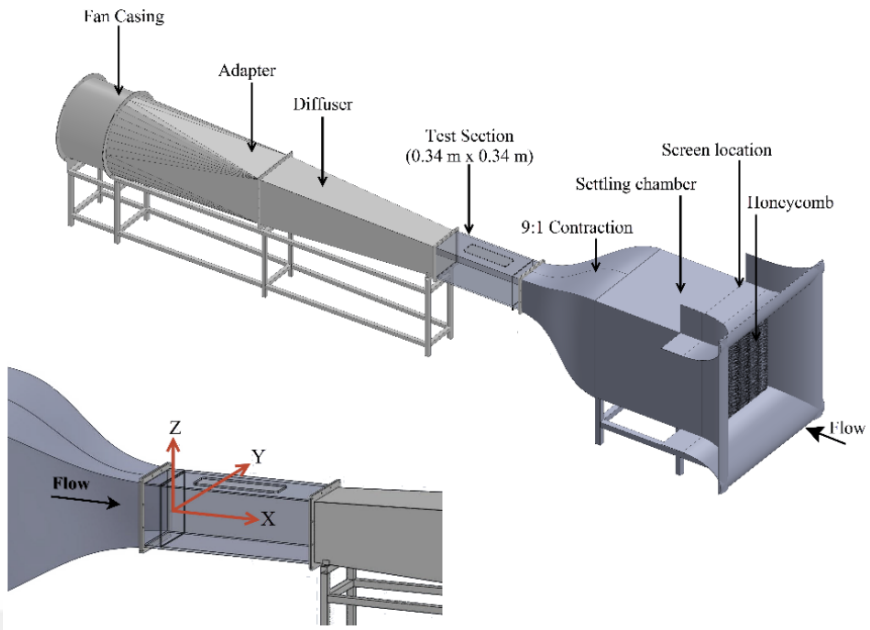


Figure 2.1: Wind tunnel parts and definition of the coordinate system.

2.2.1 Conceptual Design of the Gust Generator

The main goal in the design and manufacturing of a wind tunnel gust generator is to produce uniform gusts with a desired waveform and amplitude in a deterministic manner. In the present mechanism, the gust generator consists of the gust vanes, motors to run and control the vanes, and a frame to mount the gust vanes and place the motors for the integration into the wind tunnel. Properties of the gust vanes are determined based on the limitations of the size of the test section and preliminary numerical simulations.

2.2.1.1 Design of the Gust Vanes

In this assembly, gust is generated as a result of the down and upwashes generated due to the motion of the vanes. Transportation of the down and upwashes generated due to the oscillation of the airfoils by the wake vorticity results in the formation of gust [16]. In this case, the wakes limit the region of uniform and low turbulent flow in the test section while the clean part of the flow is between the airfoils. If a single gust vane is utilized, the location where the models are typically put suffers from wake

interferences, which may result in an additional turbulent forcing upon the model. On the other hand, usage of three or more vanes is limited by the test section size. Consequently, the most feasible design for the available wind tunnel is with two gust vanes.

It is observed that NACA0014 [28] and NACA0015 [27],[31] profiles have been utilized in the wind tunnel gust generators of several institutions. Consequently, vane profile is selected to be NACA0015 to allow for a sufficiently large rod diameter to be integrated to the vanes such that the vanes are connected to the motors via a shaft. Moreover, maximum amplitude of pitching, i.e. the angle of attack of the gust vanes varies between 12° and 16° for NACA0015 airfoils in the setups of other institutions. To ensure that the vanes do not stall, the pitch angle is limited to 12° for the vanes with NACA0015 profile in the gust generator setup in the University of Cranfield [31]. Yet, it is noted that for NACA0015 profiled vanes, pitch angles up to 16° can be utilized without encountering a severe flow separation [26]. It is also demonstrated that for NACA0015, stalling takes place between $10^\circ < \alpha \leq 15^\circ$ [47]. For this reason, a maximum amplitude range of 8°-16° is chosen to observe the effect of motion amplitude on the resulting gust flow.

The vanes have a span of 33 cm such that any contact with the test section walls is prevented. This leaves a 0.5 cm distance between the vane tips and test section walls. This gap will result in tip vortices being present and affecting the flow field. However, simulation results shown for a gust vane with a 300 mm chord indicate that a 70 mm ($0.23c$) gap results in tip vortices being present for 400 mm ($1.33c$) distance in the spanwise direction [27]. For the current setup, distance between the vane tips and test section walls is $0.0625c$, which is significantly smaller than $0.23c$. Thus, it may be concluded that the tip vortices will not have an effect on the midspan locations of the gust vanes, which is the plane of interest for PIV measurements.

The ratio of chord length over the span length of the gust vanes of vane-type gust generator systems illustrated in Table 1.1 results in a chord length range of 5-10 cm. It is known that there is a linear relationship between the chord length of the vanes and the amplitude of the resultant gust [28].

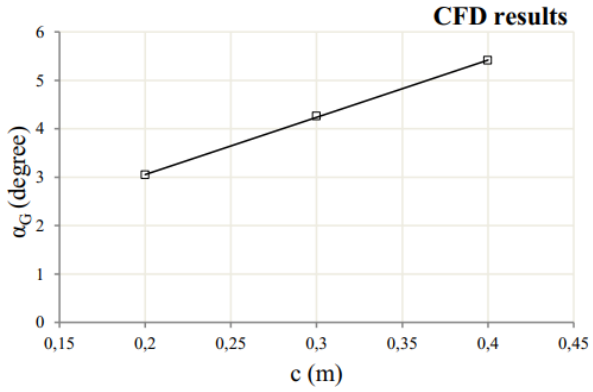


Figure 2.2: The maximum gust angle measured for different chord lengths [28].

The results shown in Figure 2.2 are at 1.5 m behind the leading edge of the gust vanes, in the center axis of the fluid domain, with a pitching amplitude of 10°. As illustrated in Figure 2.2, with increasing chord length, the gust ratio (GR) increases linearly. However, the limiting factor for the increase of the chord length is the blockage ratio. The system should be designed such that the power of the fan is sufficient to generate the desired freestream velocities in the test section, which is not possible under a high blockage ($> 10\%$). Also, the blockage ratio should be kept at a limit in order to be able to obtain a uniform velocity profile in the test section. For a chord length of 10 cm, considering that there are two gust vanes, a blockage ratio of 15.74% exists when the vanes are at an angle of attack of 16°. Thus, chord length is determined to be 8 cm, which results in a blockage ratio of 12.59%, which is a more convenient value to run wind tunnel tests.

Distance between the vanes (d), on the other hand, varies between 1.0 and 2.5 chords, in the gust generators of other institutions, as illustrated in Table 1.1. For this reason, vane spacing range for the characterization tests is chosen to be between 1.0-2.5c.

2.2.1.2 Motor Sizing

Motor sizing is done based on the required torque of the system. This may be investigated in two parts, one of which is the aerodynamic torque and the other is the inertial torque. Inertial torque is described by

$$T = \sum I\ddot{\theta} \tag{2.1}$$

Vanes undergo a sinusoidal motion, hence, angular position is governed by

$$\theta = \bar{\theta}\sin(\omega t) \tag{2.2}$$

where

$$\omega = 2\pi f \tag{2.3}$$

Moment of inertia is calculated based on the CAD drawing of the system. Furthermore, the aerodynamic torque is calculated utilizing the unsteady potential flow theory and turned out to be not dominant in the total torque of the system and attains a maximum value of 0.195 Nm. Inertial torque, on the other hand, equals to 0.56 Nm [48]. As a result, two servo motors with 400 W power and 1.27 Nm nominal torque are selected to drive the two vanes.

2.2.1.3 Design of the Frame

Vanes are mounted at the inlet of the test section, in a metal frame with a length of 15 cm. Motors are connected to the vanes from the top via a shaft centered at the quarter chord point of the vanes. Shafts have a length of 41 cm and extend through the full span of the vanes and the test section. The vanes with NACA0015 profiles are 3D printed using PLA+ filaments and installed on the gust generator system. The frame is built such that the distance between the two vanes is manually adjustable.

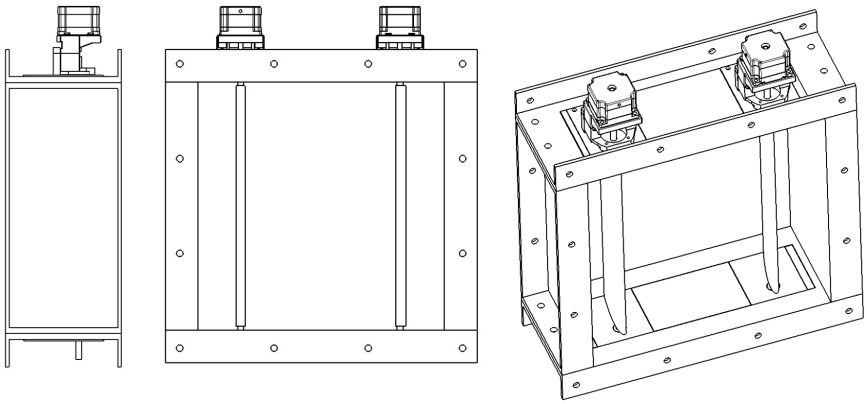


Figure 2.3: CAD drawing of the gust generator system. Side, front and isometric views respectively.

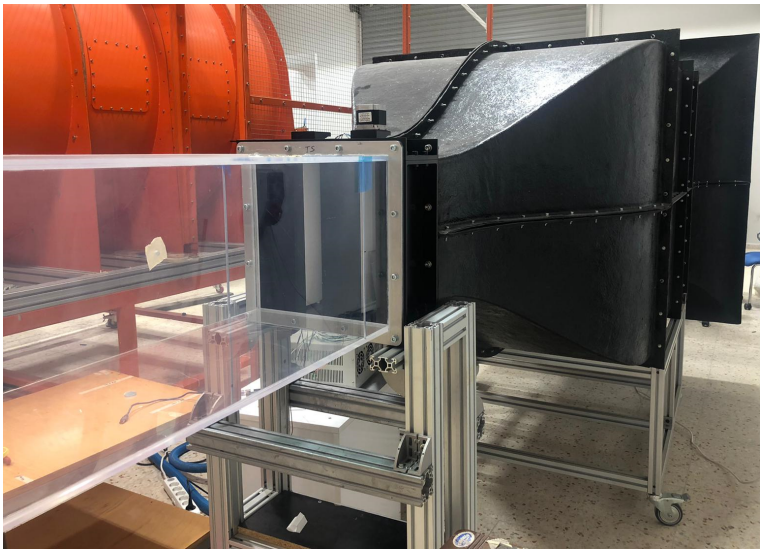


Figure 2.4: Gust generator integrated into the entrance of the test section of the C1 wind tunnel at RÜZGEM.

2.2.2 CFD Analyses of the Gust Generator

For the characterization of the gust generator, several CFD simulations have been run in the commercial CFD solver ANSYS Fluent. The setup is configured such that two sinusoidally pitching NACA0015 airfoils with a chord length of 8 cm in a domain with a length of 1.5 meters are analyzed.

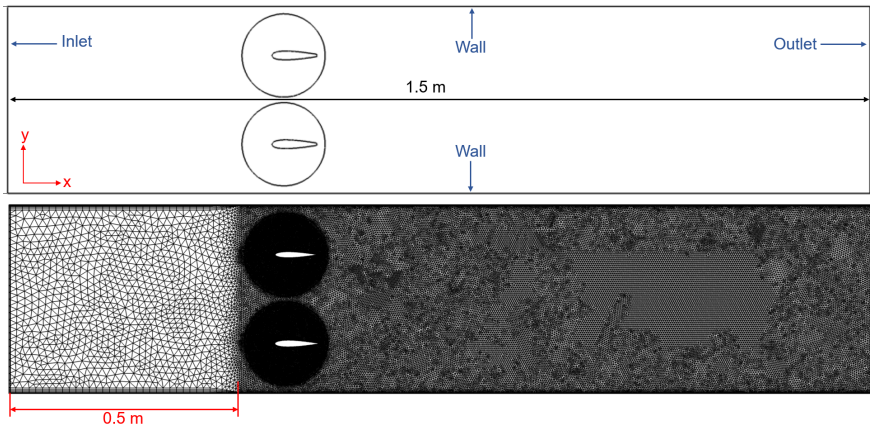


Figure 2.5: Boundary conditions, domain specifications (top), and mesh grid used in the simulations (bottom).

Sinusoidal motion is imposed on the circular regions surrounding the airfoils while a

constant velocity boundary condition is utilized at the inlet. Selected mesh methods are diffusion-based smoothing with a diffusion parameter of 1.5 and remeshing. The two circular regions are then defined as dynamic mesh regions governed by a simple harmonic motion with their center of gravity positioned at the quarter chord of each airfoil.

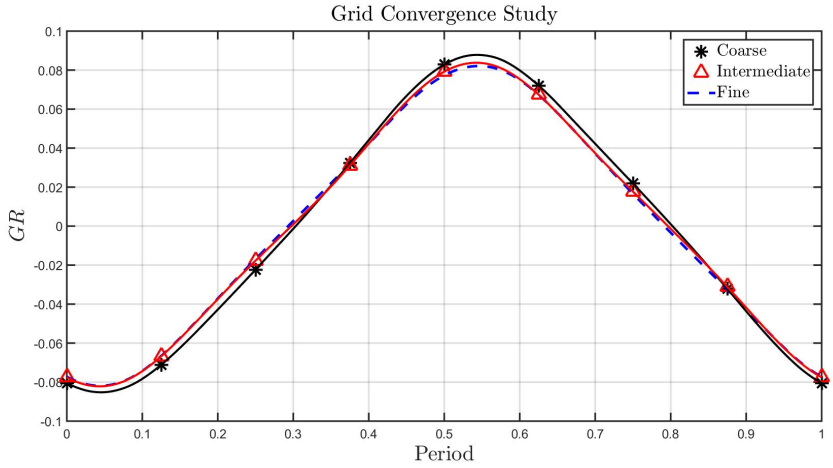


Figure 2.6: Grid convergence study performed with three grids of different sizes.

The computational grid consists of triangular elements with increased refinement around the airfoils, in the dynamic mesh regions, and the wake region. Mesh elements with larger edge lengths are utilized upstream of the gust vanes, due to concerns regarding the computational power and time. As the region of interest is downstream of the gust vanes, the rest of the domain is composed of mesh elements with smaller edge lengths. It is also verified that increased refinement upstream of the gust vanes do not alter the properties of the flow field downstream of the gust vanes. Thus, the grid design utilized in the study is suitable to be used in this type of analysis.

Table 2.1: Properties of the grids

Grid	Element number	Minimum edge length [m]
Coarse	32000	3×10^{-4}
Intermediate	110000	7.5×10^{-5}
Fine	420000	1.8×10^{-6}

Wall boundary condition is applied on the top and bottom sides of the domain to introduce the effect of the tunnel walls on the flow. A pressure outlet boundary condition is applied at the outlet of the domain with a turbulence intensity value of 0.5%, which is a property of the wind tunnel.

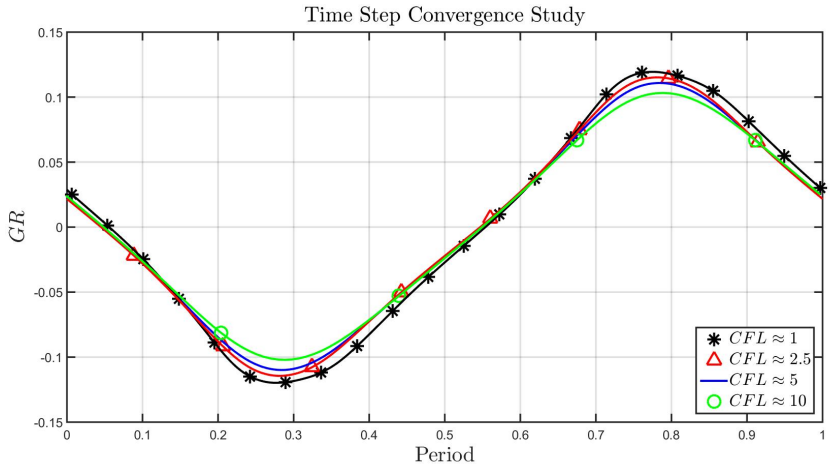


Figure 2.7: Results of the time-step convergence study.

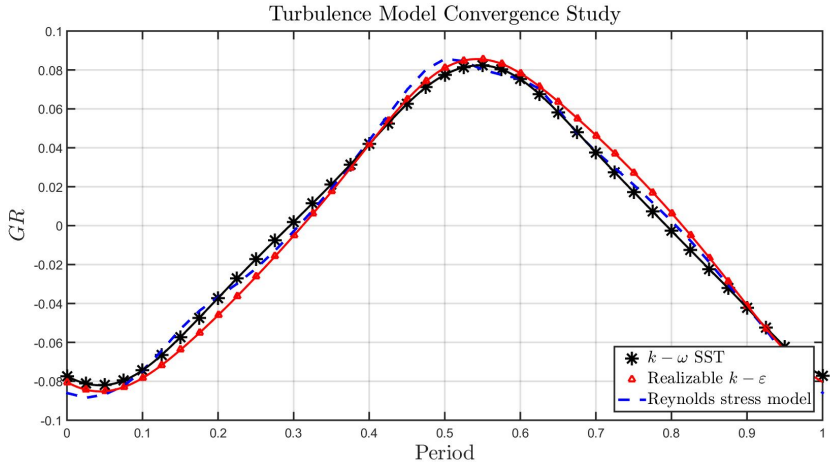


Figure 2.8: Turbulence model convergence study performed with three different turbulence models.

Grid and time step independence studies have been performed and the simulations have been run on the computational mesh with intermediate number of elements, i.e. with 110000 grid points at a CFL number close to 1.0. The intermediate grid is chosen as the difference between the results obtained with fine and intermediate grids are very

close and the grid is converged. Three different turbulence models have been tested (i.e., the $k-\omega$ SST, realizable $k-\varepsilon$ with enhanced wall treatment, and the Reynolds stress model) and compared with the initial experimental results. Consequently, the Reynolds stress model is selected for further simulations.

Initialization is done with a steady state solution while a simple scheme is utilized for pressure-velocity coupling. Then, transient solution is obtained with a coupled scheme for pressure-velocity coupling and transient formulation is second order implicit.

2.2.2.1 Validation of the CFD Methodology

To validate the CFD methodology and verify the reliability of the CFD results, a validation study is performed. Modifying the geometry to replicate the gust generator built for the Open Jet Facility in Delft University [28], and imposing the motion kinematics utilized in the particular study, CFD runs are performed.

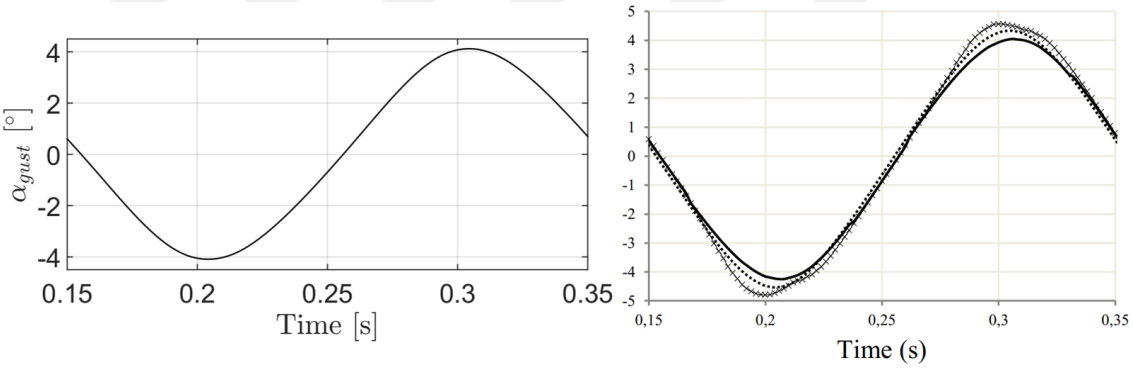


Figure 2.9: CFD results of the gust generator in the Open Jet Facility in Delft University obtained via the current methodology (left) and the study [28] (right). Full line in the right plot stands for the case with $d = 0.7\ m.$ $c = 0.3$ m, $V_{ref} = 25$ m/s, $f = 5$ Hz and $\delta_{max} = \pm 10°$.

The results demonstrated in the study itself are very much in agreement with the results obtained via the current methodology. Variation of the flow angle in time is investigated for the case when the chord length of the vanes is 0.3 m and the vane spacing is 0.7 m.

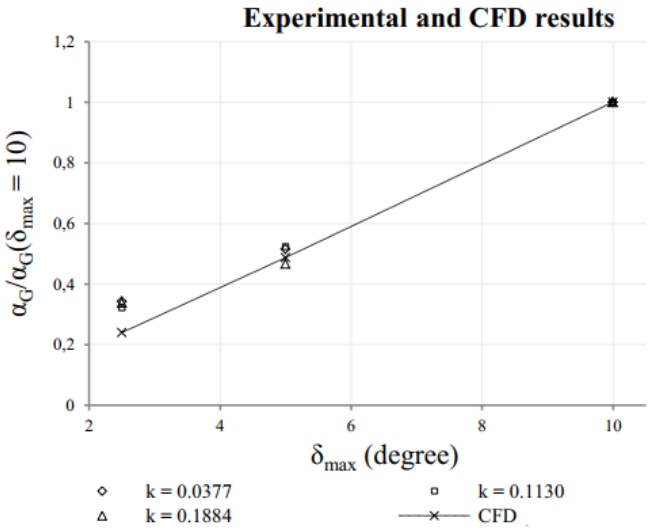


Figure 2.10: Comparison of the experimental and CFD results demonstrated in [28].

Comparing the results obtained with the current grid and CFD methodology (Figure 2.9, left), to the ones shown in Figure 2.9 on the right with a full line, it is observed that there is a great agreement in between. Both periodic waves go to a minimum that is slightly lower than $-4°$ and a maximum of around $4°$. When the time is equal to 0.15 s, both analyses indicate a gust angle value of 0.5°. Moreover, comparison of the CFD results with the experimental results shown in Figure 2.10 also indicates a remarkable agreement. CFD results are obtained for the case when $k = 0.1884$, for which the experiments yield in very similar gust angle values.

Thus, the methodology adopted for CFD analyses, the computational domain design with the grid and the boundary conditions are validated to be utilized in further studies.

2.2.2.2 CFD Analyses for the Characterization of the Gust Generator

CFD runs are performed at different reduced frequency values and the resulting maximum gust ratio is calculated for each case. Different reduced frequency values are obtained by changing the pitching frequency or the freestream velocity, for which the ranges are limited by the capacity of the wind tunnel and the motors driving the gust vanes. The distance between the gust vanes is set to be $2c$ in the numerical simulations.

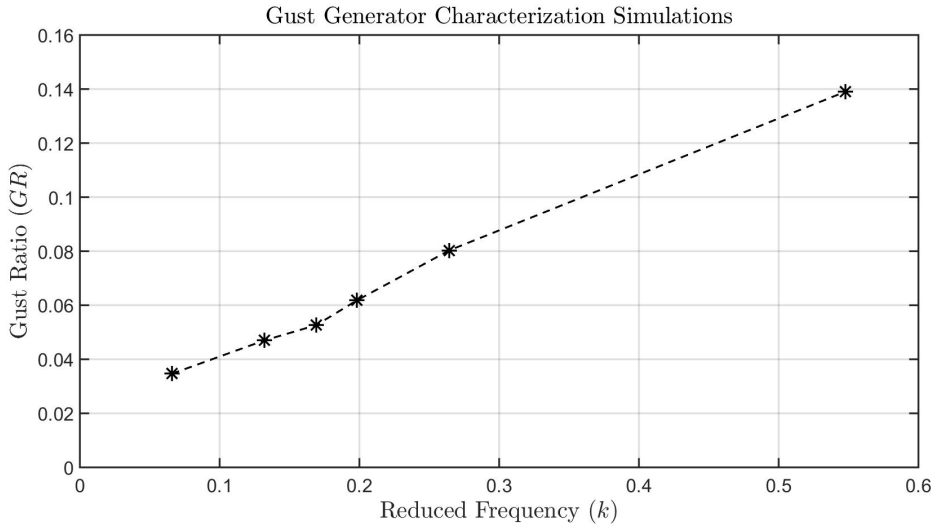


Figure 2.11: The maximum gust ratio values 3 chords downstream of the trailing edge of the gust vanes for different reduced frequencies.

Regarding the reduced frequency, to stay inside the ranges of operation of the wind tunnel and the two-vane gust generator and generate a transverse gust of sufficient amplitude, 0.25 is chosen as the baseline case. This corresponds to a pitching frequency of 10 Hz and a freestream velocity of 10 m/s.

2.2.3 Experimental Investigation of the Gust Generator

To fully characterize the flow field parameters downstream of the gust generator, phase-locked 2D2C PIV measurements are performed. Primarily, measurements for the baseline case are conducted. The baseline case corresponds to a pitching frequency of 10 Hz, a freestream velocity of 10 m/s, and a vane spacing of $2c$. The gust vanes undergo a sinusoidal flapping motion without any phase difference.

After the comparison of the baseline case with CFD results, phase-locked 2D2C PIV measurements for other reduced frequency, vane spacing, and maximum pitching amplitude values are also performed for complete characterization of the gust generator. In other words, in addition to changing the pitching frequency and the freestream velocity, distance between the vanes, and maximum pitching amplitude are also changed and the resulting flow field is investigated.

Table 2.2: Test matrix

Case	f [Hz]	U_∞ [m/s]	k	$\bar{\theta}$	Spacing
1	2.5	10	0.06	12°	$2c$
2	5	5	0.25	12°	$2c$
3	5	10	0.12	12°	$2c$
4	7.5	10	0.18	12°	$2c$
5	10	5	0.50	12°	$2c$
6	10	10	0.25	12°	$2c$
7	10	15	0.16	12°	$2c$
8	10	10	0.25	8°	$2c$
9	10	10	0.25	16°	$2c$
10	10	10	0.25	12°	$1c$
11	10	10	0.25	12°	$2.5c$

In order to conduct phase-locked PIV measurements, the laser is externally triggered by a Transistor-Transistor-Logic (TTL) signal produced by the motors at desired phase angles. Triggering is done at 4° intervals beginning from 0° for every period. Sampling point locations for a period of motion are shown in Figure 2.12.

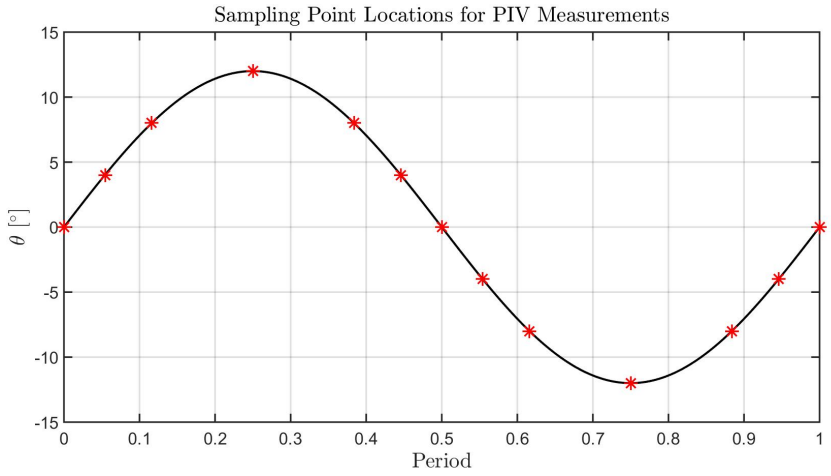


Figure 2.12: Sampling point locations demonstrated on a period of motion.

2.2.3.1 Flow Field Measurements via Particle Image Velocimetry

Phase-locked two-dimensional two-component (2D2C) particle image velocimetry (PIV) measurements are carried out in two measurement windows downstream of the gust generator. The system is composed of a Phantom v641 high speed camera with a Nikon-Nikkor 60 mm lens, a New Wave Solo PIV Nd:YAG laser, a Dantec Dynamics timer box and DynamicStudio® data acquisition and analysis software. The laser beam is first emitted from the laser head in the transverse direction and is then directed upwards along the test section with the help of a mirror. Afterward, it passes through a spherical and a cylindrical lense to be converted into a laser sheet of 2 mm thickness. The laser sheet is in xy plane and is at the center of the test section in z direction. The flow is seeded with fog of droplets with a mean diameter of 1 μm. The field of view (FOV) size is 166 $\times$ 256 mm^2. For each phase, 100 image pairs are acquired and statistically averaged in order to decrease the uncertainty levels for the presented mean values. Double-frame particle images are pre-processed by subtraction of the image minimum in order to enhance the image quality and remove any background noise. Then, using a two-step adaptive-correlation analysis with the final interrogation window size of 64 $\times$ 64 px^2 and a 50% overlap, a vector spacing of 3.32 mm is obtained in the resulting vector maps. Details of the experimental parameters are demonstrated in Table 2.3.

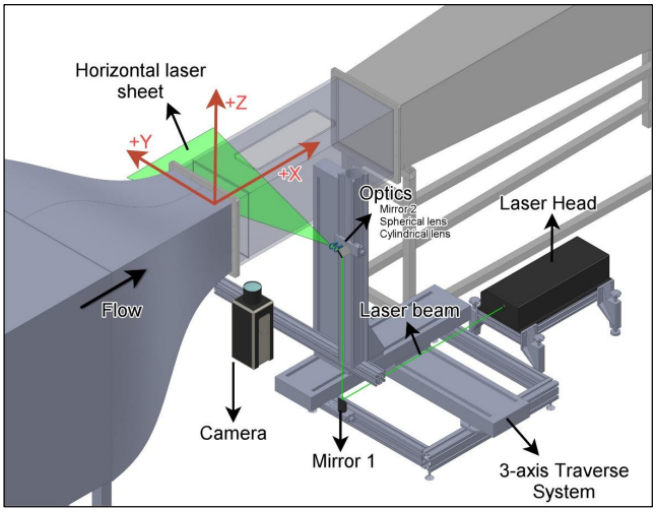


Figure 2.13: PIV measurement setup.

Table 2.3: PIV experimental parameters

Seeding	Type	Fog droplets
	Nominal diameter	1μm
	Seeding generator	Safex fog generator
Laser	Laser type	Nd:YAG
	Manufacturer	New Wave Research
	Model	Solo 120XT
	Maximum Energy	120 mJ/pulse
	Wavelength	532 Nm
	Thickness	2 mm
	Maximum repetition rate	21 Hz
Optics	Mirrors	Dielectric mirror, 532 Nm
	Spherical lens	Plano-convex, 500 mm FL
	Cylindrical lens	Plano-concave, -6.4 mm FL
Camera	Sensor type	CMOS
	Sensor resolution	2560×1600 pixel^2
	Sensor size	25.6×16.0 mm^2
	Pixel pitch	10μm
	Depth	12 bit
	Internal memory buffer	16 GB
Camera lens	Manufacturer	Nikon
	Focal length	60 mm
	$f\#$	5.6
Imaging	Image magnification	0.0967
	Field of View (FOV)	166×256 mm^2
	Camera-object distance	650 mm
	Time between pulses	76 μs
Data analysis	Correlation method	Adaptive cross-correlation
	Interrogation area	64×64 px^2
	Overlap	50%
	Post-processing	Universal outlier detection
	Vector spacing	3.32 mm

2.2.3.2 Measurement Procedure

To characterize the flow field induced by the gust generator, several parameters such as the freestream velocity, pitching frequency, distance between the gust vanes, and the maximum amplitude of motion are varied and phase-locked 2D2C PIV measurements are carried out. In the measurements, the velocity in the test section is adjusted by controlling the driver frequency of the wind tunnel. A Pitot-static tube is placed at the end of the contraction section to measure the flow velocity. Total and static pressure values are recorded via a 64-channel Ethernet intelligent pressure scanner with an accuracy of 0.20% of the full-scale range (4 inch H_2O). Barometric pressure and temperature values of the laboratory are also recorded during the measurements. The freestream velocity is then calculated using the Bernoulli equation and the ideal gas law. While the motors undergo a sinusoidal motion, the laser is triggered externally at certain phases of the motion utilizing the digital I/O module connected to the cRIO and a synchronizer. The laser, camera and the optical equipment (mirrors and lenses) are placed on a traverse mechanism which is free to move in three axes. At each measurement window, all PIV equipment move with the traverse system such that all experimental parameters remain identical.

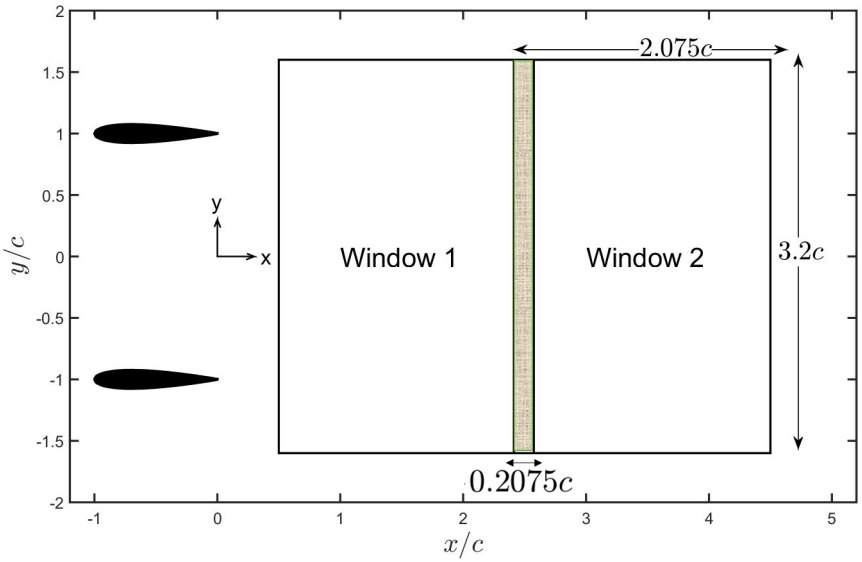


Figure 2.14: PIV measurement domain showing the windows with the overlap region and the field of view dimensions.

The origin is located at the trailing edge of the gust vanes in the freestream direction,

and at the midpoint of the two gust vanes in the transverse direction. In z direction, it is at the center of the test section as shown in Figure 2.1. Two measurement windows with an overlap of 10% are captured in the measurements, where the first window starts at $0.5c$ downstream location of the trailing edge of the gust vanes as demonstrated in Figure 2.14.

2.2.3.3 Data Analysis

Image analysis is performed in DynamicStudio®, where pre-processing is applied to raw images to reduce the background noise. To do this, the image minimum is subtracted from all images before any further processing. It is then followed by an adaptive cross-correlation in three steps with a final interrogation window size of 64 $\times$ 64 px^2. Utilizing 50% overlap between the interrogation windows results in a resolved field of view of 166 $\times$ 256 mm^2 with a vector resolution of about 3.32 mm, corresponding to 49 $\times$ 79 vectors. The statistically averaged flow fields are then exported as data files for further analysis using MATLAB.

2.2.3.4 Uncertainty Analysis

Velocity vectors are obtained utilizing PIV technique, which works by dividing the particle displacement between two consecutive frames by the time separation of the two frames. Quantification of PIV uncertainty is performed utilizing the basic equation used in the technique.

$$U = \frac{\Delta x}{\Delta t} \tag{2.4}$$

Then, uncertainty in the velocity vectors can be calculated as:

$$\varepsilon_U = \sqrt{\left(\frac{\partial U}{\partial \Delta t}\varepsilon_{\Delta t}\right)^2 + \left(\frac{\partial U}{\partial \Delta x}\varepsilon_{\Delta x}\right)^2} \tag{2.5}$$

The uncertainty in Δt, i.e., laser pulse separation, is typically on the order of 1 ns [44], resulting in a negligible relative uncertainty [45]. Moreover, the uncertainty in Δx is indicated to be 0.05-0.1 pixel according to many experimental studies [46]. In

this regard, uncertainty in velocity vectors can be calculated.

$$\varepsilon_U = \sqrt{\left(-\frac{\Delta x}{\Delta t^2}\varepsilon_{\Delta t}\right)^2 + \left(\frac{1}{\Delta t}\varepsilon_{\Delta x}\right)^2} \tag{2.6}$$

Rearranging,

$$\frac{\varepsilon_U}{U} = \sqrt{\left(\frac{\varepsilon_{\Delta t}}{\Delta t}\right)^2 + \left(\frac{\varepsilon_{\Delta x}}{\Delta x}\right)^2} \tag{2.7}$$

The highest suggestion for the uncertainty in the particle displacement (0.1 pixel) is substituted to be on the conservative side. The particle displacement for the set pulse separation equals to 8 pixels.

$$\frac{\varepsilon_U}{U} = \frac{0.1}{8} = 1.25\% \tag{2.8}$$

Consequently, uncertainty in velocity vectors equals to 1.25%.

2.3 Application

To assess the capability of a porous disk in mimicking the wind turbine wake in a gusty inflow condition, as an application, the flow in the wake of a porous disk is compared with that of a model wind turbine subjected to a sinusoidal transverse gust. Actuation parameters of the gust vanes are identical to the baseline case ($f = 10$ Hz, $U_\infty = 10$ m/s, $d = 2c$ and $\bar{\theta} = 12°$).

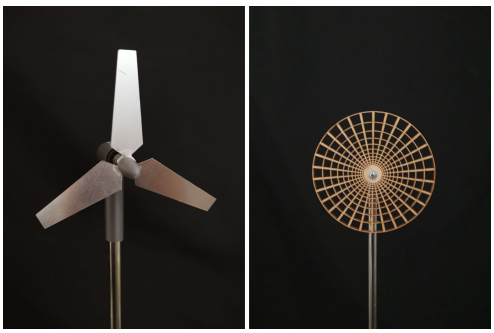


Figure 2.15: The model wind turbine (left) and the porous disk (right).

The porous disk and model wind turbine which are tested under transverse gust conditions have a diameter of 0.12 m and a thrust coefficient, C_T , of 0.82 at a Reynolds number of 78000. The porous disk has a radially non-uniform porosity distribution

Table 2.4: Properties of the models

Properties	Model Turbine	Porous Disk
Taper distribution	Linear	-
Material	Aluminum	Plywood
Porosity	-	Non-uniform
Thickness	0.5 mm	4 mm
Diameter	120 mm	120 mm
Mast diameter	10 mm	10 mm
Hub diameter	10.2 mm	10.8 mm

specifically designed to mimic the rotor [41]. The model wind turbine blade has a linearly tapered cross-section with 22° twist angle at the root and 15° at the tip section. Blades are fabricated from an aluminum sheet, which is cut and pressed to obtain the desired taper and twist distribution. Nacelle and hub parts are 3D printed using PLA+ filaments and a brushless DC motor is integrated inside the nacelle to drive the turbine blades in rotating motion.

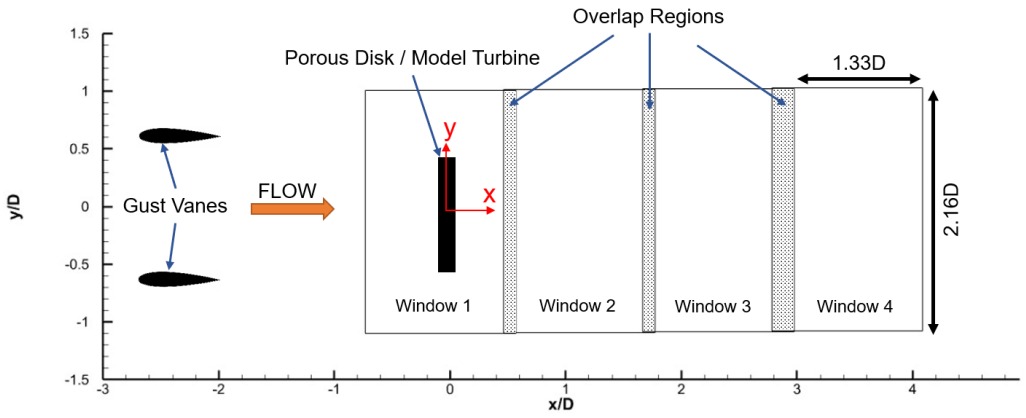


Figure 2.16: PIV measurement domain showing the windows with the overlap region and the field of view dimensions.

Figure 2.16 shows the position of the wind turbine/porous disk with respect to the gust generator as well as the locations of the fields of view that are captured in the PIV measurements. For these measurements, the final interrogation window size is

32×32 px^2, corresponding to a vector resolution of 1.6 mm. Other measurement parameters and procedure are identical to those of the characterization experiments. Each rectangular window represents a FOV in the x-y plane. There is 10% overlap between the first three windows, while 16.25% overlap exists between window 3 and window 4 due to limitations in the traversing mechanism. 10% overlap corresponds to $0.13D$ and is resolved by around 5 vectors. Wake measurements are performed up to around 4.2 diameters downstream of the wind turbine and porous disk by combining multiple PIV measurement windows.

CHAPTER 3

RESULTS AND DISCUSSION

Results of the experimental and computational studies are presented and discussed in this chapter. Both temporal and spatial variations in the flow field are explored. Spatial behavior of the flow field is demonstrated in the form of contour plots of a number of flow properties for some selected phases of a period of the motion of the gust vanes. Temporal behavior, on the other hand, is analyzed for each phase of the motion at a fixed downstream location at the center of the two vanes.

Effects of changing several actuation parameters and the distance between the vanes on the resulting gusty flow are investigated. Reduced frequency is varied by varying the pitching frequency and freestream velocity separately. It is aimed to explore if any relation between any of the two parameters and resulting gust flow exists, or if the reduced frequency is the only parameter affecting the gust generated. Effect of changing Strouhal number is another parameter studied, which depends on the amplitude of the pitching motion. Finally, the vane spacing, i.e., the distance between the vanes, is varied and the resulting flow field is studied both in a spatial and a temporal manner. In the end, it is aimed to fully quantify the dependency and sensitivity of the gust generator to any of these parameters and obtain the information about the temporal and spatial character of the gust flow under all conditions.

After the characterization studies, a model wind turbine and a porous disk having the same thrust coefficient are placed $3c$ downstream ($x/c = 3$) of the gust generator. The reason why the models are placed at this certain location is that CFD results indicate that at $x/c = 3$, the gust flow reaches a sufficient magnitude and is uniform. Wake flows of the two models are then compared under a transverse gust loading, to test the capability of the porous disk in mimicking the wake of a wind turbine under a

gusty inflow condition. The gusty inflow the models are sujected to is identical to the baseline case in terms of actuation parameters, i.e., $f = 10$ Hz, $U_\infty = 10$ m/s, $\bar{\theta} = 12^\circ$ and $d = 2c$.

Contour plots of all the phases of a period of motion are presented in the Appendix A.

3.1 Variations in the Gust Ratio

To parametrize gust flows and quantify the severity of gust, one commonly used parameter is the gust ratio [6]. It is defined as the ratio of the gust velocity to the freestream velocity. Hence, the transverse gust ratio is expressed as:

$$GR = \frac{v}{U_\infty} \tag{3.1}$$

The streamwise gust ratio is expressed as:

$$GR = \frac{u}{U_\infty} \tag{3.2}$$

where u is the gust velocity, and equals to:

$$u = U - U_\infty \tag{3.3}$$

Consequently, severity and magnitude of gusts are quantified by the gust ratio (GR). For all the test cases demonsrated in Table 2.2, which are composed of different reduced frequencies, actuation parameters, vane spacing, etc., the variation of maximum gust ratio is investigated.

Reduced frequency variation is done through altering the pitching frequency and the freestream velocity separately, in order to observe if any relation between one of the parameters to the maximum gust ratio exists, or if the reduced frequency is the only parameter affecting the magnitude of the resulting gust. The results are first demonstrated for $x/c = 3$ location, as it is the point where the models are placed.

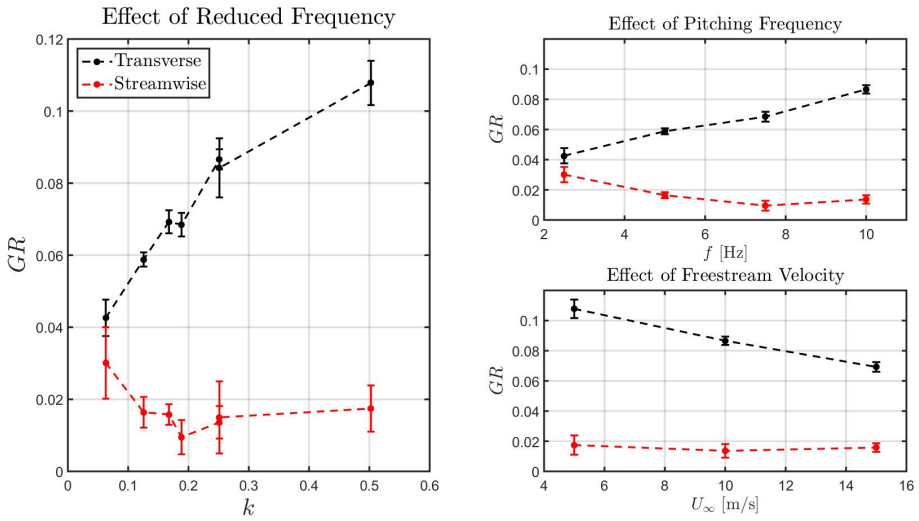


Figure 3.1: Maximum transverse and streamwise gust ratio values at $x/c = 3$ for different reduced frequencies. Effect of varying pitching frequency and freestream velocity while other actuation parameters are identical, are also shown.

It is depicted in Figure 3.1 that with increasing pitching frequency, there is an increase in the transverse gust ratio. On the other hand, with increasing freestream velocity, there is a decrease in the transverse gust ratio. These trends are very well expected, as an increase in the pitching frequency, as well as a decrease in the freestream velocity, results in an increase in the unsteadiness of the flow. With an increasing level of unsteadiness, it is expected to have a gust of larger magnitude. Moreover, for the same reduced frequency ($k = 0.2513$) obtained with different actuation parameters, transverse and streamwise gust ratios are almost equal to each other. This indicates that magnitude of gust depends directly on the reduced frequency.

For the streamwise gust, effect of neither pitching frequency nor freestream velocity is not as pronounced as it is for the transverse gust. This is because of the fact that the motion of the gust vanes are in-phase, resulting in the generation of a dominant transverse gust along with a very small streamwise gust.

The trends are similar at $x/c = 2$ location. Effect of pitching frequency and freestream velocity on the transverse gust is more pronounced. An increase in transverse gust ratio is observed with an increasing reduced frequency at this location as well. Also, an increase in the transverse gust ratio is observed with an increase in the pitching

frequency and a decrease in the freestream velocity.

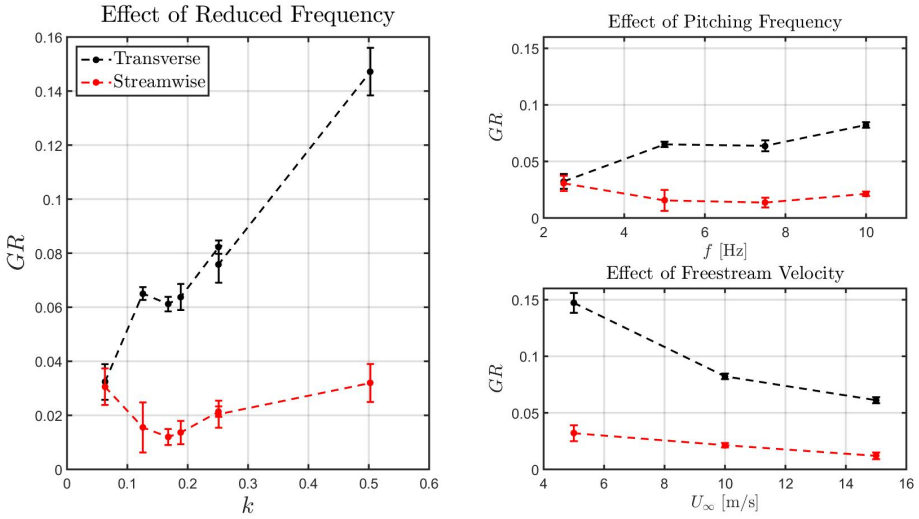


Figure 3.2: Maximum transverse and streamwise gust ratio values at $x/c = 2$ for different reduced frequencies. Effect of varying pitching frequency and freestream velocity while other actuation parameters are identical, are also shown.

Another important flow parameter in describing oscillating flow mechanisms, Strouhal number (St) is also varied and its effect on gust magnitude is observed. Strouhal number is generally utilized in analyzing unsteady, oscillating flow problems, as it is a representation of the measure of the ratio of inertial forces due to unsteadiness of the flow [49]. It is defined as:

$$St = \frac{fL}{U_\infty} \tag{3.4}$$

where L is the characteristic length in the problem of interest. For this study, L is set to be the distance traveled by the trailing edge of a single vane. Hence, the effect of motion amplitude is included in the the investigation.

$$L = \sin\bar{\theta}\frac{3c}{4} \tag{3.5}$$

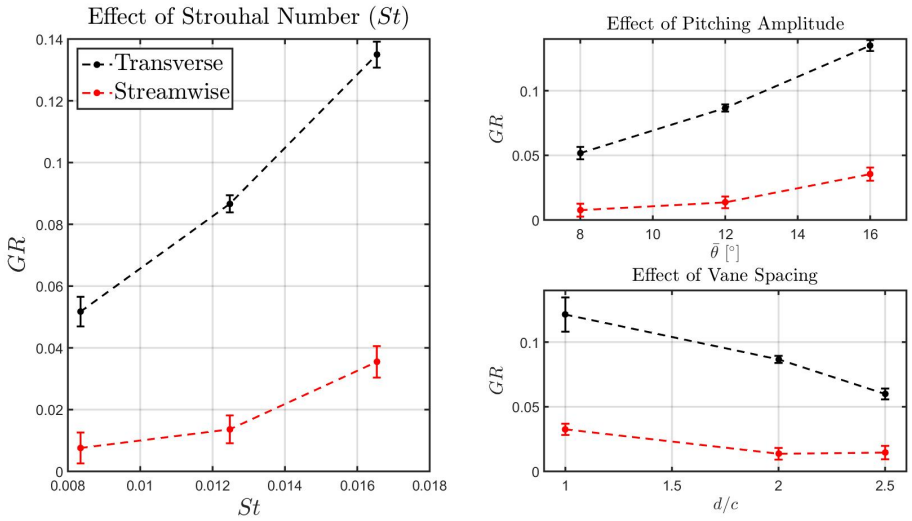


Figure 3.3: Maximum transverse and streamwise gust ratio values at $x/c = 3$ for different Strouhal numbers. Effect of varying pitching amplitude and vane spacing while other actuation parameters are identical, are also shown.

Variation trends in the transverse and streamwise gust ratios are similar for changing pitching amplitude and vane spacing. With an increase in the pitching amplitude, both transverse and streamwise gust ratios demonstrate an increasing behavior. This is because of the fact that an increase in the amplitude corresponds to an increase in the magnitude of the disturbance introduced to the flow, which is responsible for the generation of the transverse component of velocity.

On the other hand, with an increase in the distance between the vanes, a decrease is observed in both streamwise and transverse gust ratios. This is because of the fact that for the setup with the minimum vane spacing, change in blockage ratio of the useful working section, i.e. the area under the influence of gust, is more severe. Hence, gusts with larger magnitude are generated.

For the effect of Strouhal number, on the other hand, the trend is the same with amplitude, as the oscillation amplitude is included in the definition. Trends look similar for $x/c = 2$ position. With an increase in the pitching amplitude and a decrease in vane spacing, transverse and streamwise gust ratios increase. Yet, all the cases demonstrate a significant difference in the magnitudes of transverse and streamwise gust ratios. This indicates that the present mechanicsm is successful in generating a

dominant transverse gust with a very small streamwise gust generated as a result of changing blockage ratio.

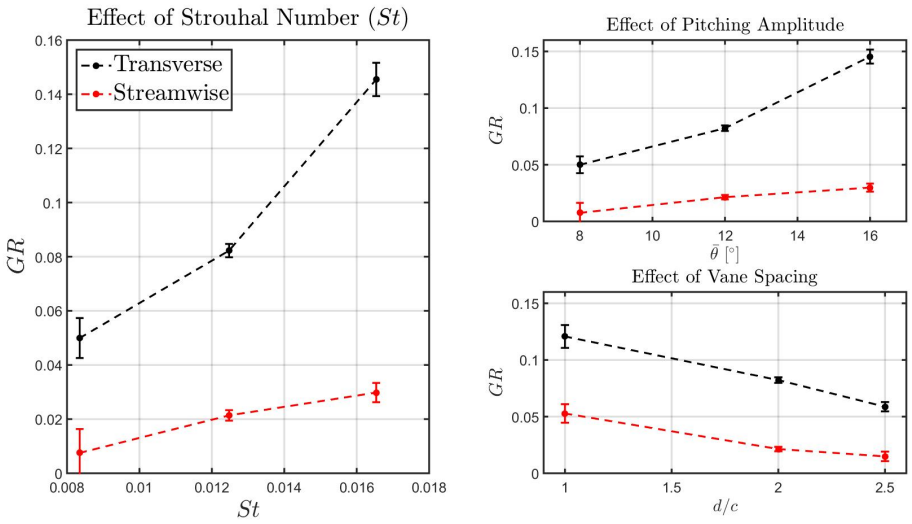


Figure 3.4: Maximum transverse and streamwise gust ratio values at $x/c = 2$ for different Strouhal numbers. Effect of varying pitching amplitude and vane spacing while other actuation parameters are identical, are also shown.

Finally, by calculating the maximum gust ratio values at a certain downstream location, sensitivity of the maximum gust ratio to the actuation parameters and the distance between the vanes can be investigated. Yet, to explore the changes in the gust uniformity and the content of the flow in terms of different flow structures, contour plots should be analyzed.

3.2 Comparison of Numerical and Experimental Results

Along with the phase-locked 2D2C PIV measurements, computational analyses of the gust generator have also been performed. A comparison of the results for the baseline ($f = 10$ Hz, $U_\infty = 10$ m/s, $d = 2c$ and $\bar{\theta} = 12°$) case indicates a good agreement between the CFD and PIV results, both in temporal and spatial sense.

Although the in-phase operation of the two gust vanes is maintained with the purpose of generating a transverse gust, contour plots show that there is a variation in the streamwise velocity component as well as the transverse velocity component. This

variation is attributed to the changing blockage ratio as a result of the pitching motion of the vanes. Thus, flow passage area is varied at each phase of the period, causing a periodic variation in the streamwise velocity.

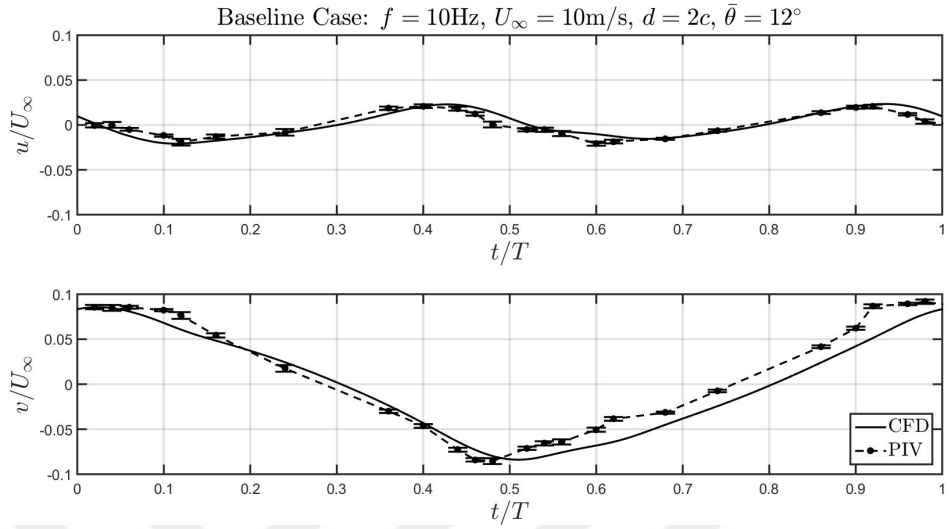


Figure 3.5: Streamwise and transverse gust ratio values at each phase of the period obtained by numerical and experimental studies.

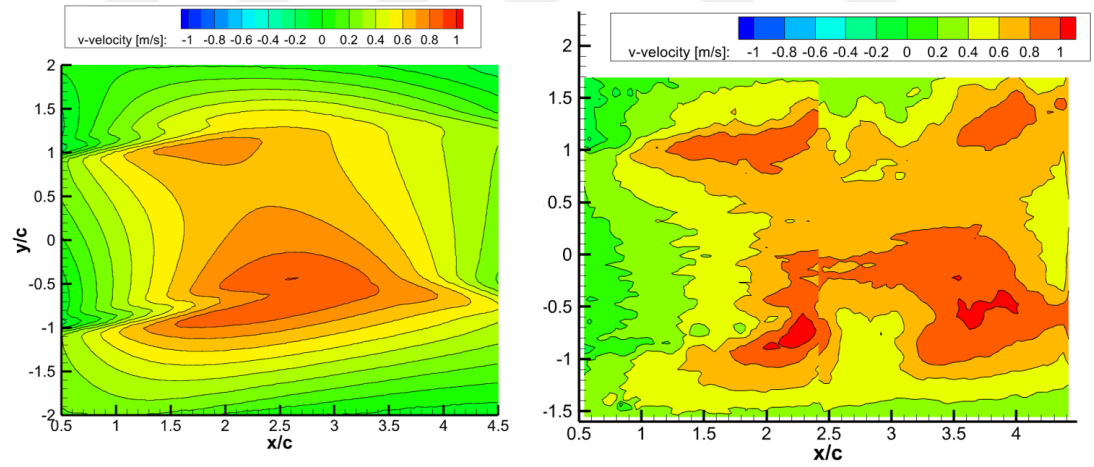


Figure 3.6: Contours of transverse velocity component (v-velocity) obtained via CFD runs (left) and PIV measurements (right), for the phase when $\theta = 0^\circ$ for the baseline case.

Figure 3.5 shows that the CFD approach is actually able to capture the gust ratio and the sinusoidal shape of the gust flow revealed in temporal analysis plots with a very high accuracy. A phase lag is present between the two results, which may stem from

the relatively coarse discretization of the experimental data or a discrepancy in CFD in terms of the freestream velocity encountered by the vanes.

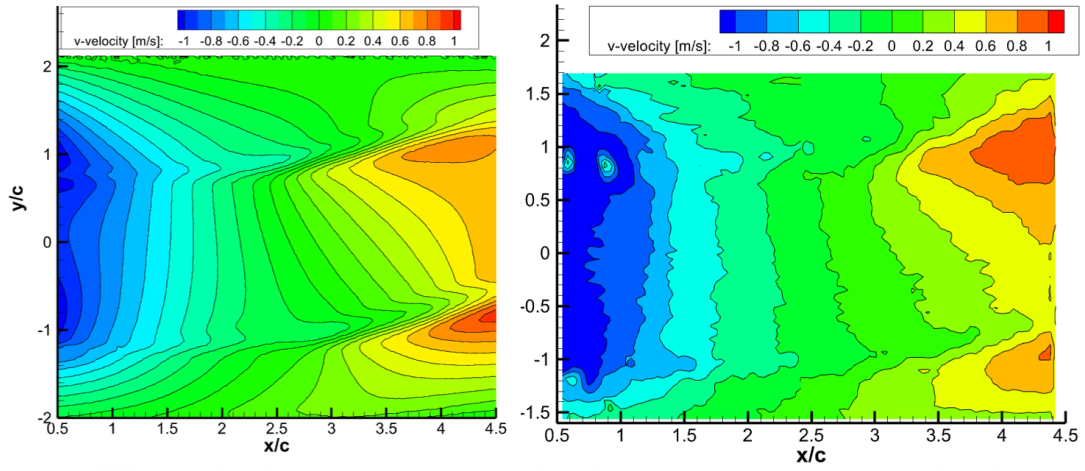


Figure 3.7: Contours of transverse velocity component (v-velocity) obtained via CFD runs (left) and PIV measurements (right), for the phase when $\theta = 12°$ for the baseline case.

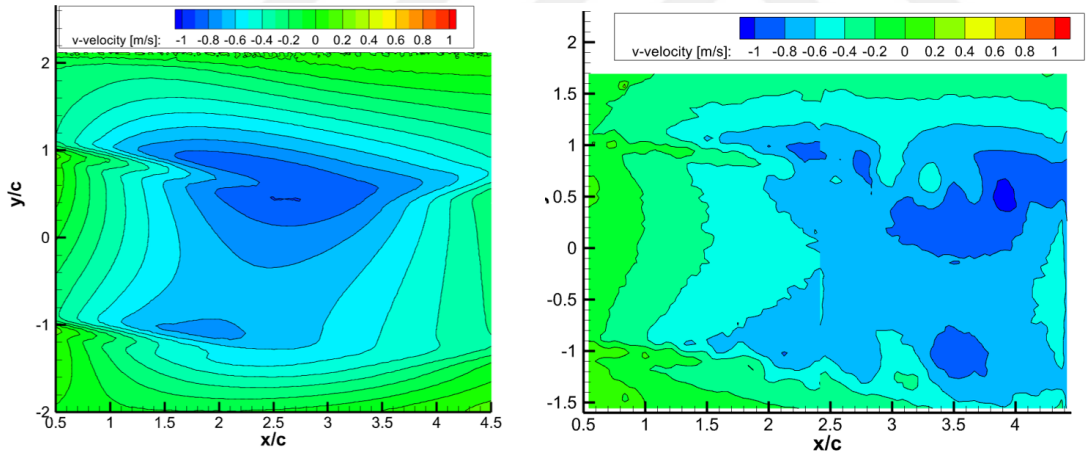


Figure 3.8: Contours of transverse velocity component (v-velocity) obtained via CFD runs (left) and PIV measurements (right), for the phase when $\theta = 0°$ for the baseline case.

Comparison of the results obtained via CFD to experimental results in spatial sense, i.e., in the form of contours, also proves the existence of a relatively small phase lag. Yet, dominant flow structures are captured successfully by the CFD, especially for the cases in which the deflection angle of the wakes are higher, which correspond to

$\theta = 12°$ and $\theta = -12°$.

When the period of motion just begins, i.e. $\theta = 0°$, as revealed in Figure 3.6, the coherent flow region of high transverse velocity exists in CFD as well as PIV. However, CFD calculates a different spatial distribution of the flow structure and local regions of smaller magnitude when compared to experimental results.

At the peak location of the pitching motion, i.e. $\theta = 12°$ (Figure 3.6) coherent regions of non-zero transverse velocity seem to advect downstream. This advection is captured very well by the CFD and the results seem to be in a remarkable agreement.

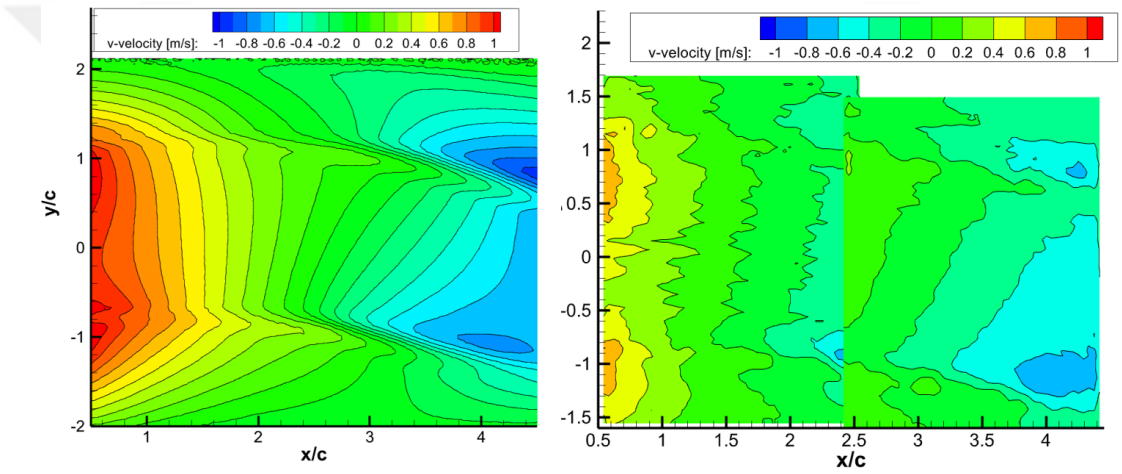


Figure 3.9: Contours of transverse velocity component (v-velocity) obtained via CFD runs (left) and PIV measurements (right), for the phase when $\theta = -12°$ for the baseline case.

The phase difference between the results obtained via CFD and PIV are observed in Figures 3.8 and 3.9. The capability of CFD in terms of capturing the major flow structures are also clear in these results. As a result, it can be deduced that CFD is a very powerful tool especially in a temporal analysis, where the gust ratio is calculated at each phase of the motion at a certain downstream location. This may be an advantage to evaluate the performance of the gust generator and quantify the severity of gust before a model is placed and experiments are conducted.

3.3 Spatial Variations in the Flow Field

Contour plots obtained via PIV measurements of all the test cases demonstrated in Table 2.2 are shown in Figures A.1-A.29 in the Appendix A. In this section, for comparison purposes, only the phases corresponding to the peaks and zeros of a period are demonstrated, for the streamwise and transverse velocity components and out-of-plane vorticity (ζ).

Out-of-plane vorticity is normalized by the pitching frequency for each case and is calculated as:

$$\zeta = \frac{\partial v}{\partial x} - \frac{\partial u}{\partial y} \tag{3.6}$$

3.3.1 Effect of Reduced Frequency

Reduced frequency is varied by varying the pitching frequency and the freestream velocity, while each of the other flow parameters are kept constant. In addition, different actuation parameters can generate the same reduced frequency.

As discussed previously and shown in Figures 3.1 and 3.2, the same reduced frequency yields the same maximum gust ratio, but the content of the flow in terms of flow structures and gust uniformity are actually different. Thus, reduced frequency is not the only parameter in determining the convenience of a case for a model testing under gust loading.

Figure 3.11 reveals similar gust ratio values at the centerline between the two vanes, but completely different flow structures. Some vortex shedding is observed for the case when $f = 5$ Hz and $U_\infty = 5$ m/s, which is not observed in the other case. Thus, gust uniformity is somewhat poorer for the case of lower frequency and freestream velocity, although the reduced frequency values are equal.

The vortex shedding for the case with lower frequency and freestream velocity is observed in Figure 3.12 as well. Thus, caution must be taken while placing a model downstream of the gust generator.

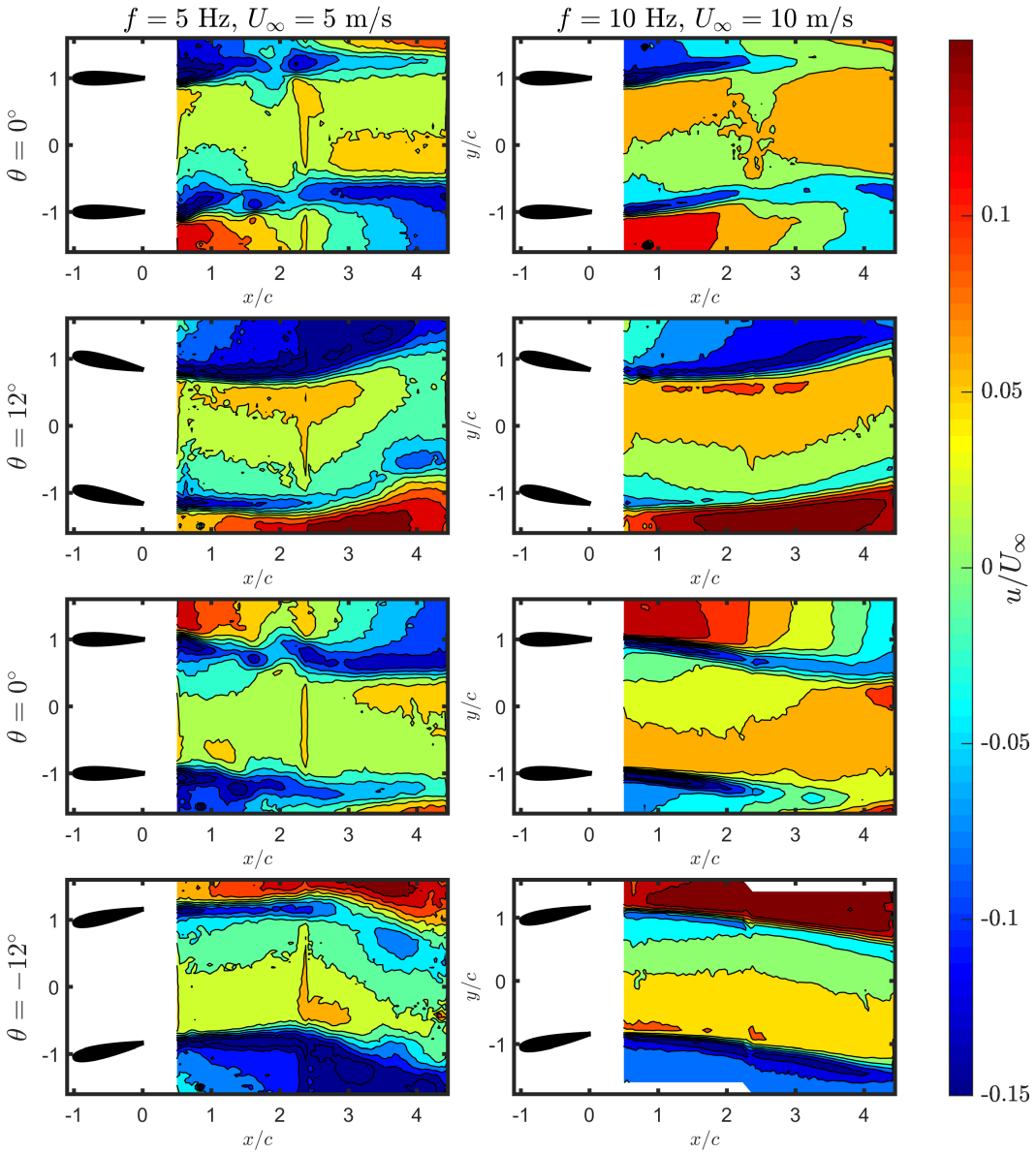


Figure 3.10: Effect of different actuation parameters and the same reduced frequency on the streamwise component of velocity. Columns represent the test cases for which frequency is different and other parameters are identical. Rows represent the phase angle of the period. One period of motion starts from 0°, peaks at θ_{max}, becomes 0° again and goes to minimum (θ_{min}).

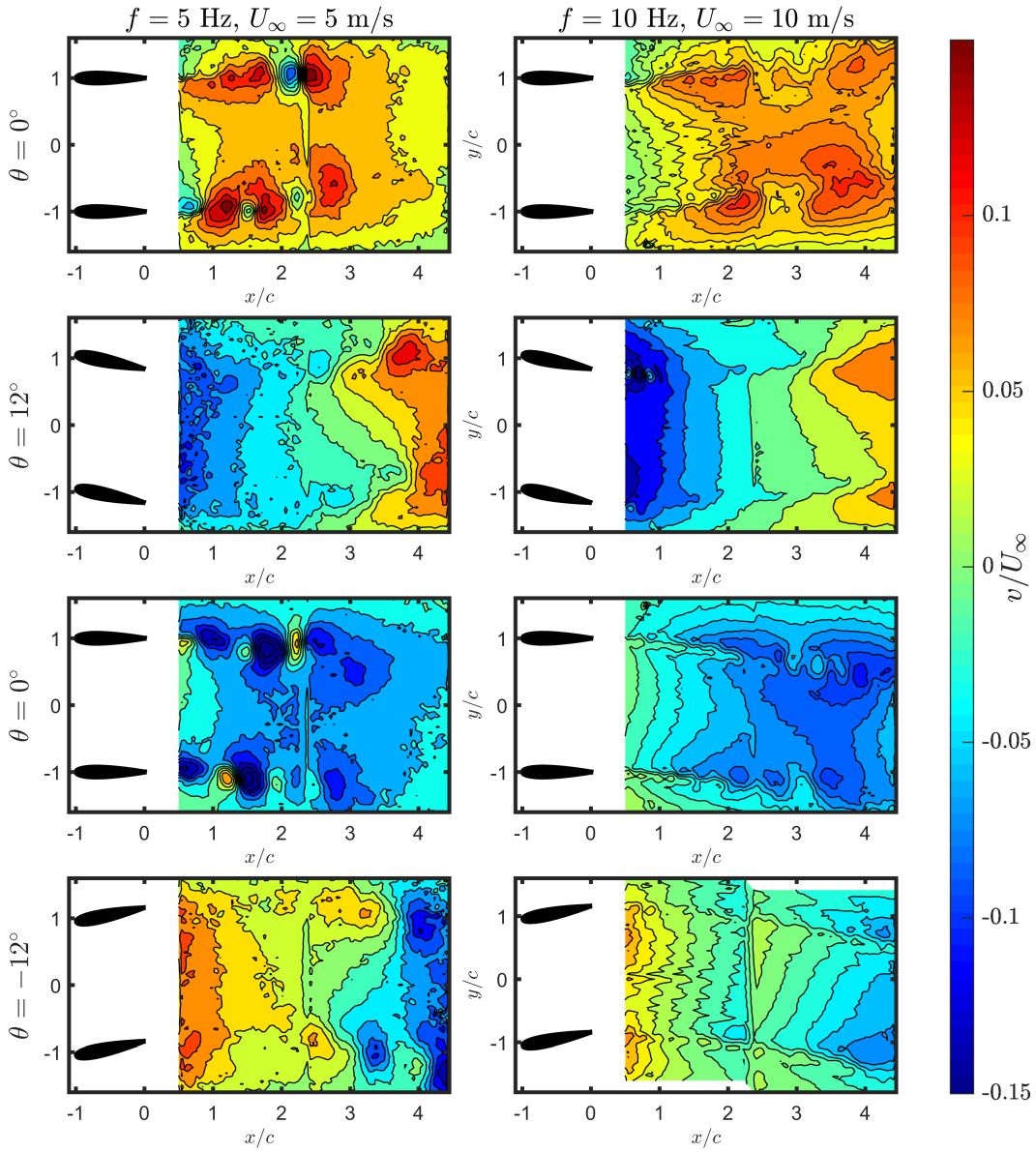


Figure 3.11: Effect of different actuation parameters and the same reduced frequency on the transverse component of velocity. Columns represent the test cases for which frequency is different and other parameters are identical. Rows represent the phase angle of the period. One period of motion starts from 0°, peaks at θ_{max}, becomes 0° again and goes to minimum (θ_{min}).

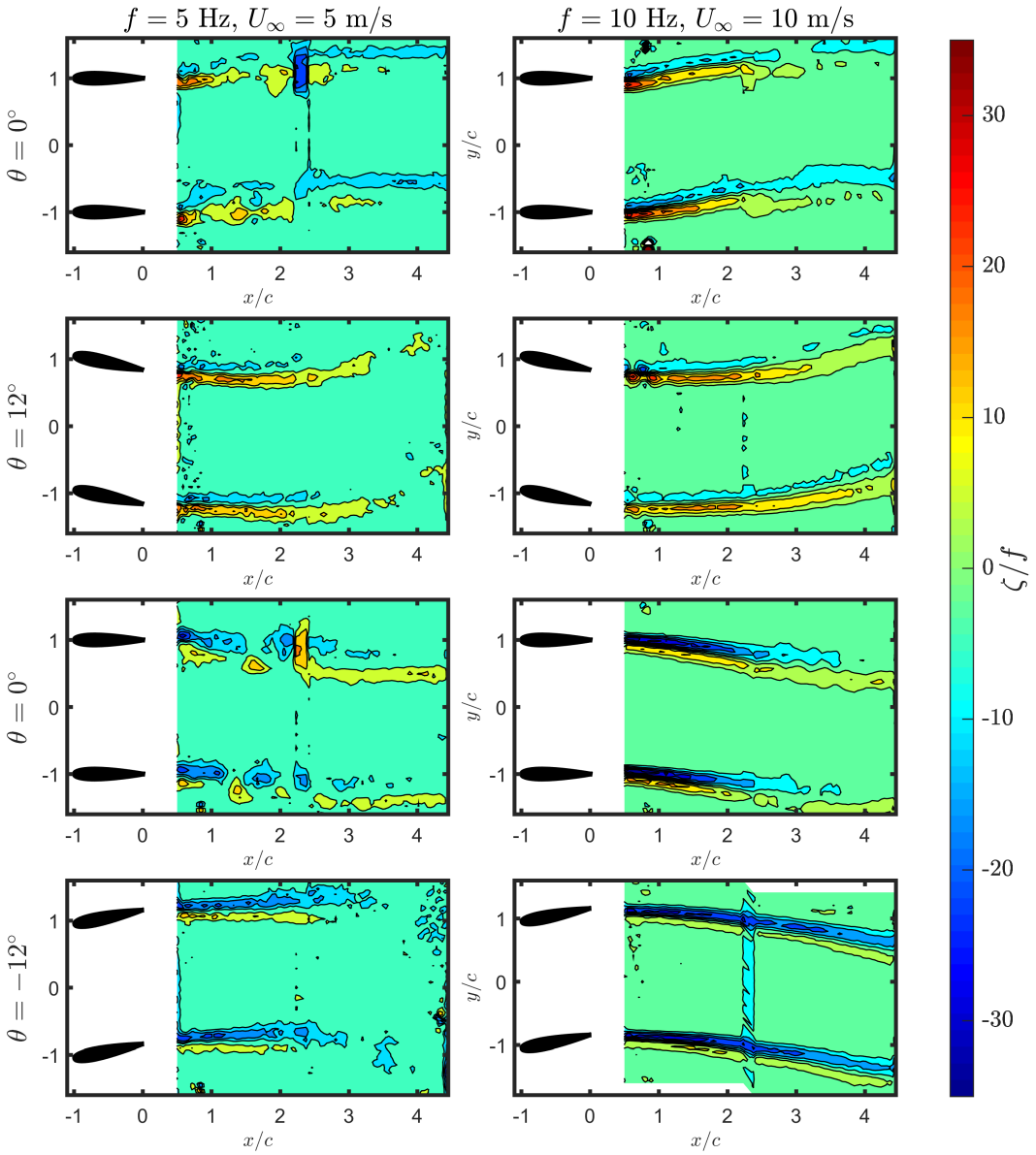


Figure 3.12: Effect of different actuation parameters and the same reduced frequency on out-of-plane vorticity. Columns represent the test cases for which frequency is different and other parameters are identical. Rows represent the phase angle of the period. One period of motion starts from 0°, peaks at θ_{max}, becomes 0° again and goes to minimum (θ_{min}).

3.3.1.1 Effect of the Pitching Frequency

A pitching frequency range of 2.5-10 Hz is selected to examine the effect of pitching frequency on the resulting flow field. The only variable that is changed is the pitching frequency and every other parameter is identical to the baseline case ($U_\infty = 10$ m/s, $d = 2c$ and $\bar{\theta} = 12°$). As shown in Table 1.2, a wide variety of motion frequencies have been tried for the gust generators of other institutions. A minimum of 0.5 Hz and a maximum of 80 Hz have been examined. Yet, to be able to observe a gust of sufficient amplitude and to stay out of the uncertainty range of PIV, a minimum value of 2.5 Hz is selected. To maintain a safe operation of the motors, a maximum of 10 Hz is chosen.

For the streamwise velocity, with an increase in the pitching frequency, the wakes of the vanes become more deflected at related phases of the period, as depicted in Figures 3.13 and 3.14. This indicates that the generated gust flow becomes more severe and affects a larger region downstream of the vanes, as the pitching frequency increases. This is attributed to the increase in the strength of the bound circulation with an increase in the pitching frequency. This stronger bound vorticity results in the generation of a lift force that is greater in magnitude, which is responsible for the higher deflection in the wakes of the vanes with increasing pitching frequency. Patches of relatively high speed streamwise flow appear in the regions between the gust vanes and the test section walls, which are generated as a result of the varying blockage ratio during the pitching motion. This results in a variation in the flow passage area, or the area of the useful working section. Thus, to test models under gust loading, model placement in y direction is critical. The regions where patches of low and high speed appear should be avoided such that the model always stays in the useful working section where gust flow is dominant.

On the other hand, the transverse velocity component displays more homogeneous distributions during the course of the vane pitching motion, as shown in Figures 3.15 and 3.16. Coherent regions of non-zero transverse velocity advect downstream without a significant variation in their topology. Yet, with increasing pitching frequency, regions of high magnitude of transverse velocity increases in terms of area, suggesting an increase in the severity of the gust flow produced. Out-of-plane vorticity (ζ)

contours (Figures 3.17 and 3.18) reveal no direct interaction between the wake vorticity layers of the two vanes, yet, model placement location is important in order to avoid any interaction with the shear layers of the vanes.

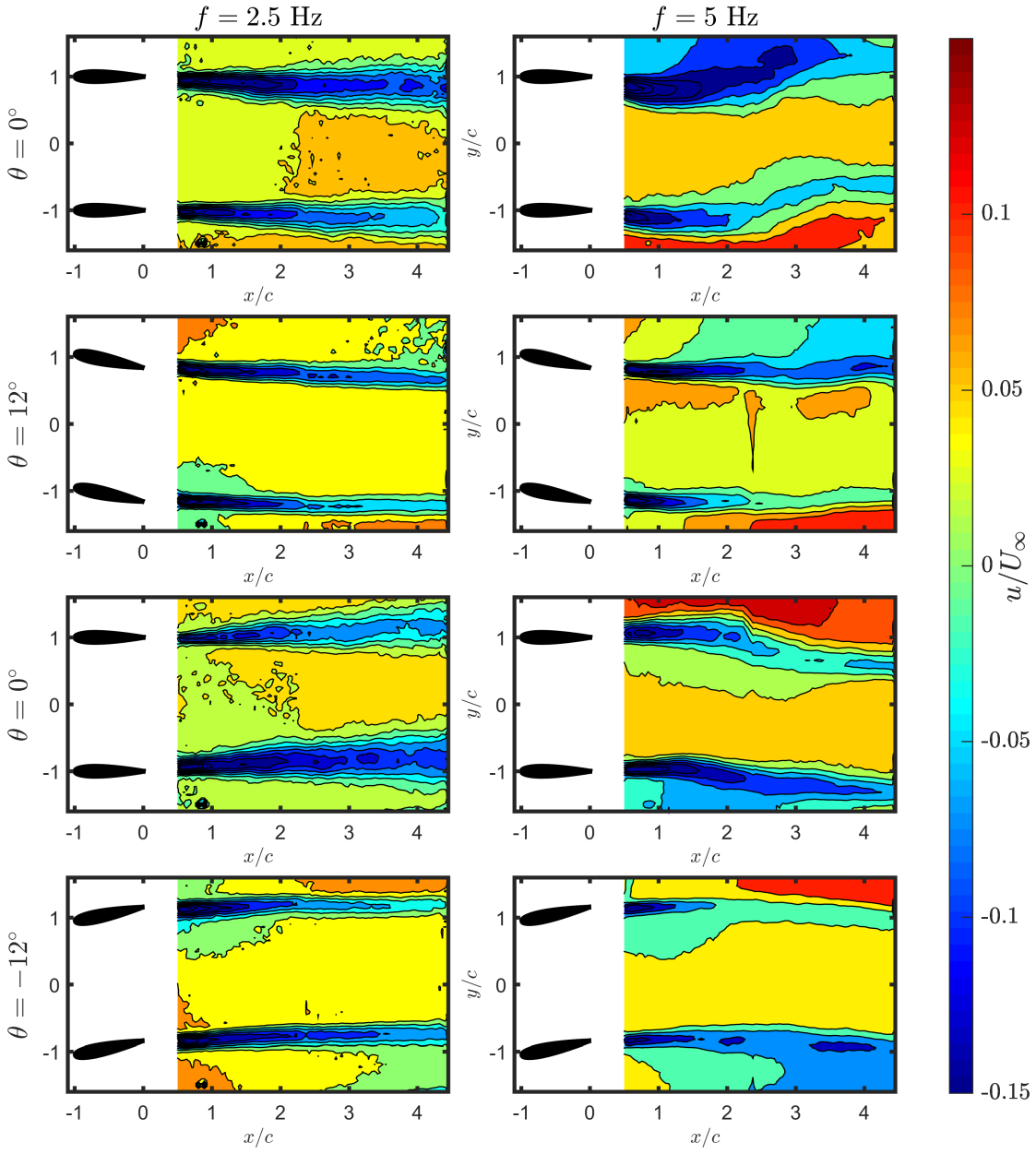


Figure 3.13: Effect of pitching frequency on the streamwise component of velocity. Columns represent the test cases for which frequency is different and other parameters are identical. Rows represent the phase angle of the period. One period of motion starts from 0°, peaks at θ_{max}, becomes 0° again and goes to minimum (θ_{min}).

Furthermore, with an increase in the pitching frequency, i.e., reduced frequency, contours of transverse velocity (Figures 3.15 and 3.16) demonstrate that gust uniformity decreases. Thus, it can be deduced that the increase in the gust magnitude comes with a penalty in uniformity, as the reduced frequency increases.

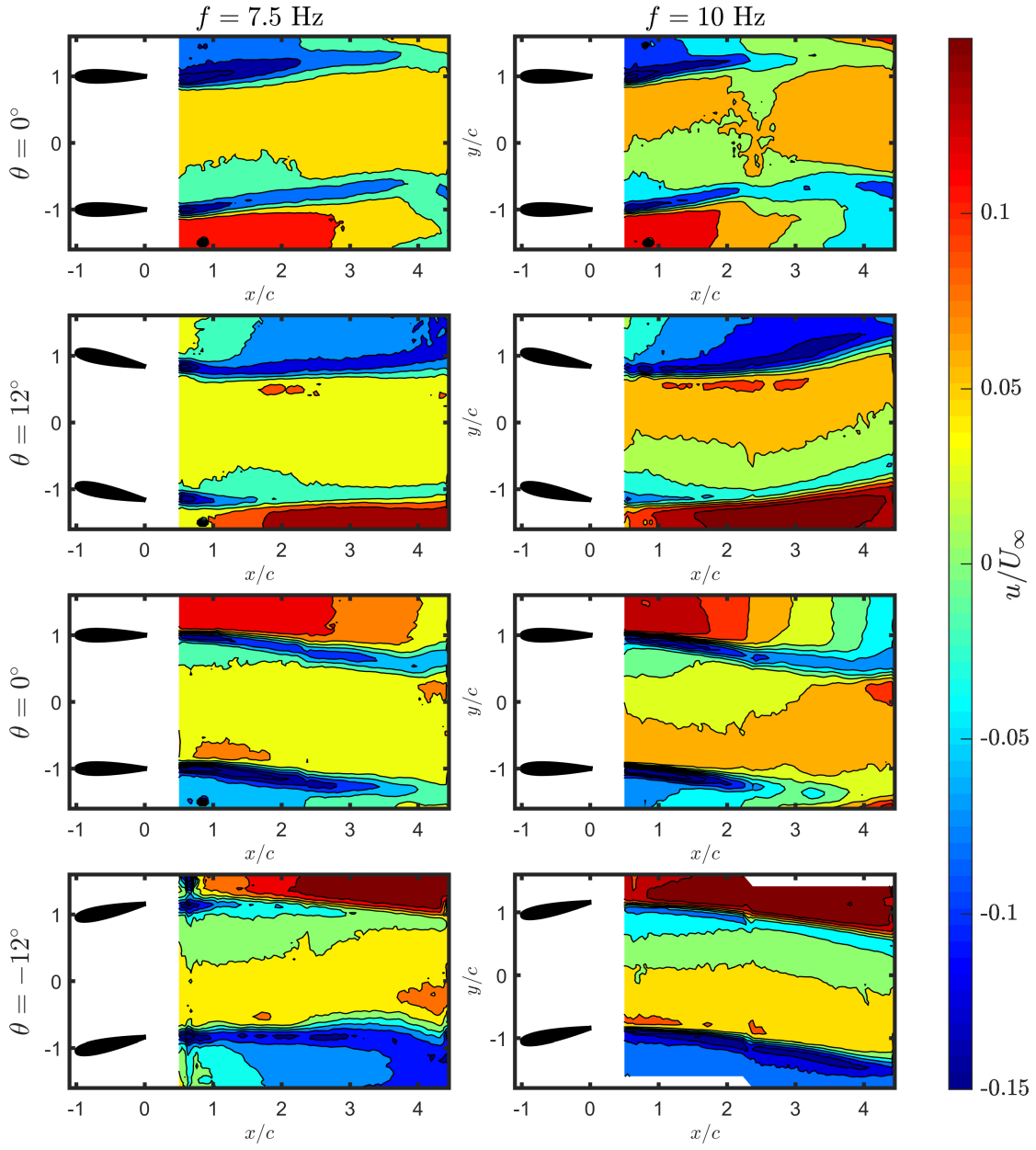


Figure 3.14: Effect of pitching frequency on the streamwise component of velocity. Columns represent the test cases for which frequency is different and other parameters are identical. Rows represent the phase angle of the period. One period of motion starts from 0°, peaks at θ_{max}, becomes 0° again and goes to minimum (θ_{min}).

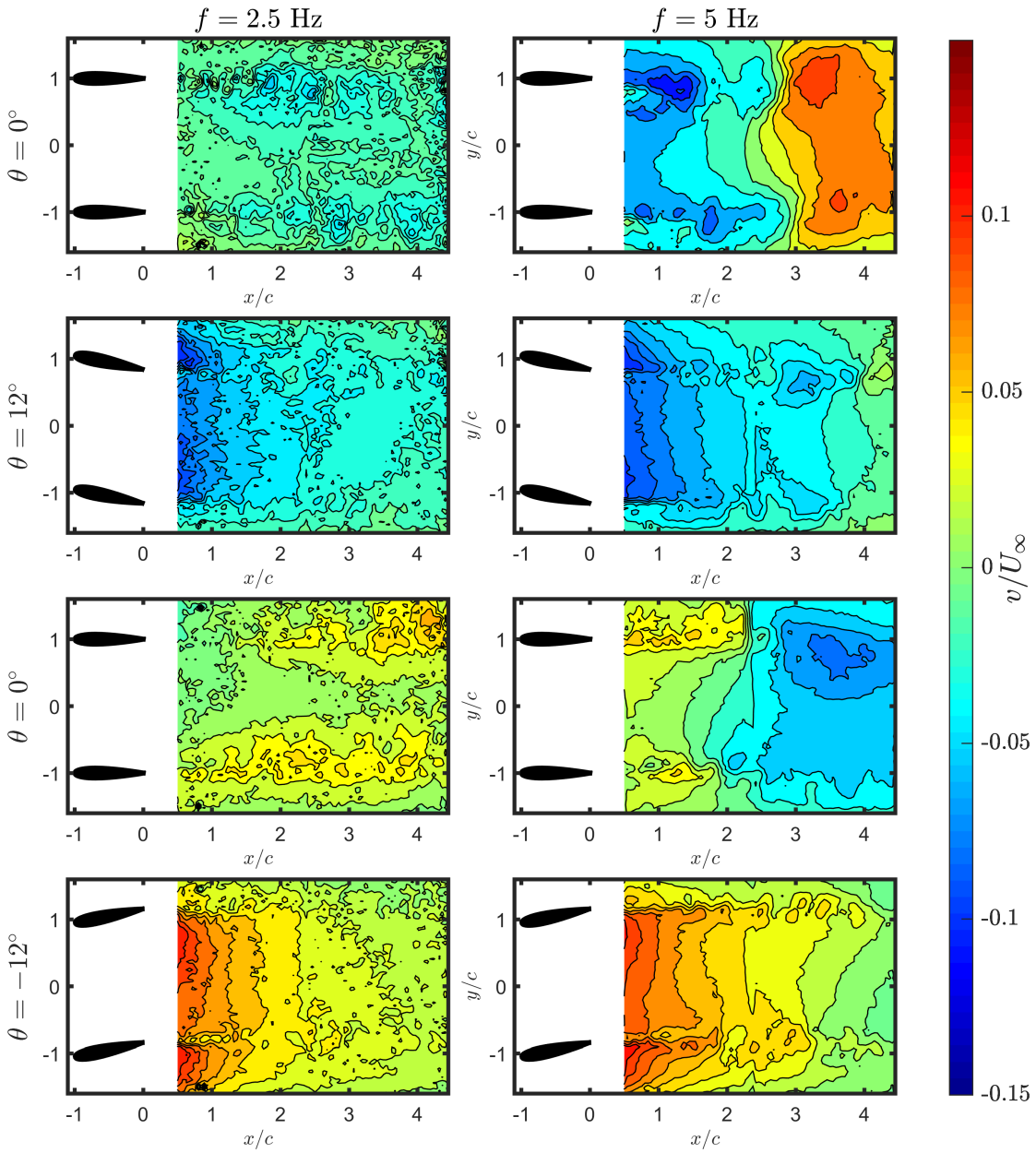


Figure 3.15: Effect of pitching frequency on the transverse component of velocity. Columns represent the test cases for which frequency is different and other parameters are identical. Rows represent the phase angle of the period. One period of motion starts from 0°, peaks at θ_{max}, becomes 0° again and goes to minimum (θ_{min}).

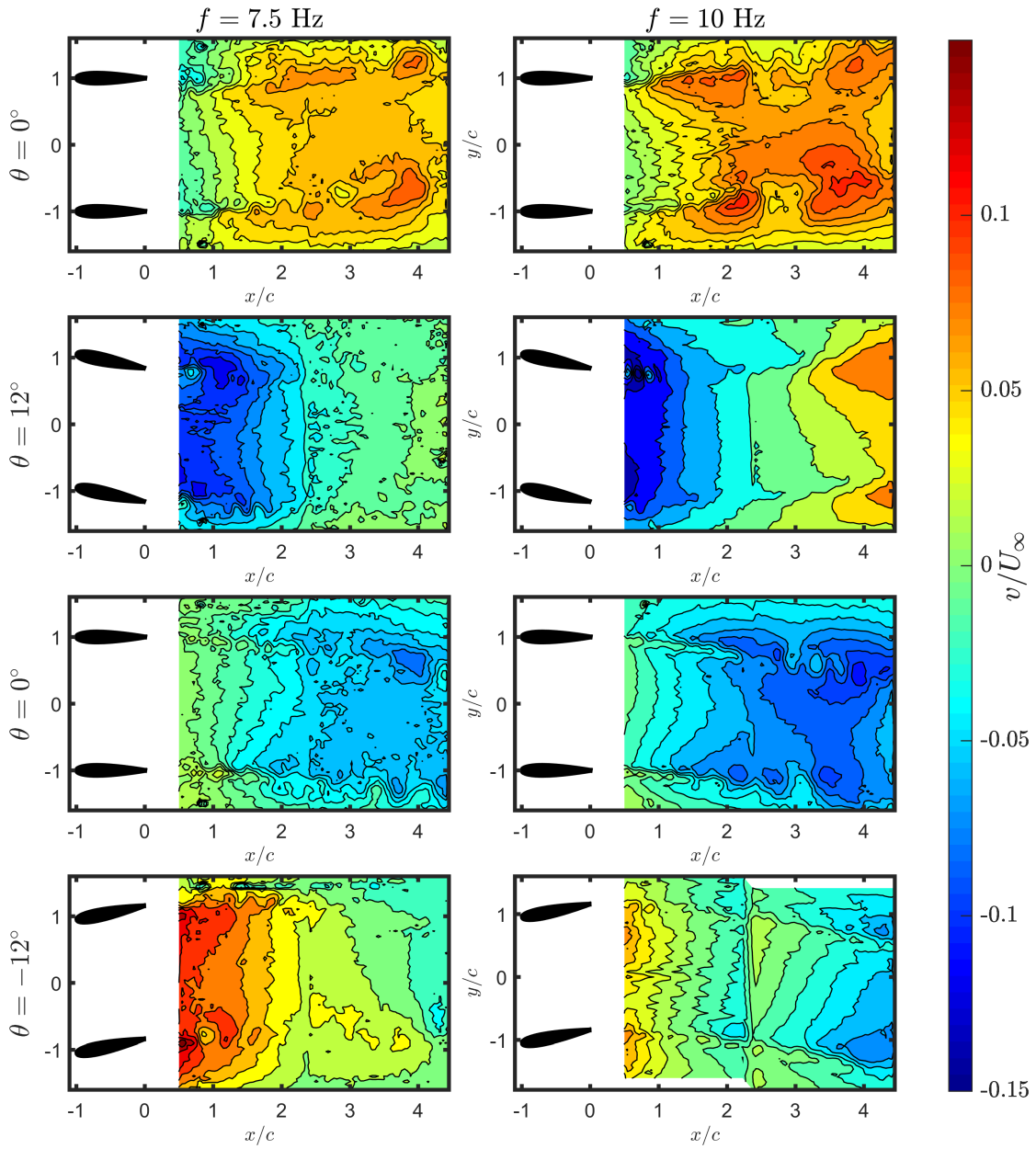


Figure 3.16: Effect of pitching frequency on the transverse component of velocity. Columns represent the test cases for which frequency is different and other parameters are identical. Rows represent the phase angle of the period. One period of motion starts from 0°, peaks at θ_{max}, becomes 0° again and goes to minimum (θ_{min}).

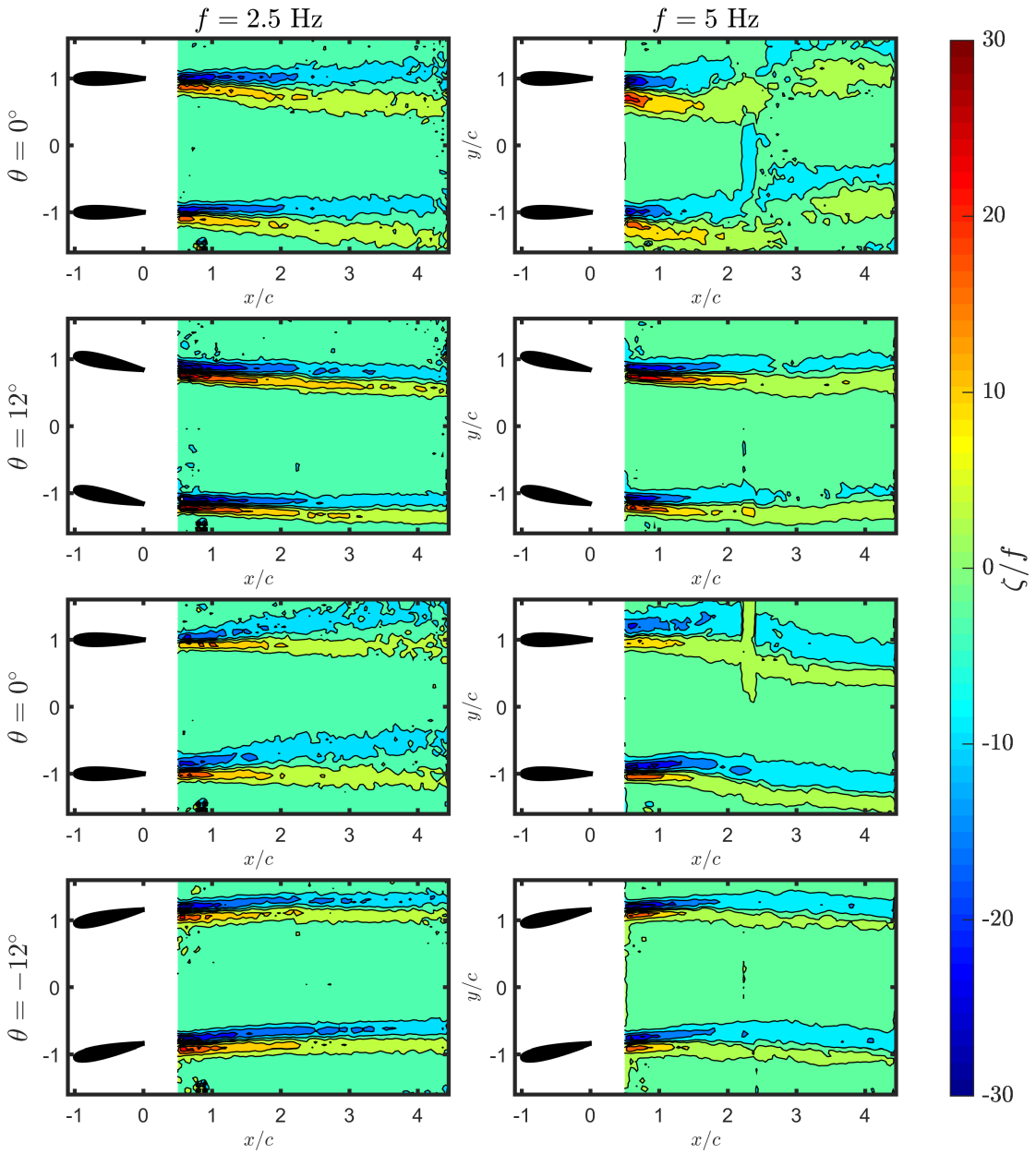


Figure 3.17: Effect of pitching frequency on vorticity. Columns represent the test cases for which frequency is different and other parameters are identical. Rows represent the phase angle of the period. One period of motion starts from 0°, peaks at θ_{max}, becomes 0° again and goes to minimum (θ_{min}).

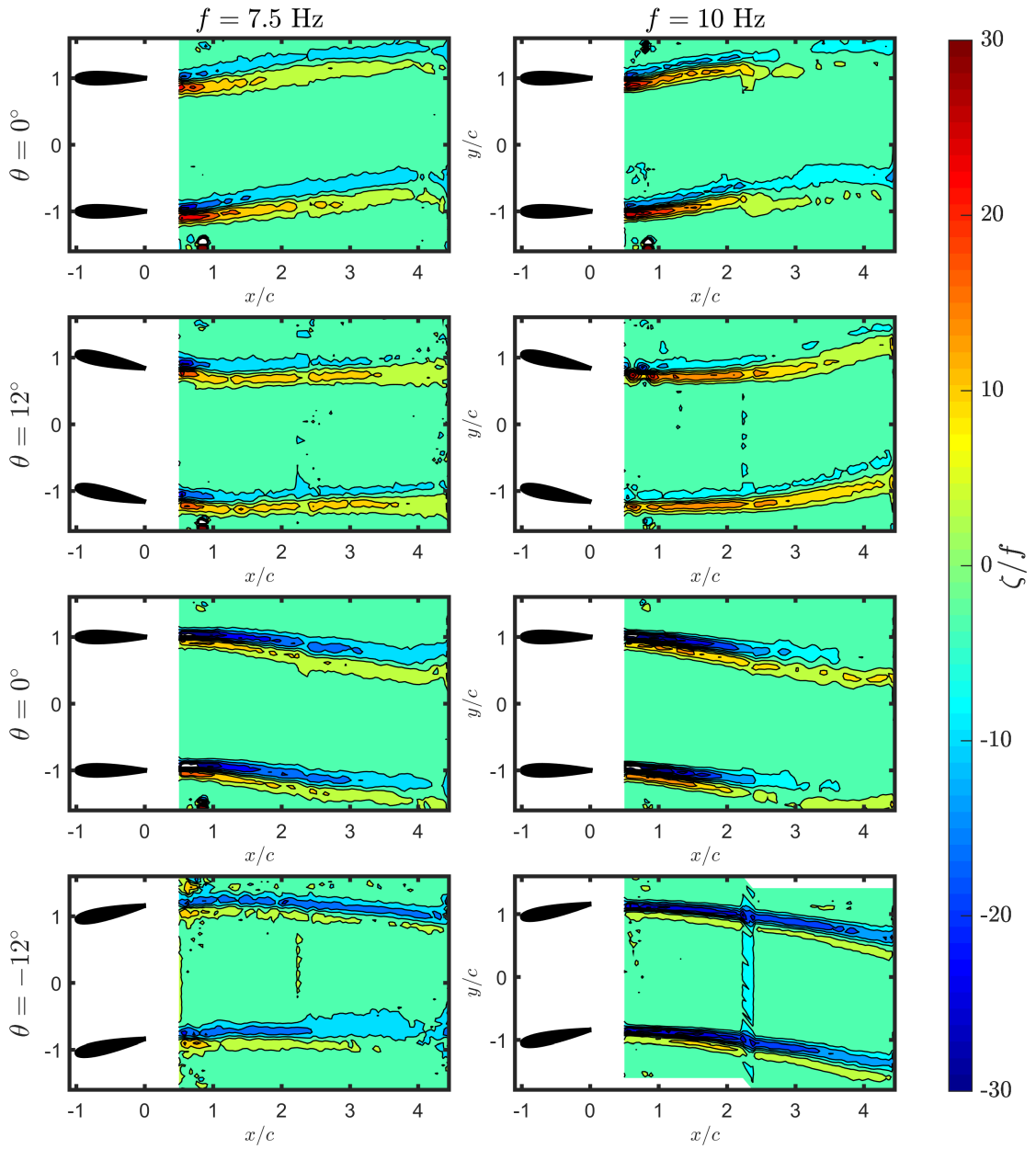


Figure 3.18: Effect of pitching frequency on vorticity. Columns represent the test cases for which frequency is different and other parameters are identical. Rows represent the phase angle of the period. One period of motion starts from 0°, peaks at θ_{max}, becomes 0° again and goes to minimum (θ_{min}).

3.3.1.2 Effect of the Freestream Velocity

A freestream velocity range of 5-15 m/s is selected to examine the effect of freestream velocity on the resulting flow field. The sole parameter that is varied is the freestream velocity and all of the other parameters are identical to baseline case ($f = 10$ Hz, $d = 2c$ and $\bar{\theta} = 12°$). A minimum of 5 m/s is selected to be able to obtain a steady, uniform velocity in the test section. A maximum of 15 m/s is selected such that a gust flow of sufficient amplitude is obtained and a safe operation of the wind tunnel is maintained.

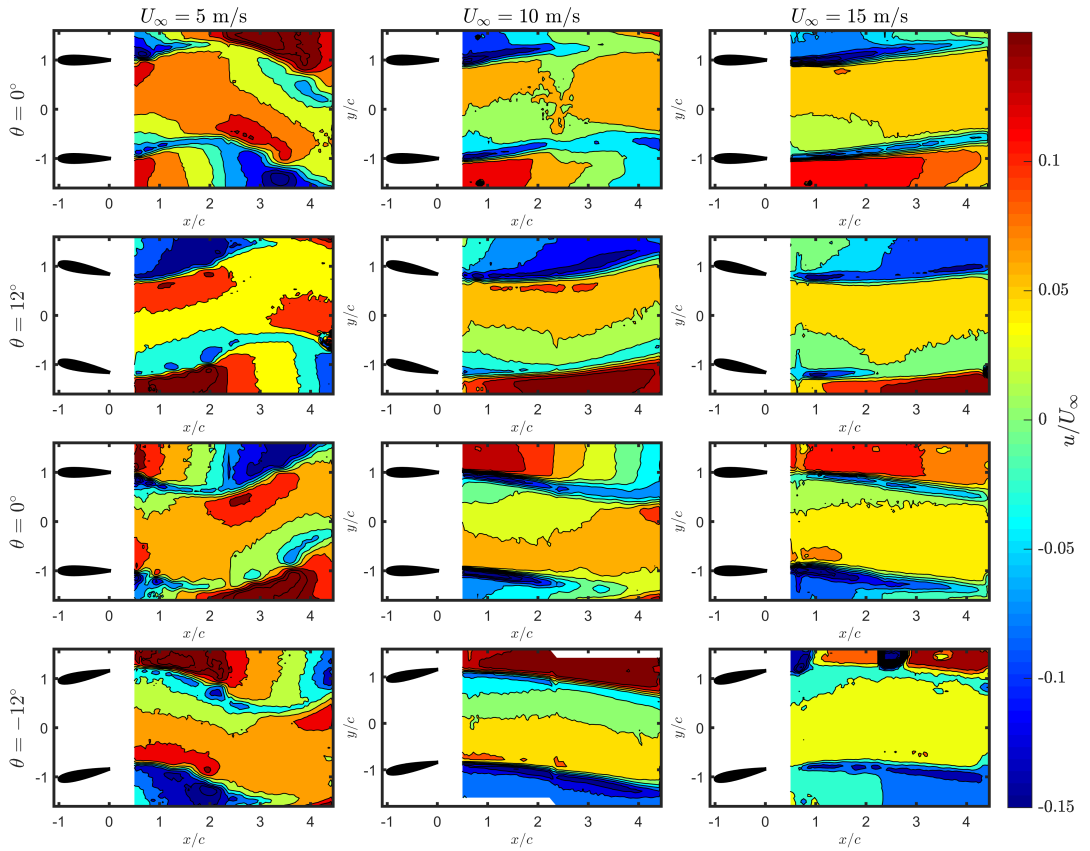


Figure 3.19: Effect of freestream velocity on the streamwise component of velocity. Columns represent the test cases for which frequency is different and other parameters are identical. Rows represent the phase angle of the period. One period of motion starts from 0°, peaks at θ_{max}, becomes 0° again and goes to minimum (θ_{min}).

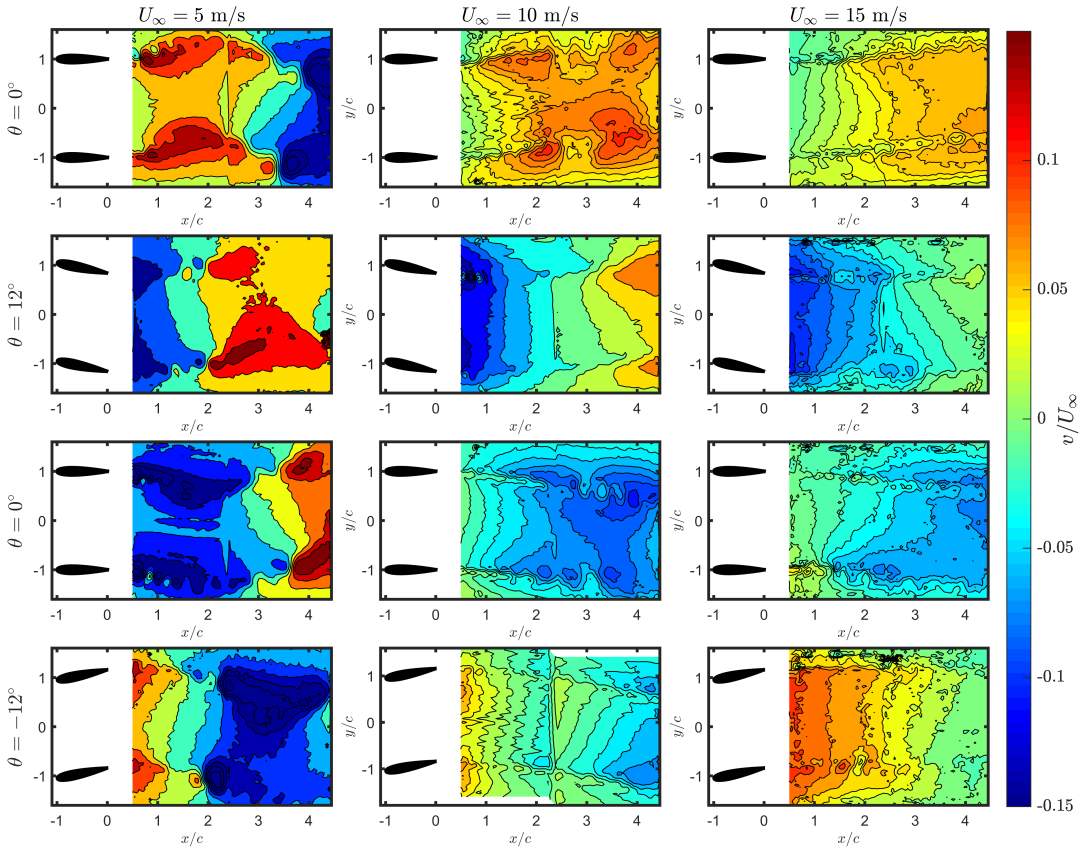


Figure 3.20: Effect of freestream velocity on the transverse component of velocity. Columns represent the test cases for which frequency is different and other parameters are identical. Rows represent the phase angle of the period. One period of motion starts from 0°, peaks at θ_{max}, becomes 0° again and goes to minimum (θ_{min}).

Streamwise velocity contours (Figure 3.19) reveal that with a decrease in the freestream velocity, i.e., an increase in the reduced frequency, the deflection in the wakes of the vanes increases. This results in a sharp variation in the area of the useful working section, thus, formation of patches of high speed regions between the vanes and the walls of the test section. Hence, model placement in y direction becomes critical as the freestream velocity decreases. Apart from that, the gust ratio at the center of the two vanes ($y/c = 0$) is not affected dramatically by the changes in the freestream velocity.

Transverse velocity component, on the other hand, in accordance with the previous results, shows a more uniform and symmetrical distribution. Coherent structures travel downstream without a significant variation in their structure. Yet, with a decrease in

the freestream velocity, thus an increase in the reduced frequency, coherent regions of non-zero transverse velocity are generated more quickly, suggesting an increase in the severity and magnitude of gust. The loss of uniformity with a decreasing freestream velocity, thus increasing reduced frequency, is clearly observed in this case as well. Transverse velocity contours of the case with the minimum reduced frequency ($U_\infty = 15$ m/s) demonstrate a uniform behavior in y direction, allowing a large space for a model to be placed. On the other hand, coherent flow structures that change sharply in y direction for the case when $U_\infty = 5$ m/s limits the locations for a model to be positioned.

For the case with the highest reduced frequency, i.e. ,lowest freestream velocity, out-of-plane vorticity contours depict a larger deflection in the wake vorticity layers and a decrease in the magnitude. Vortical structures emerging from the vanes are clearly observed for the case when $U_\infty = 5$ m/s.

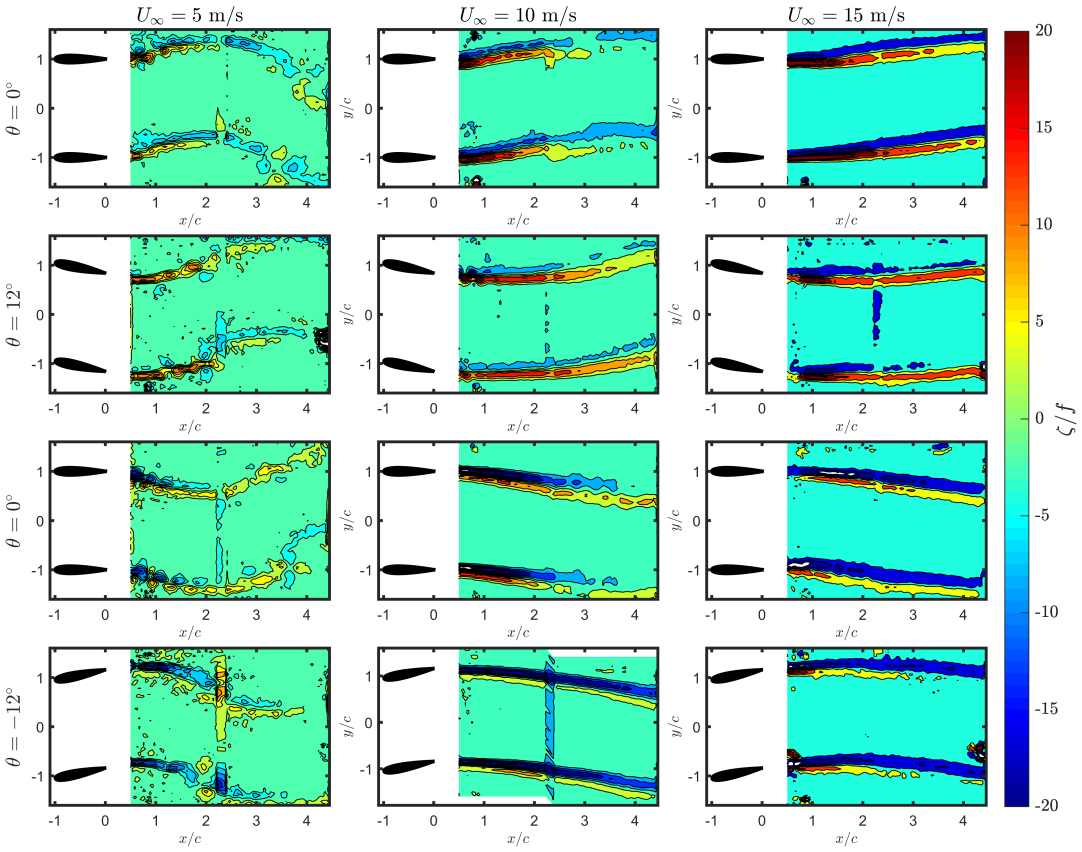


Figure 3.21: Effect of freestream velocity on vorticity. Columns represent the test cases for which frequency is different and other parameters are identical. Rows represent the phase angle of the period. One period of motion starts from 0°, peaks at θ_{max}, becomes 0° again and goes to minimum (θ_{min}).

3.3.2 Effect of the Vane Spacing

As mentioned in Chapter 2, a vane spacing range of $1.0c$ to $2.5c$ is selected. A maximum of $2.5c$ is selected based on both literature review and the size of the test section. A minimum of $1c$ is selected, which is also a limitation of the frame design. Yet, these values both lie in the range of vane spacing values of the gust generators of other institutions. Actuation parameters are identical to those of the baseline case, $f = 10$ Hz, $U_\infty = 10$ m/s and $\bar{\theta} = 12°$.

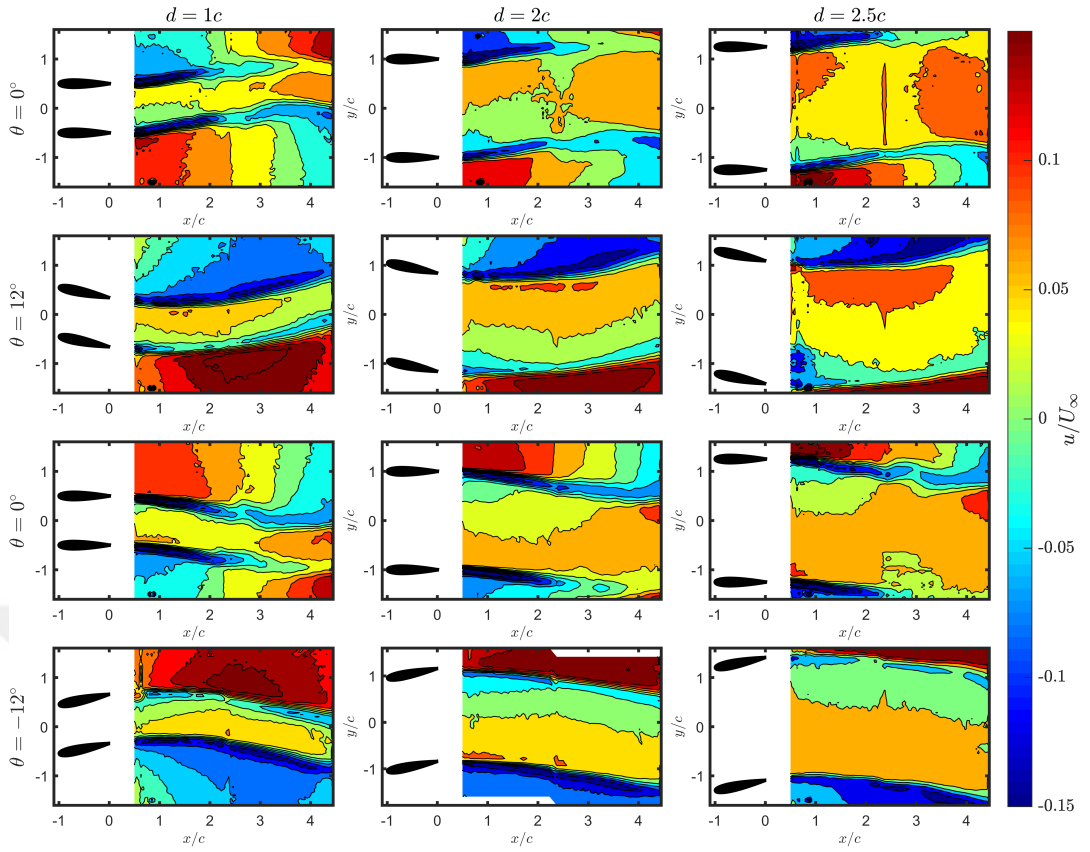


Figure 3.22: Effect of vane spacing on the streamwise component of velocity. Columns represent the test cases for which frequency is different and other parameters are identical. Rows represent the phase angle of the period. One period of motion starts from 0°, peaks at θ_{max}, becomes 0° again and goes to minimum (θ_{min}).

Figure 3.22 reveals that with an increase in the vane spacing, wakes of the two vanes are damped by the test section walls. Hence, patches of high velocity occupy a smaller area, as the vane spacing increases. This results in the area of the useful working section becoming larger. This may be advantageous in placing a model to test under gusty inflow conditions. Also, magnitude of velocity in the region between the two vanes is very minimally affected, which suggests that streamwise gust ratio does not change dramatically with vane spacing.

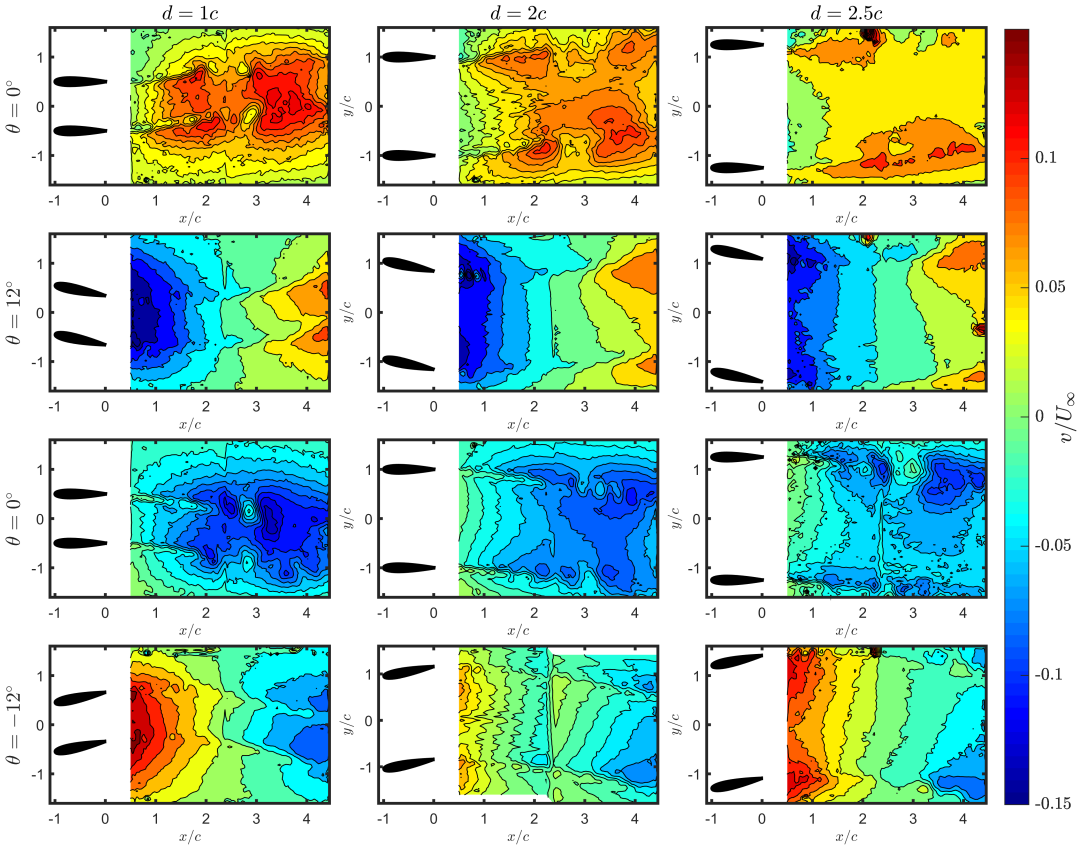


Figure 3.23: Effect of vane spacing on the transverse component of velocity. Columns represent the test cases for which frequency is different and other parameters are identical. Rows represent the phase angle of the period. One period of motion starts from 0°, peaks at θ_{max}, becomes 0° again and goes to minimum (θ_{min}).

Figure 3.23 depicts a quicker formation of regions of coherent non-zero transverse velocity with a decrease in vane spacing. Also, an increase in the magnitude of transverse velocity is clearly observed, suggesting an increase in the gust ratio with a decrease in the distance between the vanes.

Figure 3.24 reveals that useful working section which is under the influence of gust and is not affected by wake vorticity of the vanes and becomes limited in y direction with a decrease in the vane spacing. For the case when $d = 2.5c$, wake vorticity layers of the vanes are damped easily by the tunnel walls.

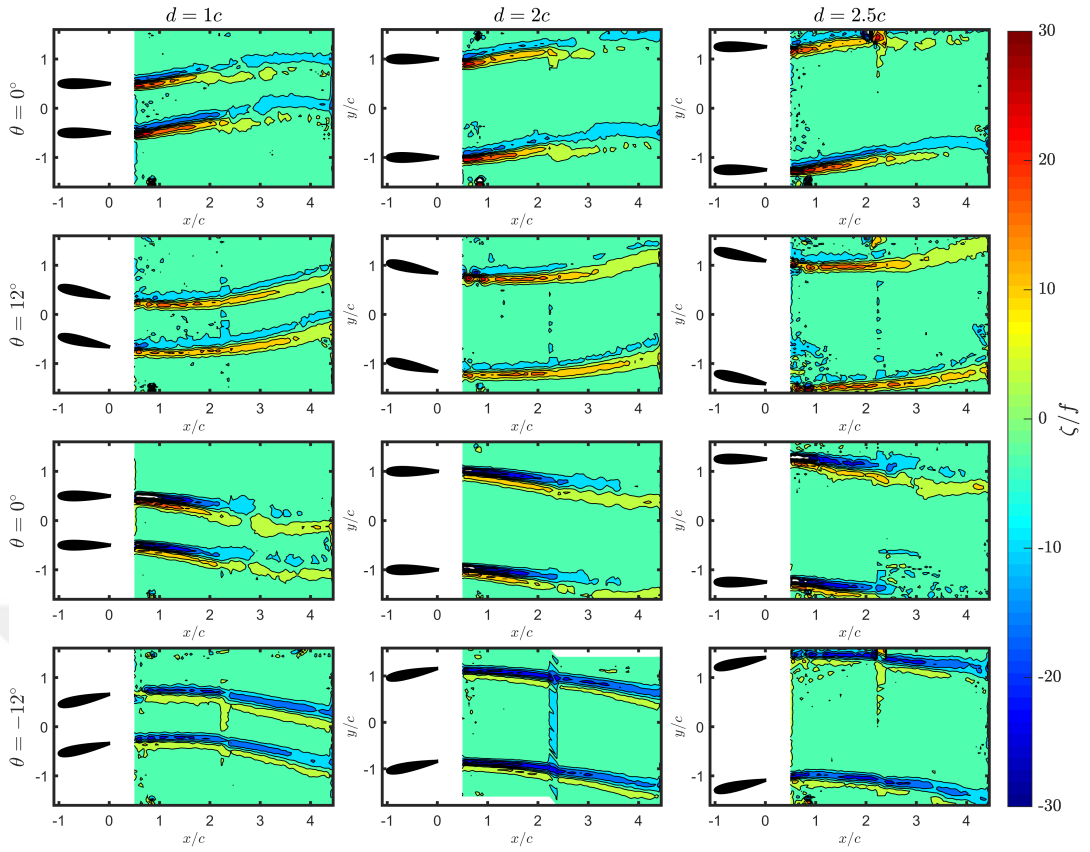


Figure 3.24: Effect of vane spacing on vorticity. Columns represent the test cases for which frequency is different and other parameters are identical. Rows represent the phase angle of the period. One period of motion starts from 0°, peaks at θ_{max}, becomes 0° again and goes to minimum (θ_{min}).

3.3.3 Effect of the Pitching Amplitude

As mentioned in Chapter 2, a maximum pitching amplitude range of 8°-16° is selected. Maximum value is limited to avoid stalling, and minimum value is selected such that a gust of sufficient amplitude shall be observed. Other actuation parameters are identical to those of the baseline case, $f = 10$ Hz, $U_\infty = 10$ m/s and $d = 2c$.

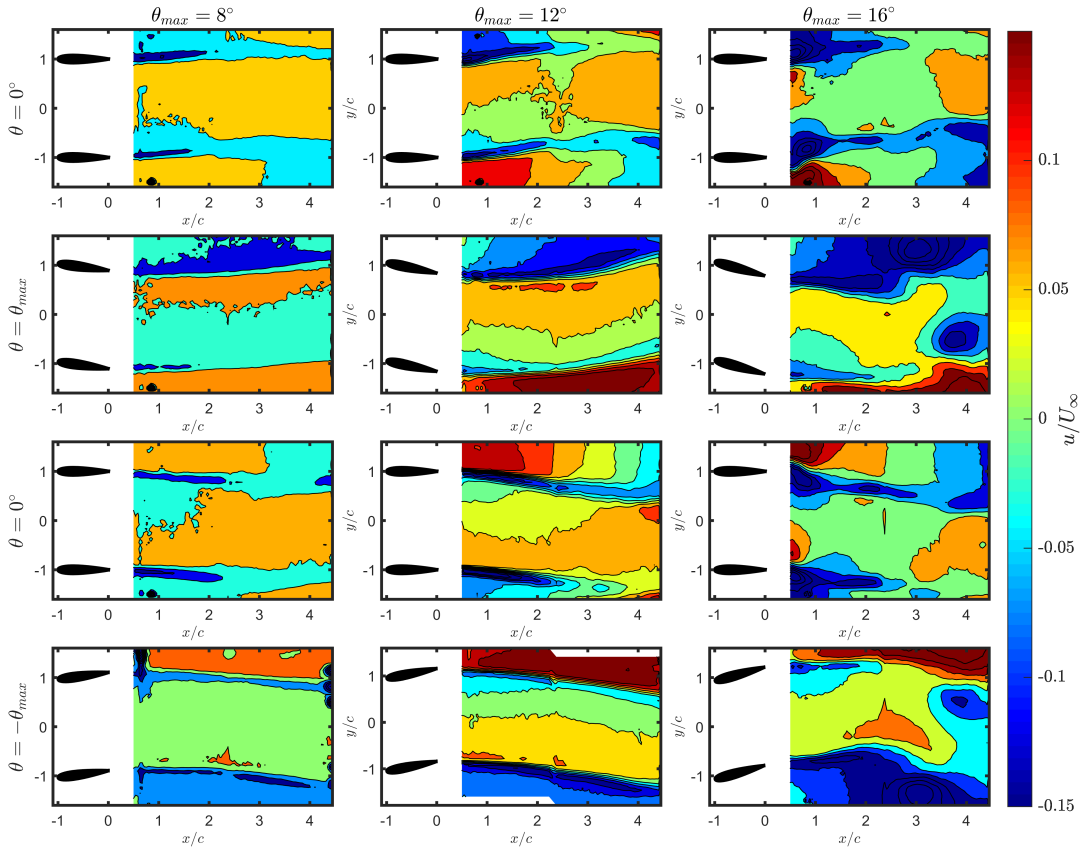


Figure 3.25: Effect of maximum amplitude on the streamwise component of velocity. Columns represent the test cases for which frequency is different and other parameters are identical. Rows represent the phase angle of the period. One period of motion starts from 0°, peaks at θ_{max}, becomes 0° again and goes to minimum (θ_{min}).

As Figures 3.25, 3.26 and 3.27 reveal, increasing the pitching amplitude to 16° leads to the stall of the gust vanes. As a result of the flow separation, more coherent vortical patterns emerge in the wake of the vanes. Yet, a disruption in the symmetry and homogenity of the gust flow is encountered, especially in the transverse velocity component. This may be attributed to the flow separation and associated wake vorticity region. Moreover, as a result of the flow separation, a significant loss in the gust uniformity is also encountered.

Conseqeuently, due to the loss of symmetry and homogenity of the gust, the case with maximum motion amplitude is not convenient for studying the gust response of an aerodynamic model in the test section.

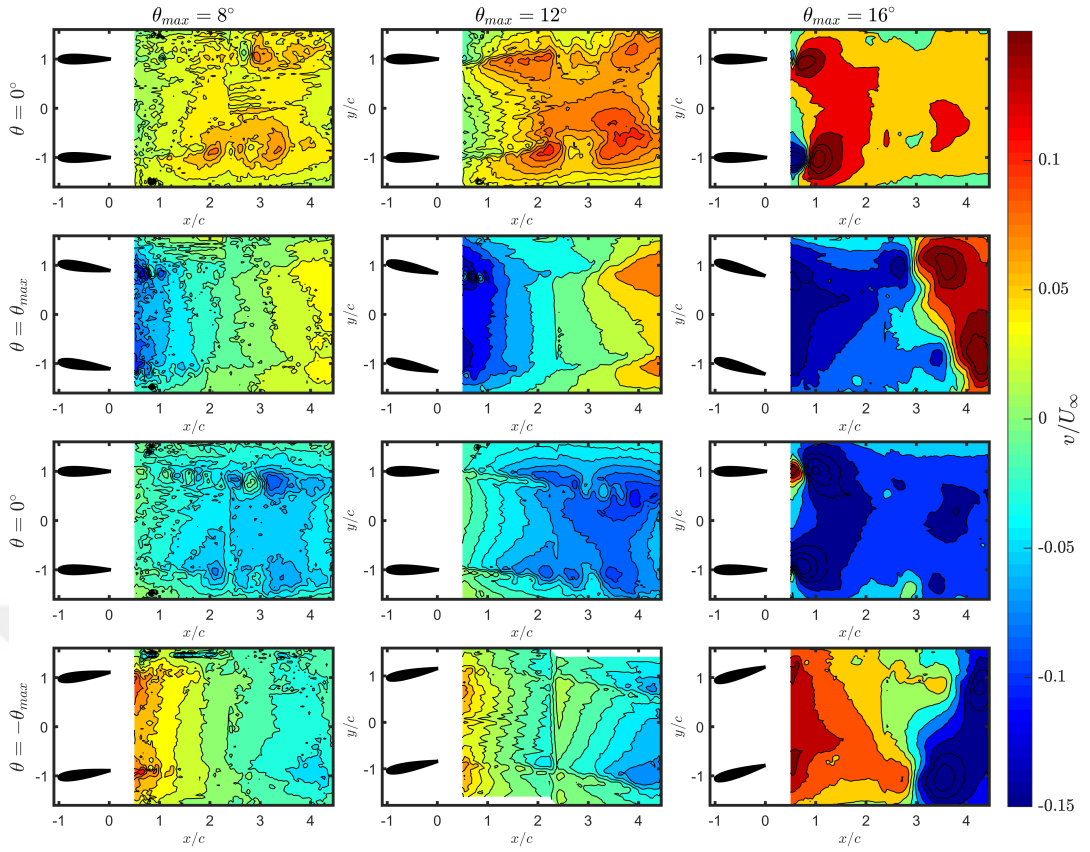


Figure 3.26: Effect of maximum amplitude on the transverse component of velocity. Columns represent the test cases for which frequency is different and other parameters are identical. Rows represent the phase angle of the period. One period of motion starts from 0°, peaks at θ_{max}, becomes 0° again and goes to minimum (θ_{min}).

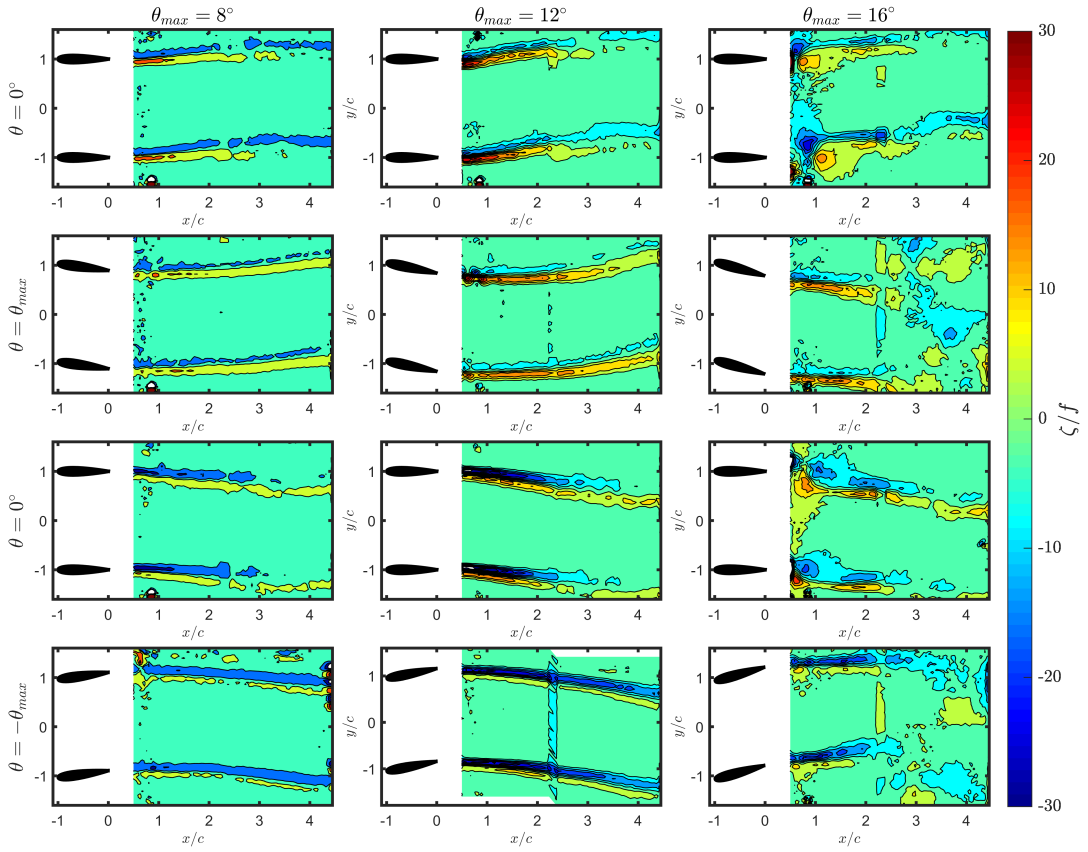


Figure 3.27: Effect of maximum amplitude on vorticity. Columns represent the test cases for which frequency is different and other parameters are identical. Rows represent the phase angle of the period. One period of motion starts from 0°, peaks at θ_{max}, becomes 0° again and goes to minimum (θ_{min}).

3.4 Temporal Variations in the Flow Field

In addition to spatial variations in the flow field, temporal behavior is also examined at fixed downstream locations through each phase of the period in terms of gust ratio. To explore the effects of varying actuation parameters and vane spacing, temporal results at $x/c = 3$ and $y/c = 0$ location are presented.

For the baseline case, streamwise and transverse gust ratios at the mid-point between the two vanes are calculated for each phase of the period at two downstream locations. Streamwise gust ratio is very small in magnitude and shows a sinusoidal behavior at both locations. This is attributed to the motion kinematics of the two vanes. The

motion being in-phase results in a dominant transverse gust ratio and as a consequence of changing blockage ratio through the course of pitching motion, a small streamwise gust is also generated.

Transverse gust ratio slightly increases downstream, and displays a clear sinusoidal trend. The lag between two downstream locations is clearly observed, which stems from the advection of coherent non-zero transverse velocity regions demonstrated on the contour plots.

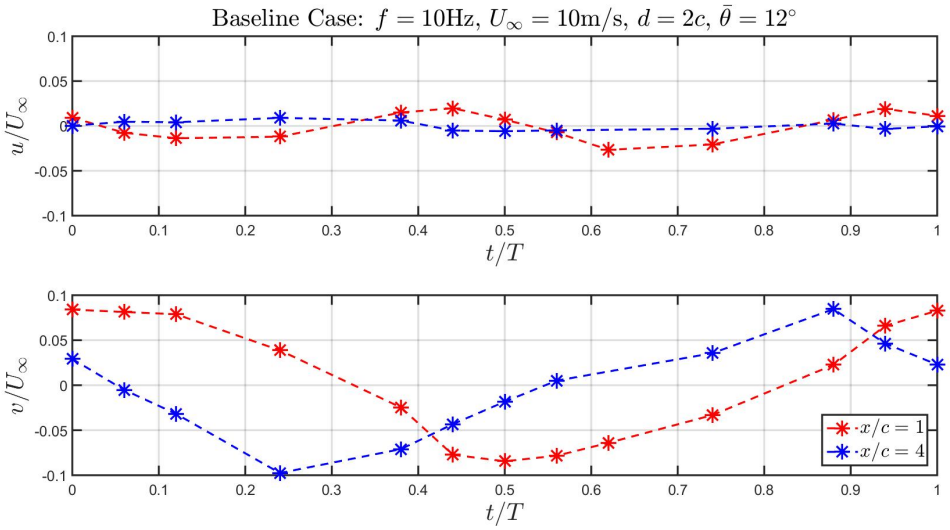


Figure 3.28: Streamwise and transverse gust ratio values at each phase of the period for the baseline case.

3.4.1 Effect of Reduced Frequency

Effect of reduced frequency is examined through varying two parameters independently, pitching frequency and freestream velocity. Gust ratio at each phase of the period where PIV measurements are taken, is calculated at $x/c = 3$ location.

The two cases with the same reduced frequency ($k = 0.2513$), but different actuation parameters result in very close gust ratios and temporal behavior, as expected.

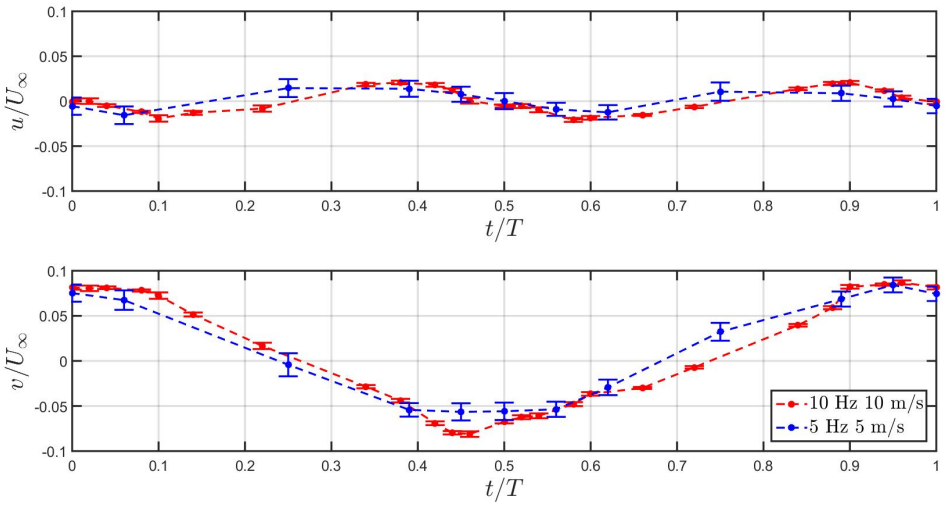


Figure 3.29: Streamwise and transverse gust ratio values at each phase of the period for the two cases with the same reduced frequency, but different actuation parameters.

3.4.1.1 Effect of the Pitching Frequency

A pitching frequency range of 2.5-10 Hz is selected and both streamwise and transverse gust ratio values at $x/c = 3$ are calculated.

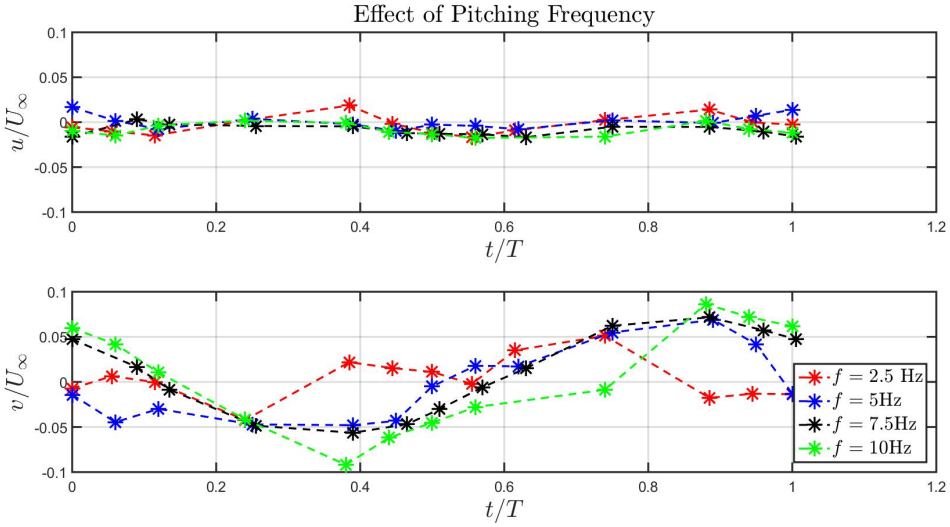


Figure 3.30: Streamwise and transverse gust ratio values at each phase of the period. Each line represents a case where pitching frequency is altered and other actuation parameters are identical. ($U_\infty = 10$ m/s, $d = 2c$ and $\bar{\theta} = 12°$.)

The case for which pitching frequency equals to 2.5 Hz fails to deliver a transverse gust profile that is approximately a sinusoid. This failure in delivering a transverse gust of sinusoidal profile for the case when $f = 2.5$ Hz, which corresponds to the case with the lowest reduced frequency, is also observed in CFD results.

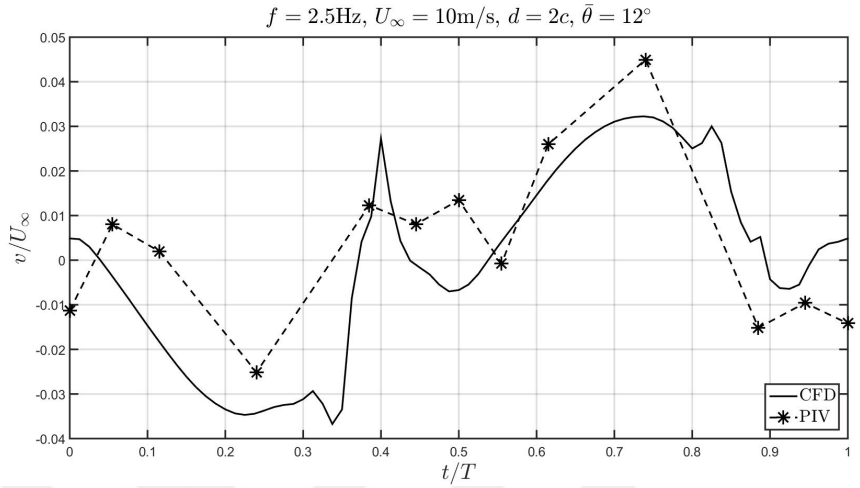


Figure 3.31: Transverse gust ratio values at each phase of the period. Dashed lines with symbols correspond to experimental data, while solid line corresponds to CFD results. ($f = 2.5$ Hz, $U_\infty = 10$ m/s, $d = 2c$ and $\bar{\theta} = 12°$.)

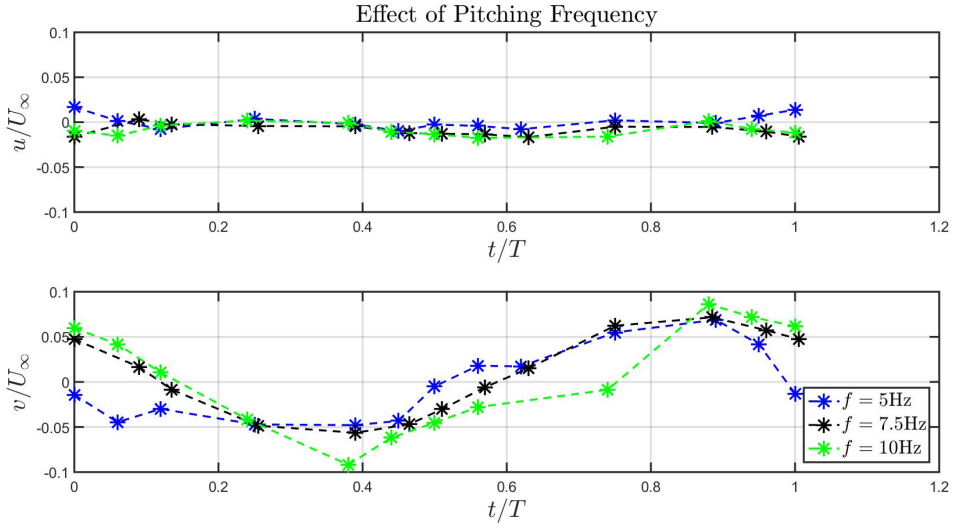


Figure 3.32: Streamwise and transverse gust ratio values at each phase of the period. Each line represents a case where pitching frequency is altered and other actuation parameters are identical. ($U_\infty = 10$ m/s, $d = 2c$ and $\bar{\theta} = 12°$.)

Thus, for this reduced frequency, which is the minimum reduced frequency among all test cases, a sinusoidal transverse gust cannot be generated. Hence, the effect of pitching frequency on the gust ratio can be observed more clearly with the elimination of that specific case.

Figure 3.32 reveals that streamwise gust is very small in magnitude and is almost not affected by the changes in pitching frequency. Transerverse gust on the other hand, increases in magnitude with an increase in pitching frequency. This is very well expected, as an increase in pitching frequency results in an increase in the reduced frequency, thus, an enhanced unsteadiness is introduced into the flow.

Another significant observation depicted in Figure 3.32 is that, with an increase in the pitching frequency, thus reduced frequency, a phase lag emerges between the cases. This is shown more clearly in the results obtained via CFD runs, as shown in Figure 3.33. In accordance with the contour plots, advection velocity of the coherent fluid regions of non-zero transverse velocity changes with changing reduced frequency and results in a phase lag. This phase lag is more pronounced in the temporal analysis plots.

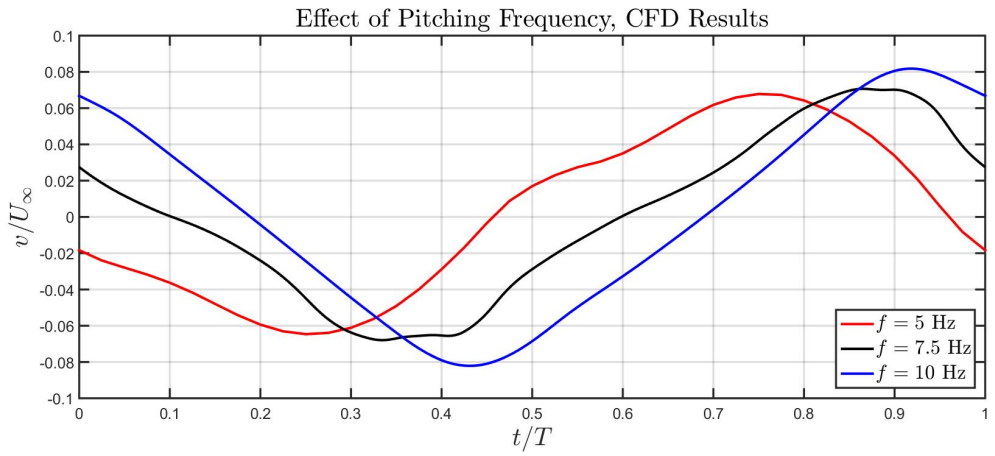


Figure 3.33: Transverse gust ratio values at each phase of the period obtained via CFD runs. Each line represents a case where pitching frequency is altered and other actuation parameters are identical. ($U_\infty = 10$ m/s, $d = 2c$ and $\bar{\theta} = 12°$.)

The phase lag that is observed between the cases with different pitching frequency values, i.e., reduced frequency values, is related to unsteady thin airfoil theory. It

provides a systematic approach for the calculation of unsteady aerodynamic forces. For an airfoil that is undergoing a sinusoidal pitching motion, lift force equals to [50]:

$$L = [C(k) - 1]L_0 \tag{3.7}$$

where $C(k)$ is the Theodorsen function and L_0 is the steady lift that can be calculated by the steady potential theory. Theodorsen's function is a complex number and it depends on the reduced frequency (k):

$$C(k) = F(k) + \mathrm{i}G(k) \tag{3.8}$$

The imaginary term is responsible for the phase lag between the motion and the aerodynamic response [9].

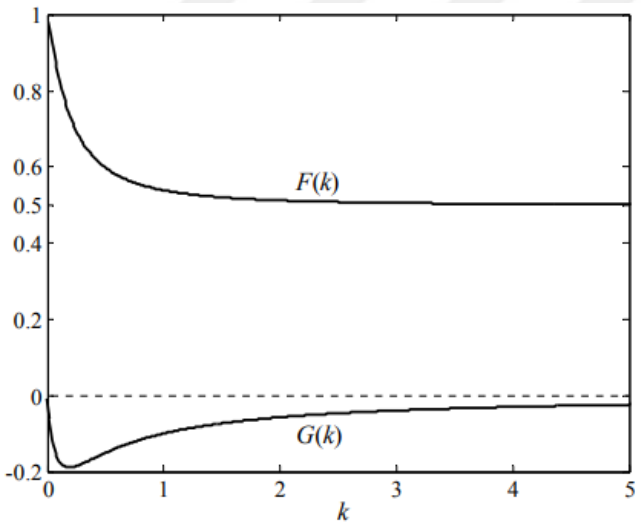


Figure 3.34: Imaginary and real parts of the Theodorsen function [50].

As demonstrated in Figure 3.34, with an increase in the reduced frequency, imaginary part of the Theodorsen function increases after a minimum point. Thus, with an increase in the pitching frequency, i.e., the reduced frequency, the peak location of the gust velocity in a period of motion is delayed and a phase lag is observed.

3.4.1.2 Effect of the Freestream Velocity

A freestream velocity range of 5-15 m/s is selected and both streamwise and transverse gust ratio values at $x/c = 3$ are calculated.

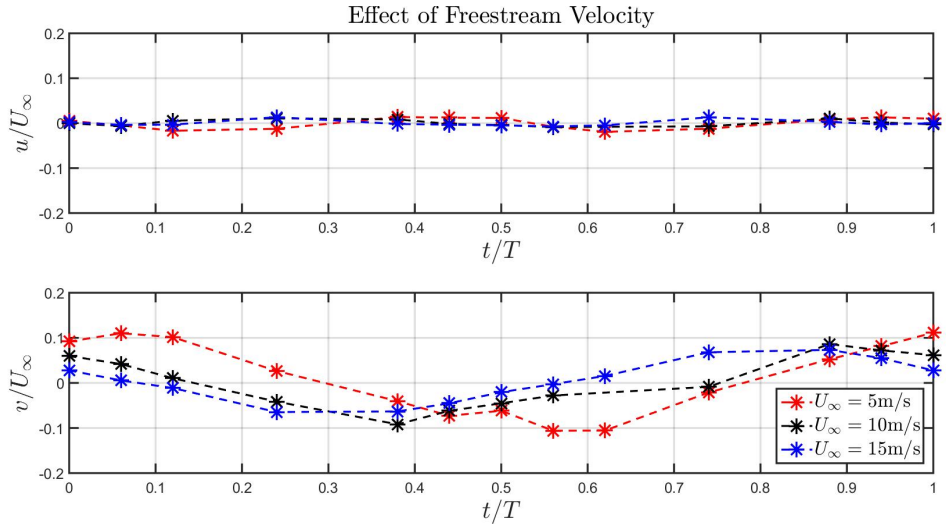


Figure 3.35: Streamwise and transverse gust ratio values at each phase of the period. Each line represents a case where freestream velocity is altered and other actuation parameters are identical. ($f = 10$ Hz, $d = 2c$ and $\bar{\theta} = 12°$.)

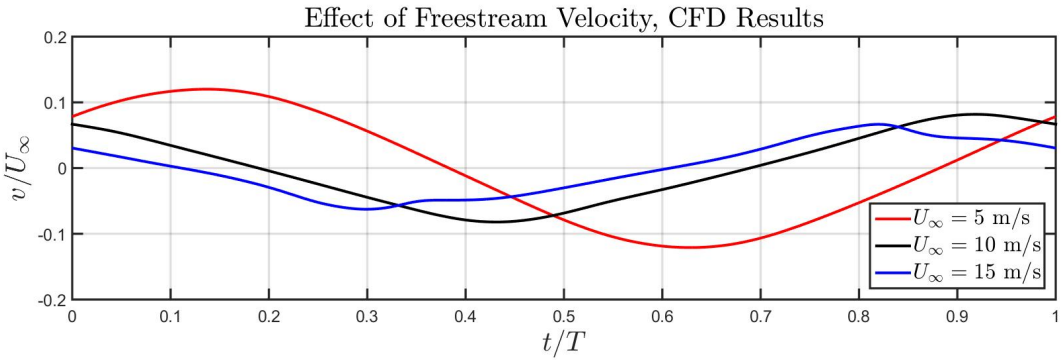


Figure 3.36: Transverse gust ratio values at each phase of the period obtained via CFD runs. Each line represents a case where freestream velocity is altered and other actuation parameters are identical. ($f = 10$ Hz, $d = 2c$ and $\bar{\theta} = 12°$.)

Figure 3.35 demonstrates that similar to the previous case, streamwise gust ratio is very small and almost not affected by the changes in the freestream velocity. Transverse gust ratio, on the other hand, increases with decreasing freestream velocity. Phase lag between the cases is observed clearly as well.

Phase lag and decrease in transverse gust ratio with increasing freestream velocity can be observed clearly in CFD results as well (Figure 3.36). This is related to the imagi-

nary part of the Theodorsen function decreasing with increasing freestream velocity, which corresponds to a decreasing reduced frequency. Hence, with a decrease in the freestream velocity, the peak of the gust velocity in a period of motion is delayed.

3.4.2 Effect of the Vane Spacing

A vane spacing range of 1.0-2.5c is selected and both streamwise and transverse gust ratio values at $x/c = 3$ are calculated. Similar to the other cases, streamwise gust ratio is very small and almost not affected by the changes in vane spacing. Although generation of patches of high velocity is affected as shown in the contour plots, streamwise gust ratio at the center of the vanes does not change with the vane spacing.

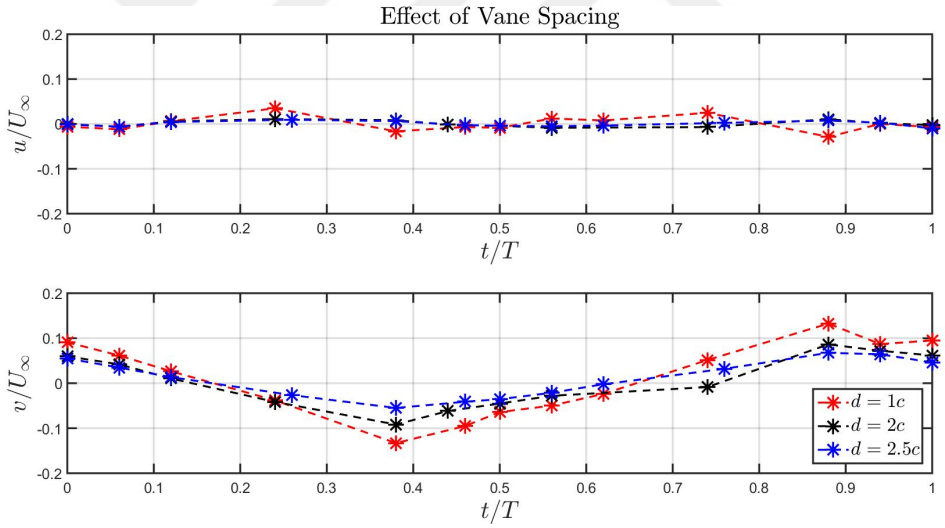


Figure 3.37: Streamwise and transverse gust ratio values at each phase of the period. Each line represents a case where vane spacing is altered and other actuation parameters are identical. ($U_\infty = 10$ m/s, $f = 10$ Hz and $\bar{\theta} = 12°$.)

Transverse gust ratio increases with a decrease in the vane spacing, yet, no phase lag exists between the cases. This indicates that phase lag is only generated as a result of changing reduced frequency, i.e., unsteadiness of the flow field.

3.4.3 Effect of the Maximum Pitching Amplitude

A maximum pitching amplitude range of 8°-16° is selected and both streamwise and transverse gust ratio values at $x/c = 3$ are calculated.

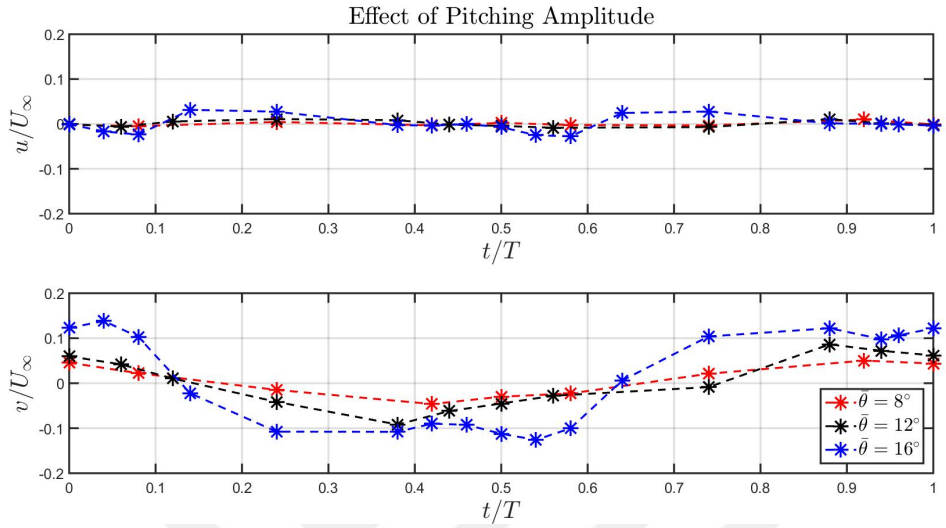


Figure 3.38: Streamwise and transverse gust ratio values at each phase of the period. Each line represents a case where maximum pitching amplitude is altered and other actuation parameters are identical. ($U_\infty = 10$ m/s, $f = 10$ Hz and $d = 2c$.)

Figure 3.38 shows no sensitivity of streamwise gust ratio to the pitching amplitude. However, the transverse gust ratio increases with an increase in the pitching amplitude. Also, for the case when $\bar{\theta} = 16°$, as a result of the flow separation demonstrated in contour plots, sinusoidal behavior of the gust is lost.

3.5 An Application Regarding Wind Turbines: Porous Disk Approach

In this section, wake flows of a porous disk and a model turbine are compared under a transverse gust loading, with the purpose of exploring the capability of the porous disk in representing the wake of a model wind turbine under gust loading.

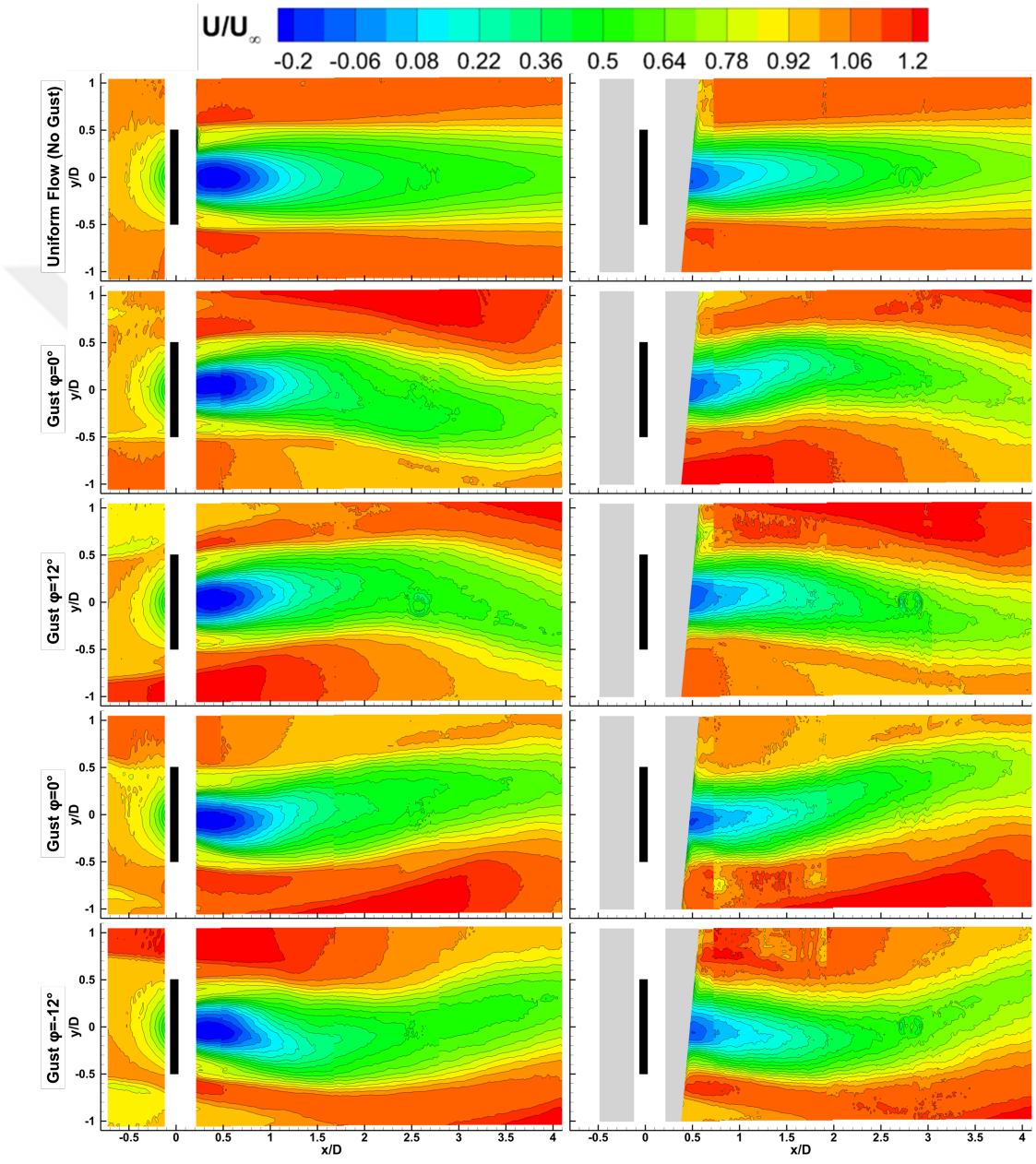


Figure 3.39: Left column: Porous disk under uniform flow, porous disk under gusty inflow. Right column: Model turbine under uniform flow, model turbine under gusty inflow. Gust vanes are at 0°, 12°, 0° and -12° angle of attack, respectively.

In order to match the thrust coefficient of the model wind turbine with that of the porous disk, (i.e., $C_T = 0.8261$ at a Reynolds number of 78000), load measurements are performed for several rotation speeds of the model turbine. It is found that the turbine at 3350 rpm produce a thrust coefficient of 0.8227, which is close enough for further analyses.

Figure 3.39 demonstrate the contours of the streamwise velocity normalized by the freestream velocity for the porous disk and the model turbine under uniform and gusty inflow conditions. The region affected by the laser reflections are masked for both cases with white rectangles. The grey shaded area corresponds to the region that is affected by the shadows and reflections due to the model turbine. Black rectangles represent the porous disk and the model turbine.

The first row of Figure 3.39 demonstrate the streamwise velocity contours under a uniform inflow. It is observed that the wakde width of the porous disk is larger than that of the model turbine. Despite the symmetric nature of the wake flow for the porous disk, slightly lifted-up wake profile is observed for the turbine wake, which can better be inferred from the extracted velocity profiles shown in Figure 3.40.

The rows from 2 to 5 show the contour plots of the porous disk (left) and the model turbine (right) under gusty inflow taken at various vane angles. Skewness of the wake created as a result of the gusty inflow conditions and the alternating wakes of the vanes can clearly be observed in all of the contour plots. Similar streamwise wake velocity contours are observed in both cases. The wavelength of the wake is also similar for both models and no phase difference is observed between the wakes of the porous disk and the model turbine.

Figure 3.40 demonstrates the normalized streamwise velocity profiles for uniform inflow and gusty inflow conditions extracted at the positions ranging from $x/D = 1$ to $x/D = 4$ for both the porous disk and the model turbine. Results obtained for the porous disk are represented by solid lines while those obtained for the model turbine are represented by dashed lines. Although the initial wake widths and deficits for both uniform inflow and gusty inflow conditions are similar for both models (see velocity profiles at $x/D = 1$), the wake grows faster in the case of the model turbine which results in smaller deficit at $x/D = 4$ compared to the wake of the porous disk.

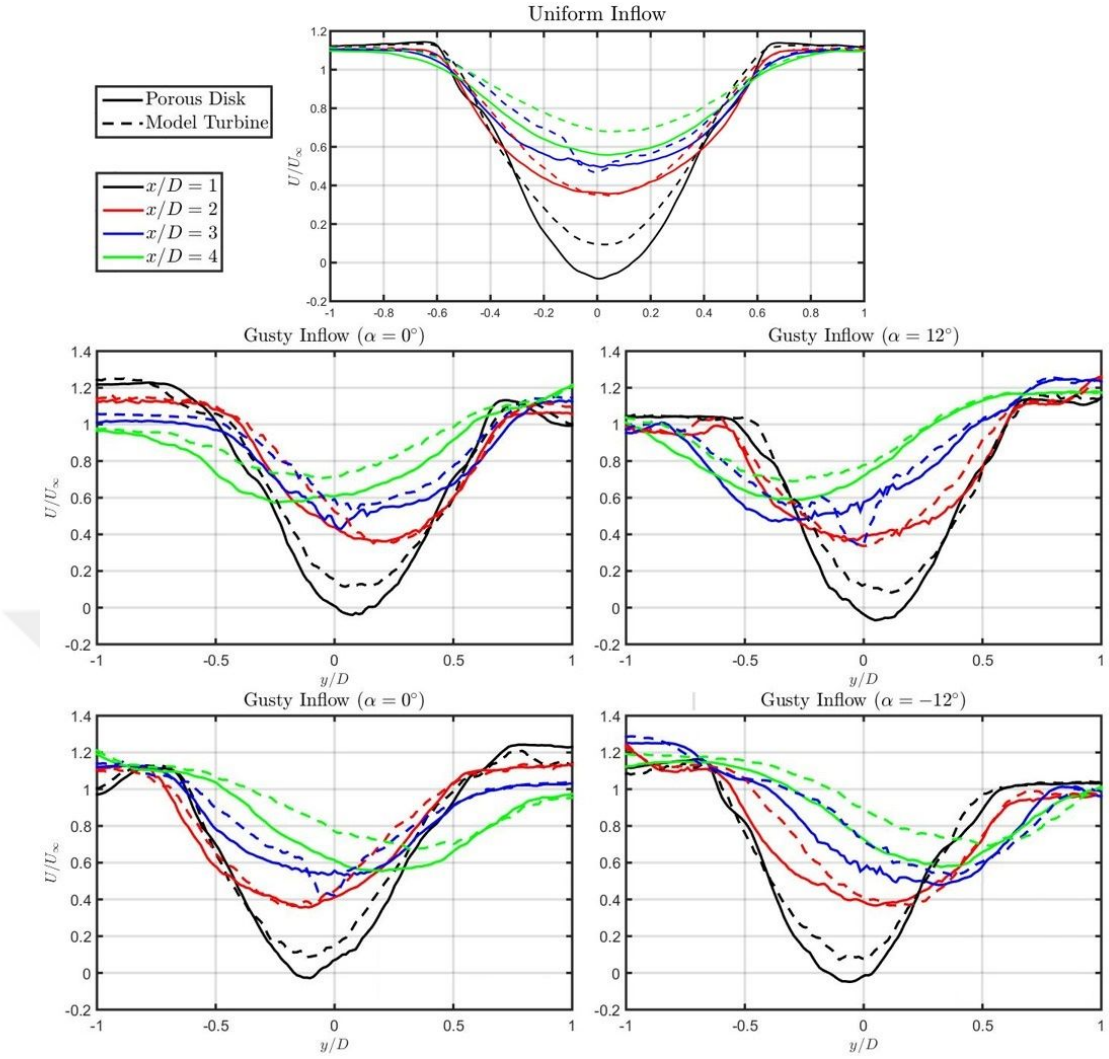


Figure 3.40: Wake deficit comparisons in terms of non-dimensional velocity at different x/D locations ($x/D = 1, 2, 3, 4$) under uniform and gusty inflow conditions at different phase angles for both porous disk (PD) and model turbine (MT).

In general, there is a better agreement between the wake velocity profiles of the porous disk and model turbine under gusty inflow conditions in the near wake (particularly in the first $3D$ downstream distance). Root mean square (RMS) normalized by the freestream velocity of the difference between the wake velocity distributions of the porous disk and the model turbine at different downstream locations for all the phases of gusty inflow condition are calculated to compare the extracted velocity profiles.

RMS values normalized by the freestream velocity reveal that the good agreement of the two models in the near wake deteriorates at more downstream stations. This

Table 3.1: RMS normalized by the freestream velocity of the difference of wake velocity distributions of the porous disk and the model turbine

Test Cases	**x/D**	**RMS/U_∞**
$\alpha > 0°$	1	0.0485
	4	0.0453
$\alpha = 12°$	1	0.0498
	4	0.0722
$\alpha < 0°$	1	0.0478
	4	0.0812
$\alpha = -12°$	1	0.0405
	4	0.0873

suggests caution in using porous disks to simulate wake flows of model wind turbine under gusty inflow conditions.

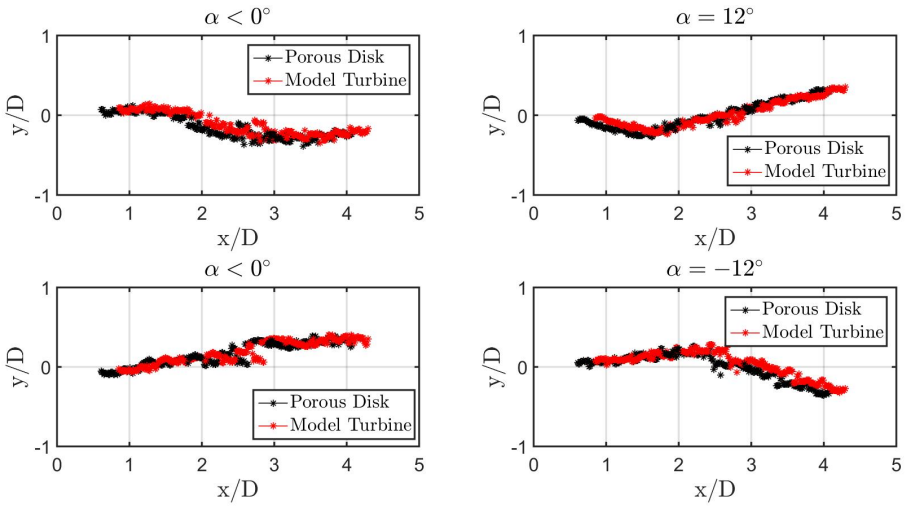


Figure 3.41: Wake centerline dynamics of the porous disk and the model turbine subjected to gusty inflow. α represents the phases of the sinusoidal motion of the vanes.

Comparison of the wake centerlines shown in Figure 3.41 suggests similar wave character in terms of phase and half wavelength for both wakes. It implies that the wave characteristics of the wake is mostly determined by the gust dynamics rather than the

experimental model.

3.5.1 Comparison of the Uniform Inflow Case and Average of the Phases

It is a common practice to use a phase averaging approach to investigate turbomachinery flows where high gradients in both space and time are present [52]. Wind turbines result in similar flow fields that are highly unsteady and are affected by high levels of turbulence due to the rotary motion of the blades. Consequently, wake flows of the porous disk and the model turbine under a uniform inflow condition are compared to the average of the phases of the gust vane motion.

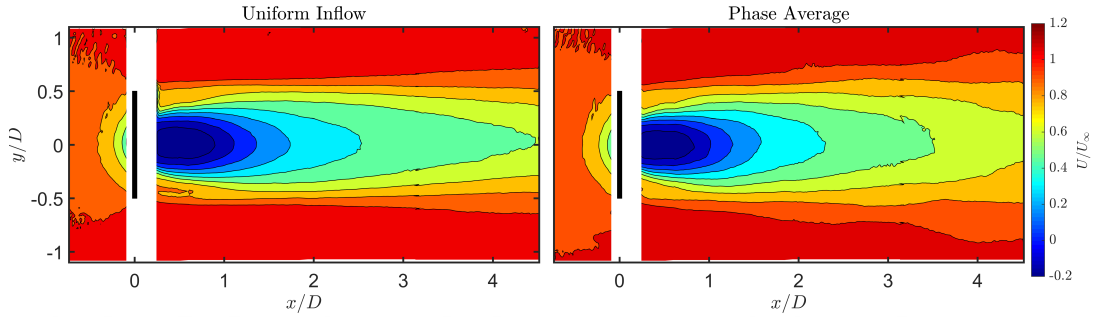


Figure 3.42: Non-dimensional streamwise velocity contours of the porous disk under uniform inflow (left) and the average of the phases of the motion of the gust vanes (right).

Contours shown in Figure 3.42 demonstrate a difference in the wake width, which becomes more pronounced in the far wake region. Wake decay for the phase average case is also quicker when compared to the uniform inflow case. Velocity profiles at several downstream locations demonstrated in Figure 3.43 also indicate that the difference between the maximum velocity deficit values increase at the far wake. Yet, the wake centerline locations for the two cases are quite similar. Consequently, it can be deduced that wake characteristics of the porous disk change under a gusty inflow condition, and phase averaging approach does not result in the same wake flow field as the uniform inflow condition. This may be attributed to the dominance of the gust flow, even in the phase averaged case.

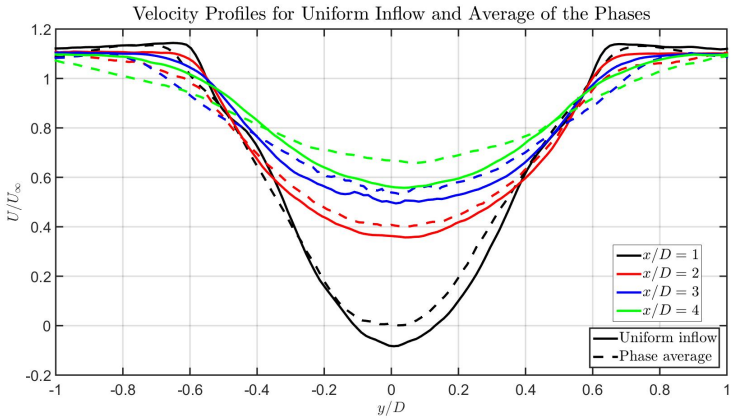


Figure 3.43: Wake deficit comparisons in terms of non-dimensional velocity at different x/D locations ($x/D = 1,\ 2,\ 3,\ 4$) under uniform inflow condition and average of the phases of the motion of the gust vanes for the porous disk.

For the model turbine, on the other hand, the difference in the wake width between the two cases become more significant in the far wake region, similar to the porous disk. For the phase averaged case, comparison of the wake decay trends indicate that wake decays faster for the phase averaged case. Likely, velocity profiles at different downstream locations deduce that at the far wake, maximum velocity deficit values of the uniform inflow and phase averaged cases are quite different.

Comparison between the uniform inflow case to the phase averaged case yields in similar results for the porous disk and the model turbine, which verifies the dominance of the gust flow over the wake characteristics of the two models.

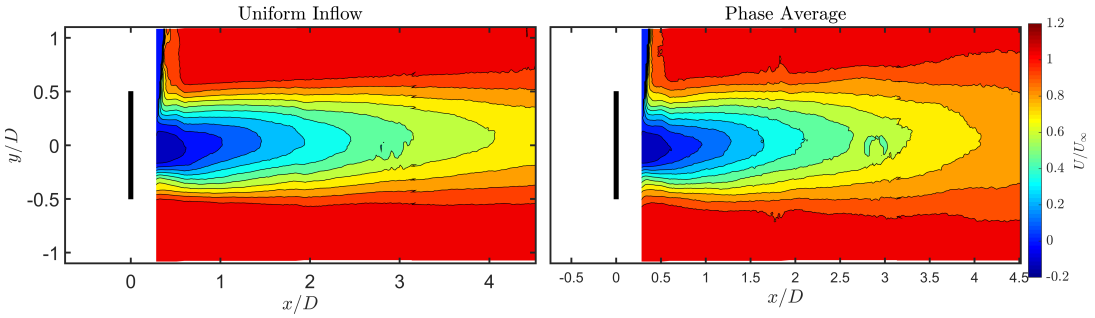


Figure 3.44: Non-dimensional streamwise velocity contours of the model turbine under uniform inflow (left) and the average of the phases of the motion of the gust vanes (right).

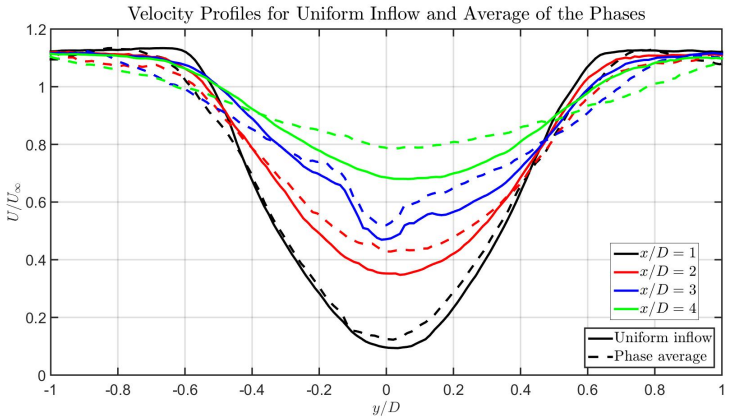


Figure 3.45: Wake deficit comparisons in terms of non-dimensional velocity at different x/D locations ($x/D = 1,\ 2,\ 3,\ 4$) under uniform inflow condition and average of the phases of the motion of the gust vanes for the model turbine.

CHAPTER 4

CONCLUSION AND FUTURE WORK

In this study, a gust generator has been designed, manufactured and integrated into the open-loop suction type C1 wind tunnel located at METUWind (RÜZGEM). Characterization of the gust generator has been done by means of both numerical and experimental studies.

Numerical studies are performed at a reduced frequency range of 0.05-0.55 and the maximum gust ratio downstream of the gust generator is calculated. Based on these, a baseline case is selected such that a transverse gust of sufficient amplitude is generated in the safe operating range of the motors driving the vanes and the wind tunnel and no flow separation occurs. This corresponds to a pitching frequency of 10 Hz, a freestream velocity of 10 m/s, a maximum pitching amplitude of 12° and a vane spacing of $2c$ ($f = 10$ Hz, $U_\infty = 10$ m/s, $\bar{\theta} = 12°$ and $d = 2c$). Then, several parameters are varied and both CFD analyses and PIV measurements are conducted. The gust vanes undergo an in-phase motion, to generate a gust flow in the transverse direction. Yet, as a consequence of changing blockage ratio in the course of the vane motion, a streamwise periodic gust is also generated, with much smaller magnitude.

Firstly, the reduced frequency is varied through varying the pitching frequency and the freestream velocity individually. Both spatial and temporal analysis convey that with an increase in the reduced frequency, the gust ratio increases. Yet, this increase comes with a penalty in the gust uniformity. Consequently, especially if the gust generator is to be utilized for model tests under gust loading, the reduced frequency selection is critical. In addition, two test cases having the same reduced frequency but different actuation parameters prove that although the resulting maximum gust ratios are equal, the flow content, i.e., flow structures, their distribution and gust uniformity,

downstream of the gust generator is different. Thus, a spatial analysis is of critical importance in the selection of actuation parameters for model tests. Moreover, as expected, with an increase in the reduced frequency, the peak location of the gust velocity in a period of motion is delayed and a phase lag occurs.

Secondly, Strouhal number is varied by changing the amplitude of the pitching motion. The results demonstrate that with an increase in the pitching amplitude, which corresponds to an increase in the amplitude of the disturbance, the gust ratio increases. However, for an amplitude of 16°, flow separation is observed. This results in a significant loss in symmetry, homogenity and uniformity of the gust that is generated. Thus, it can be deduced that similar to the reduced frequency, the pitching amplitude selection should also be done considering that a higher gust ratio may come with a penalty in symmetry and homogenity.

Finally, the distance between the vanes is varied and the resulting flow field is explored. Results indicate that the case with the maximum vane spacing provides the most uniform flow field. The area of the useful working section also increases with the vane spacing, yet, the magnitude of the gust that can be generated decreases. Thus, it can be concluded that the actuation parameters and the distance between the vanes may result in both advantageous and disadvantageous effects on the resulting flow field such that a trade-off study must be performed in the selection of these parameters. To explore the flow content and its evolution further downstream of the gust generator, instead of the commonly preferred pointwise measurement techniques, a full field investigation should be conducted.

After the characterization of the gust generator, as an application, a porous disk and a model wind turbine having the same thrust coefficients are placed $3c$ downstream of the gust generator. Results reveal that the capacity of a porous disk in mimicking a wind turbine demolishes under a gust inflow condition, especially in the far wake.

To extend the work that is demonstrated in this thesis, some ideas regarding future work should be discussed. To begin with, it has been observed that certification requirements for air vehicles require an analysis of gust with a $1 - \cos$ profile. In this respect, in addition to a sinusoidal transverse gust, motion protocols of the wings may be altered such that an appropriate displacement is designed for the vanes and the re-

sulting flow fields can be investigated. The present work regarding the generation of $1 - \cos$ profiled gusts in wind tunnels reveal that imposing a vane motion in $1 - \cos$ form fails to generate a gust flow in the desired profile [51]. Thus, the appropriate vane motion protocol should be sought for.

To continue, to eliminate the potential errors that are encountered as a result of limited discretization of a period of the motion, discretication interval, i.e. $4°$, can be reduced or high speed PIV tests can be conducted utilizing a high speed laser system. Finally, a gust generator can be designed to be integrated to the Large Scale Wind Tunnel in RÜZGEM, based on the findings of this study. Both experimental and numerical investigations should be made for the design and characterization of the new setup, following the methodology presented in this thesis.

REFERENCES

[1] Z. Wu, Y. Cao and M. Ismail. Gust Loads on Aircraft. *The Aeronautical Journal*, Vol. 123, No. 1266, pp. 1216,1274, August 2019. doi:10.1017/aer.2019.48

[2] J. Hunsaker. Report on Behavior of Aeroplanes in Gusts. *NACA Report*, 1915.

[3] E.B. Wilson. Theory of an Aeroplane Encountering Gusts. *Proceedings of the National Academy of Sciences of the United States of America*, Vol. 2, pp. 294-297, 1916.

[4] Smithson. The Wright Flyer: from invention to icon.. *Smithson National Aerospace Museum*, 1999. https://airandspace.si.edu/exhibitions/wright-brothers/online/icon/1903.cfm

[5] I. Andreu-Angulo, H. Babinsky, H. Biler, G. Sedky and A.R. Jones. Effect of Transverse Gust Velocity Profiles. *AIAA Journal*, Vol. 58, No. 12, 2020. doi:10.2514/1.J059665

[6] A.R. Jones, O. Cetiner and M.J. Smith. Physics and Modeling of Large Flow Disturbances: Discrete Gust Encounters for Modern Air Vehicles. *Annual Review of Fluid Mechanics*, Vol. 54:4, pp. 469-493, 2022. doi:10.1146/annurev-fluid-031621-085520

[7] K. Engin, E. Aydin, B. Zaloglu, I. Fenercioglu and O. Cetiner. Large Scale Spanwise Periodic Vortex Gusts or Single Spanwise Vortex Impinging on a Rectangular Wing. *Fluid Dynamics Conference*, 2018, *AIAA Paper* pp. 2018-3086, 2018. doi:10.2514/6.2018-3086

[8] J. Chowdhury, L. Cook and M.J. Ringuette. The Vortex Formation of an Unsteady Translating Plate with a Rotating Tip. *AIAA Aerospace Sciences Meeting*, 2019. *AIAA Paper*, 2019-0348. doi:10.2514/6.2019-0348

[9] Ü. Gülçat. Fundamentals of Modern Unsteady Aerodynamics. *Springer*, 2010. doi:10.1007/978-3-642-14761-6

[10] H.G. Küssner. Untersuchung der Bewegung einer Platte Beim Eintrill in Eine Strahlgrenze. *Luftfahrtforschung*, Vol. 13, p.425, 1930.

[11] J.D. Anderson. Fundamentals of Aerodynamics. *Mc-Graw Hill*, 5th ed., Vol. 1, Chapter 4, London, 2011. doi:10.1017/CBO9781107415324.004

[12] Certification Specifications for Large Aeroplanes, CS-25. *European Aviation Safety Ajency*, September 2007.

[13] Certification Specifications for Very Light Aeroplanes, CS-VLA. *European Aviation Safety Ajency*, March 2009.

[14] Flying Qualities of Piloted Aircraft. *Department of Defense Interface Standard*, August 2004.

[15] Federal Aviation Administration. *U.S. Department of Transportation*, September 2003.

[16] V. Brion, A. Lepage, Y. Amosse, D. Soulevant, P. Senecat, J.C. Abart and P. Paillart. Generation of vertical gusts in a transonic wind tunnel. *Journal of Experiments in Fluids*, Vol. 56, Number 145, 2015. doi:10.1007/s00348-015-2016-5

[17] B. Reginald, B. Bland and T. Reisert. An application of statistical data in the development of gust load criterions. *NASA Technical Report*, NASA TN 1268, 1947.

[18] A. Onol and S. Yesilyurt. Onol A., Yesilyurt S., 2017, Effects of wind gusts on a vertical axis wind turbine with high solidity. *Journal of Wind Engineering and Industrial Aerodynamics*, Vol. 162, pp. 1-11, 2017. doi:10.1016/j.jweia.2017.01.003

[19] F. Spinato, P.J. Tavner, G. van Bussel and E. Koutoulakos. Reliability of wind turbine subassemblies IET Proceedings. *IET Renewable Power Generation*, Vol. 3, Issue 4, pp. 1-15, 2009. doi:10.1049/iet-rpg.2008.0060

[20] I. Yigili, M.A. Andirin, M.T. Akpolat, O. Baskan, M. Percin and O. Uzol. Design of a gust generator and comparison of model wind turbine and porous disc wake flows in a transverse gust. *Journal of Physics: Conference Series*, Vol. 2265, Issue 2, Wind and Wind Farms; Measurement and Testing, 2022. doi:10.1088/1742-6596/2265/2/022108

[21] P. Singh, L.Ñeuhaus, O. Huxdorf, J. Riemenschneider, J. Wild, J. Peinke and M. Hölling. Experimental investigation of an active slat for airfoil load alleviation. *Journal Renewable Sustainable Energy*, Vol. 13, Issue 4, 2021. doi:10.1063/5.0045846

[22] Guideline for the Certification of Wind Turbines. *Germanischer Lloyd*, Hamburg, July 2010.

[23] I. Andreu-Angulo and H. Babinsky. Negating Gust Effects by Actively Pitching a Wing. *AIAA Aerospace Sciences Meeting*, January 2020. *AIAA Paper*, 2020-1057. doi:10.2514/6.2020-1057

[24] H. Tennekes. The Simple Science of Flight. *MIT Press*, Cambridge, MA, 2009, Chap. 3.

[25] N.J. Wei, J. Kissing, T.T.B. Wester, S. Wegt, K. Schiffmann, S. Jakirlic, M. Holling, J. Peinke and C. Tropea. Insights into the periodic gust response of airfoils. *Journal of Fluid Mechanics*, Vol. 876, pp. 237-263, July 2019. doi:10.1017/jfm.2019.537

[26] D.A. Buell. An experimental investigation of the velocity fluctuations behind oscillating vanes. *Technical Note D-5543, NASA*, Ames Research Center, Moffett Field, CA, November 1969. Document ID:19700001995

[27] K.T. Wood, R.C. Cheung, T.S. Richardson, J.E. Cooper, O. Darbyshire and C. Warsop. A New Gust Generator for a Low Speed Wind Tunnel: Design and Commissioning. *55th AIAA Aerospace Sciences Meeting*, January 2017. doi:10.2514/6.2017-0502

[28] P.M.G.J. Lancelot, J. Sodja, N.P.M. Werter, and R. De Breuker. Design and testing of a low subsonic wind tunnel gust generator. *Advances in Aircraft and Spacecraft Science*, Vol. 4, Number 2, pp. 125-144, March 2017. doi:10.12989/aas.2017.4.2.125

[29] J. Neumann and M. Holger. Gust response: Simulation of an aeroelastic experiment by a fluid-structure interaction method. *Journal of Fluids and Structures*, Vol. 38, pp. 209-302, April 2013. doi:10.1016/j.jfluidstructs.2012.12.007

[30] D. Grissom and W. Devenport. Development and Testing of a Deterministic Disturbance Generator. *10th AIAA/CEAS Aeroacoustics Conference*, Manchester, Great Britain, May 2004. doi:10.2514/6.2004-2956

[31] A.J. Saddington, M.V. Finnis and K. Knowles. The characterisation of a gust generator for aerodynamic testing. *Proc IMechE Part G: J Aerospace Engineering*, Vol. 229, Issue 7, pp. 1214-1225, 2015. doi:10.1177/0954410014548237

[32] F. Fernandez, D. Cleaver and I. Gursul. Unsteady aerodynamics of a wing in a novel small-amplitude transverse gust generator. *Experiments in Fluids*, Vol. 62, Number 9, 2021. doi:10.1007/s00348-020-03100-8

[33] X. He, D.R. Williams and S.T.M. Dawson. Transverse gust generation in a wind tunnel: a suction-driven approach. *Experiments in Fluids*, Vol. 63, Number 125, 2022. doi:10.1007/s00348-022-03484-9

[34] T.T.B Wester, J. Krauss, L. Neuhaus, A. Hölling, G. Gülker, M. Hölling and J. Peinke. How to Design a 2D Active Grid for Dynamic Infow Modulation. *Flow, Turbulence and Combustion*, Vol. 108, pp. 955-972, 2022. doi:10.1007/s10494-021-00312-8

[35] I. Yigili, M.A. Andirin, E. Kurban, O. Baskan and M Percin. Design and experimental investigation of a wind tunnel gust generator. *Ankara International Aerospace Conference*, METU, Ankara, September 2021.

[36] A. French, W. Friess, A. Goupee and K. Berube. Design, Construction and Evaluation of an Oscillating Vane Gust Generator for Atmospheric Flow Simulation . *Wind*, Vol. 1, pp. 63-76, 2021. doi:10.3390/wind1010004

[37] B. Ozturk, A. Hassanein, M.T. Akpolat, A. Abdulrahim, M. Percin and O. Uzol. Effects of freestream turbulence on the wake growth rate of a model wind turbine and a porous disc. *Journal of Physics: Conference Series*, Vol. 2265, Issue 2, Wind and Wind Farms; Measurement and Testing, 2022. doi:10.1088/1742-6596/2265/2/022042

[38] S. Aubrun, S. Loyer, P.E. Hancock and P. Hayden. Wind turbine wake properties: Comparison between a non-rotating simplified wind turbine model and a

rotating model. *Journal of Wind Engineering and Industrial Aerodynamics*, Vol. 120, pp. 1-8, 2013. doi:10.1016/j.jweia.2013.06.007

[39] L.E.M. Lignarolo, D. Ragni, C.J. Ferreira and G.J.W. van Bussel. Experimental comparison of a wind-turbine and of an actuator-disc near wake. *Journal of Renewable and Sustainable Energy*, Vol. 8, Issue 2, 2016. doi:10.1063/1.4941926

[40] A. Abdulrahim, M.T. Akpolat, A. Hassanein, M. Percin and O. Uzol. Comparison of Analytical Wake Model Predictions with Experimental Data for a Non-Uniform Porous Disc for Uniform and Non-Uniform Inflow Conditions. *Wind Energy Science Conference (WESC)*Leibniz University, Hannover, Germany, May 25-28, 2021.

[41] E.H. Camp and R.B. Cal. *Mean kinetic energy transport and event classification in a model wind turbine array versus an array of porous disks: Energy budget and octant analysis*. *Physical Review Fluids*, Vol. 1, Issue 4, August 2016. doi:10.1103/PhysRevFluids.1.044404

[42] I. Neunaber. *Stochastic investigation of the evolution of small-scale turbulence in the wake of a wind turbine exposed to different inflow conditions*. PhD Thesis, Carl von Ossietzky Universitat, January 2019.

[43] S. Aubrun, M. Bastankhah, R.B. Cal, B. Conan, R.J. Hearst, D. Hoek, M. Hölling, M. Huang, C. Hur, B. Karlsen, I. Neunaber, M. Obligado, J. Peinke, M. Percin, L. Saetran, P. Schito, B. Schliffke, D. Sims-Williams, O. Uzol, M.K. Vinnes and A. Zasso. *Round-robin tests of porous disc models*. *Journal of Physics: Conference Series*, Vol. 1256, 2019. doi:10.1088/1742-6596/1256/1/012004

[44] E. Lazar, B. de Blauw, N. Glumac, C. Dutton and G. Elliot. *A practical approach to PIV uncertainty analysis . 27th AIAA Aerodynamic Measurement Technology and Ground Testing Conf.*, Chicago, Illinois, 2010.

[45] A Sciacchitano. *Uncertainty quantifcation in particle image velocimetry*. *Measurement Science and Technology*, Vol. 30, 2019. doi:10.1088/1361-6501/ab1db8

[46] C. Brossard, J.C. Monier, P. Barricau, F.X. Vandernoot, Y. Le Sant, F. Champagnat and G. Le Besnerais. *Principles and applications of particle image velocime-*

try. *Aerospace Lab*. Alain Appriou, 2009, pp. 1-11, 2009. https://hal.archives-ouvertes.fr/hal-01180587

[47] R.I. Rubel, M.K. Uddin, M.Z. Islam and M. Rokunuzzaman. *Comparison of Aerodynamics Characteristics of NACA 0015 & NACA 4415*. *Preprints*, 2016. doi:10.20944/preprints201610.0095.v1

[48] M.A. Andirin. Generation and Experimental Investigations of Gusty Flows in Wind Tunnels. *M.S. Thesis*, Middle East Technical University, 2022. https://hdl.handle.net/11511/98159

[49] M. Dular and R. Bachert. The Issue of Strouhal Number Definition in Cavitating Flow. *Journal of Mechanical Engineering*, Vol. 55, Issue 11, pp. 666-674, 2009.

[50] C.O. Johnston. Review, Extension, and Application of Unsteady Thin Airfoil Theory. *Center for Intelligent Material Systems and Structures (CIMSS) Report No. 04-101*, Virginia Polytechnic Institute and State University Blacksburg, VA, 24060, August 2004.

[51] D. Balatti, M. Manolesos, H.H. Khodaparast and M.I. Friswell. Generating a '1-cos' gust profiles in a wind tunnel. *Online Symposium on Aeroelasticity, Fluid-Structure Interaction, and Vibrations*, October 2021.

[52] A. Boccazzi and R. Miorini. TURBOMACHINERY FLOW MEASUREMENTS BY MEANS OF PARTICLE IMAGE VELOCIMETRY AT POLITECNICO DI MILANO. *XV AIVELA ANNUAL NATIONAL MEETING*, Milan, November 2007.

APPENDIX A

CONTOUR PLOTS OF ALL TEST CASES

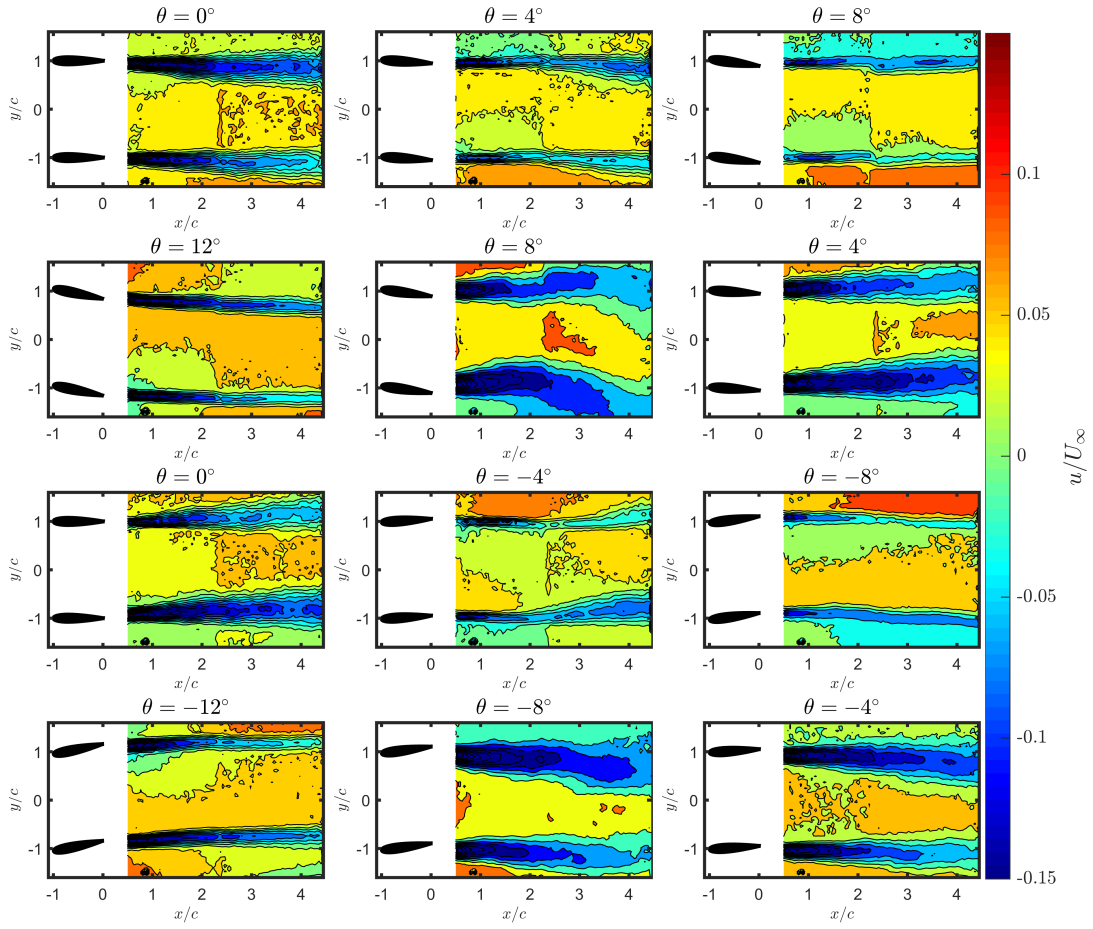


Figure A.1: PIV measurement results for the case $f = 2.5$ Hz, $U_\infty = 10$ m/s, $d = 2c$, $\bar{\theta} = 12°$. Variation of streamwise velocity component.

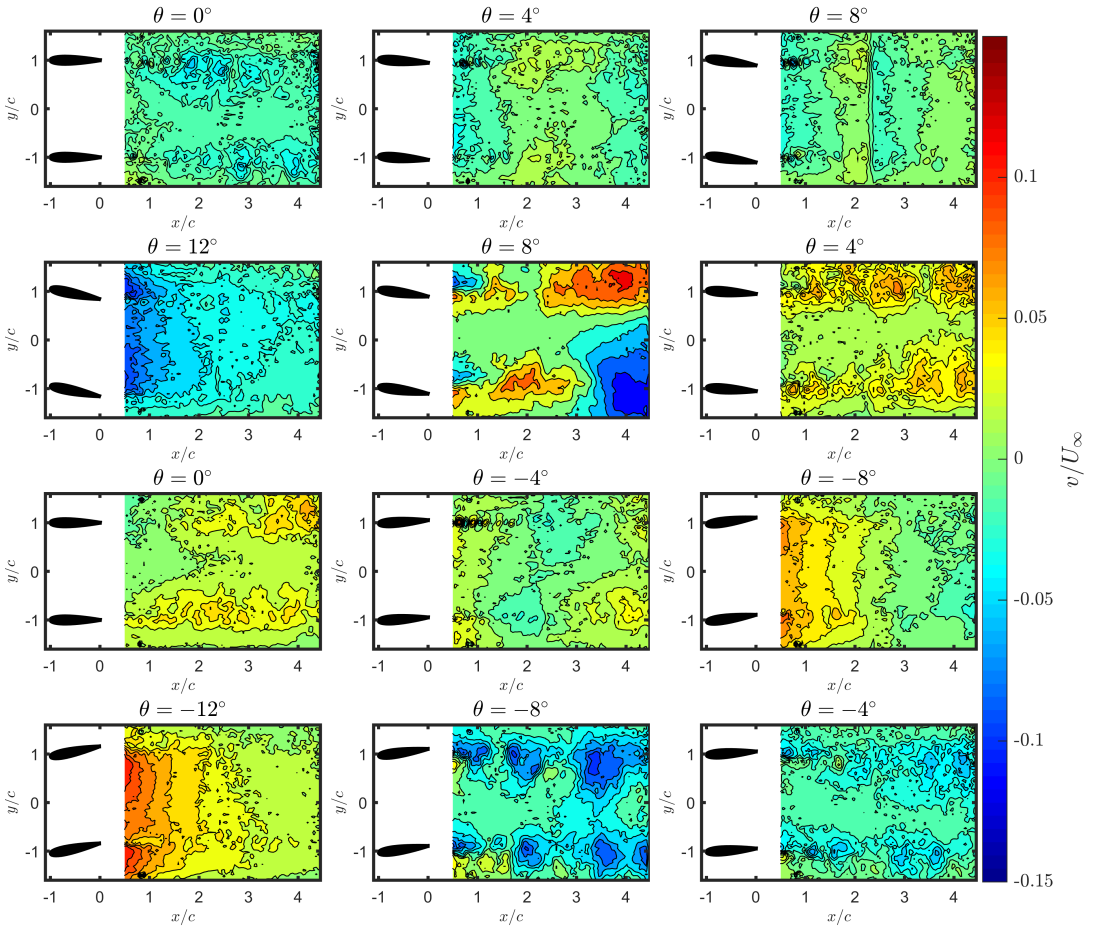


Figure A.2: PIV measurement results for the case $f = 2.5$ Hz, $U_\infty = 10$ m/s, $d = 2c$, $\bar{\theta} = 12°$. Variation of transverse velocity component.

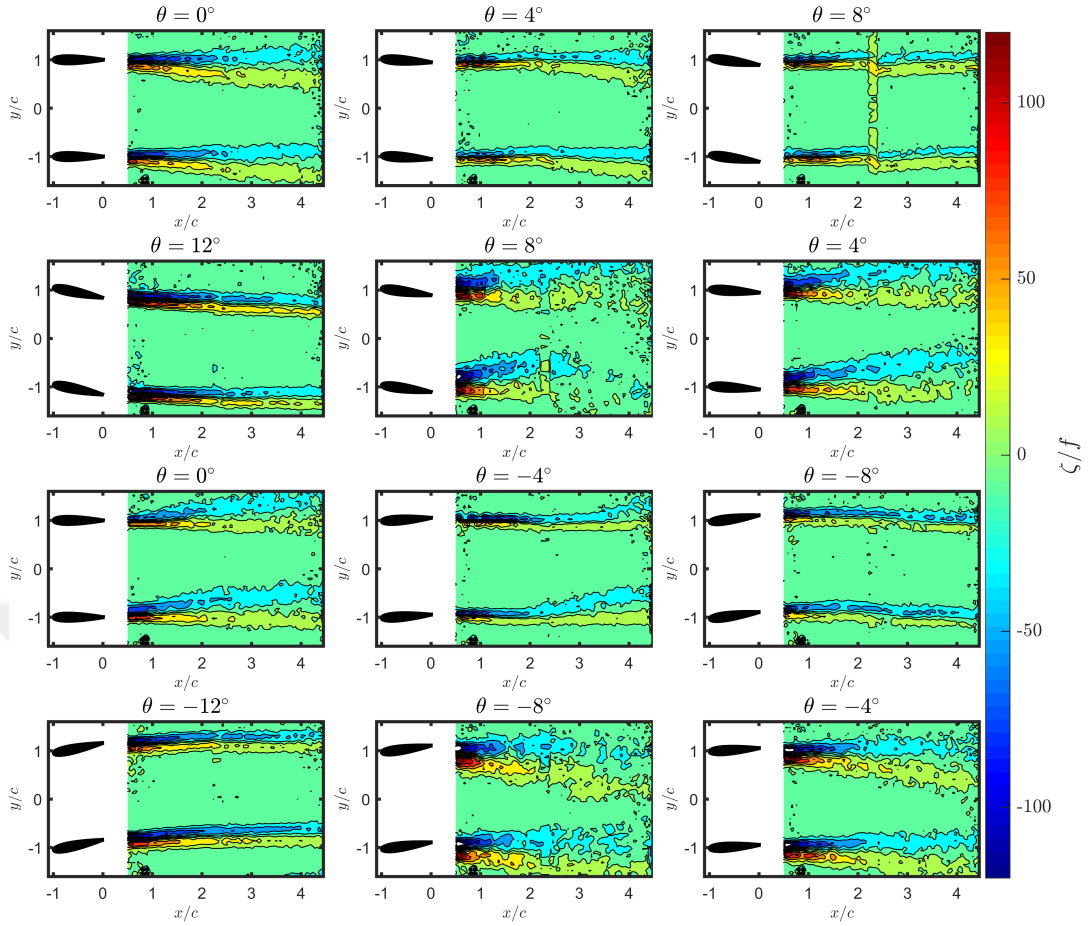


Figure A.3: PIV measurement results for the case $f = 2.5$ Hz, $U_\infty = 10$ m/s, $d = 2c$, $\bar{\theta} = 12°$. Variation of vorticity.

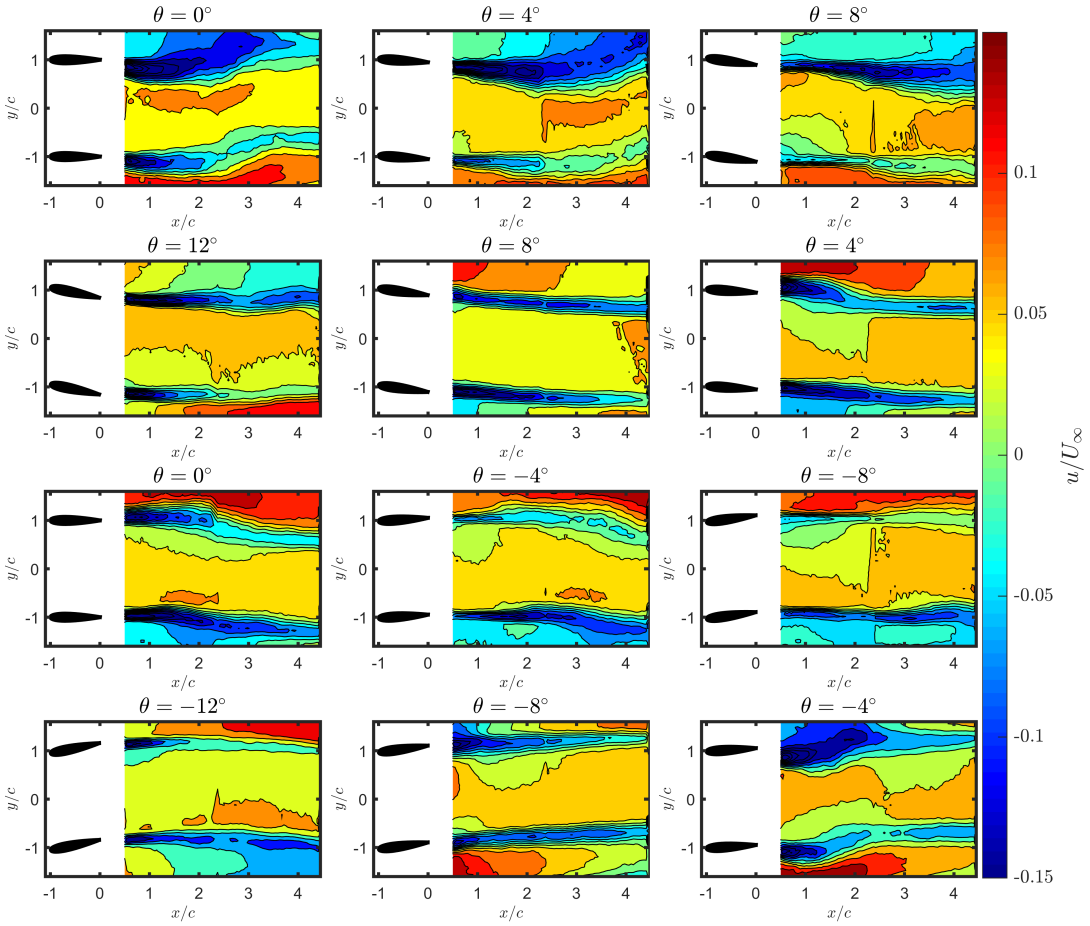


Figure A.4: PIV measurement results for the case $f = 5$ Hz, $U_\infty = 10$ m/s, $d = 2c$, $\bar{\theta} = 12°$. Variation of streamwise velocity component.

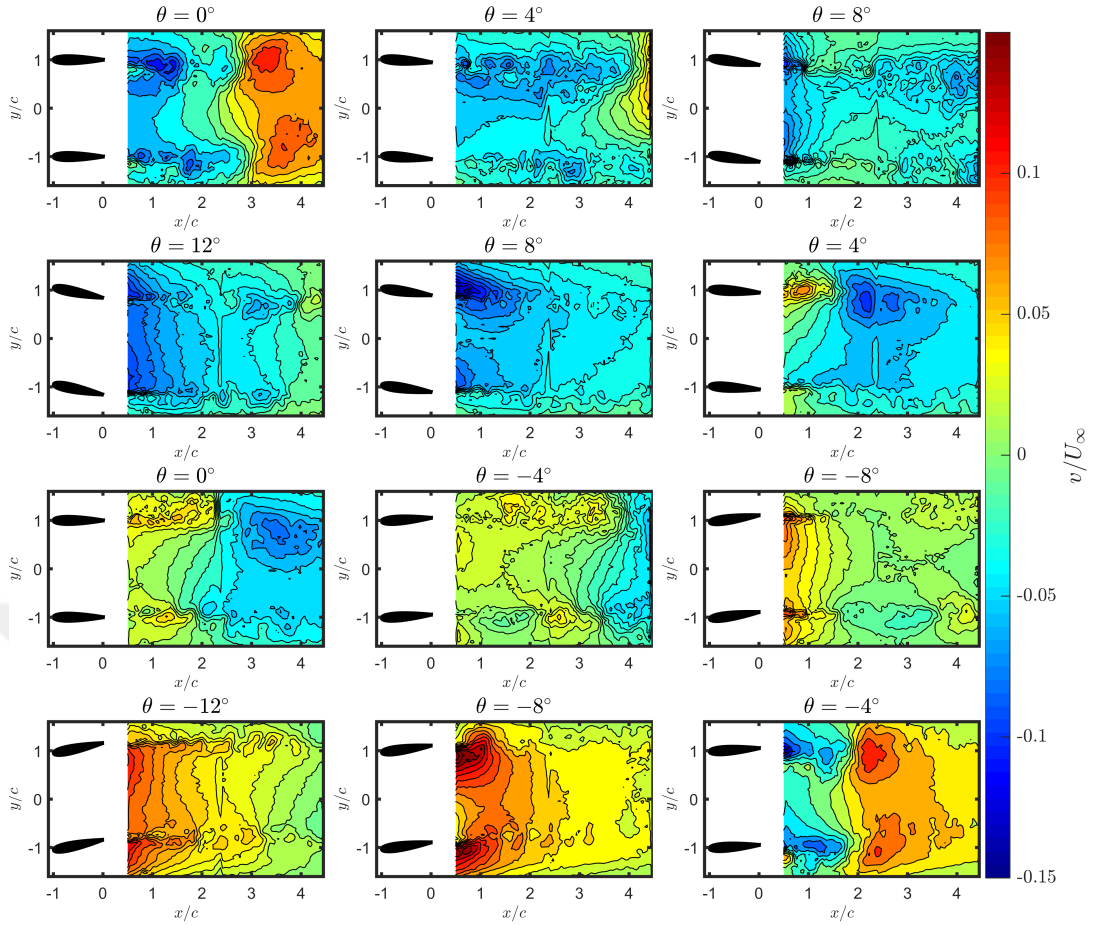


Figure A.5: PIV measurement results for the case $f = 5$ Hz, $U_\infty = 10$ m/s, $d = 2c$, $\bar{\theta} = 12°$. Variation of transverse velocity component.

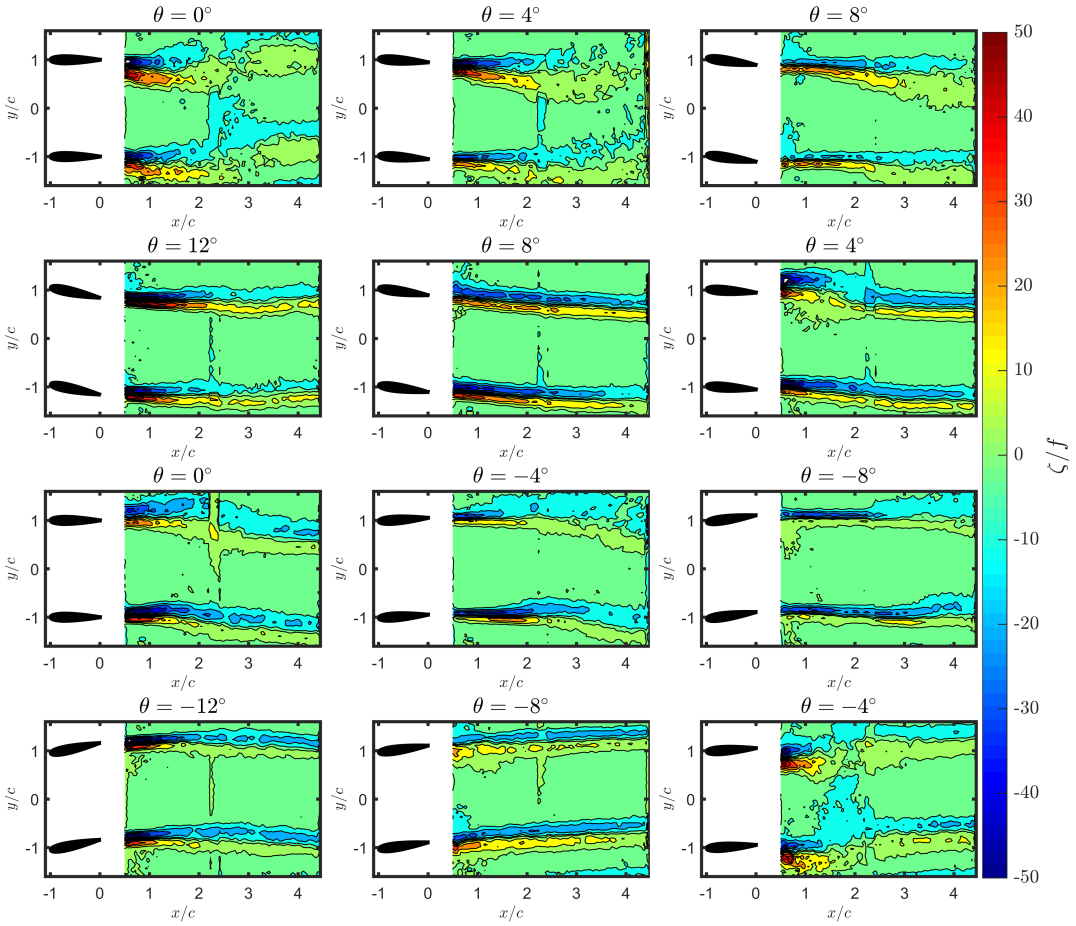


Figure A.6: PIV measurement results for the case $f = 5$ Hz, $U_\infty = 10$ m/s, $d = 2c$, $\bar{\theta} = 12°$. Variation of vorticity.

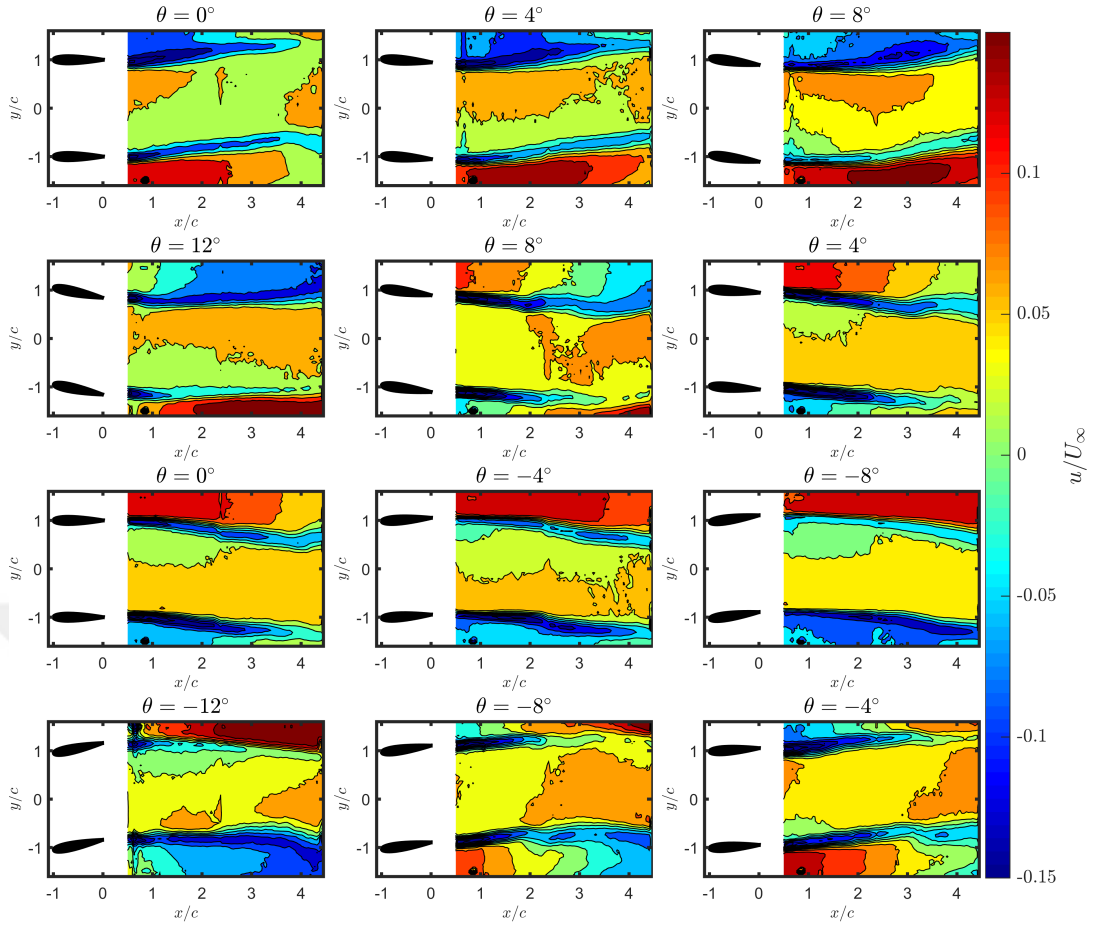


Figure A.7: PIV measurement results for the case $f = 7.5$ Hz, $U_\infty = 10$ m/s, $d = 2c$, $\bar{\theta} = 12°$. Variation of streamwise velocity component.

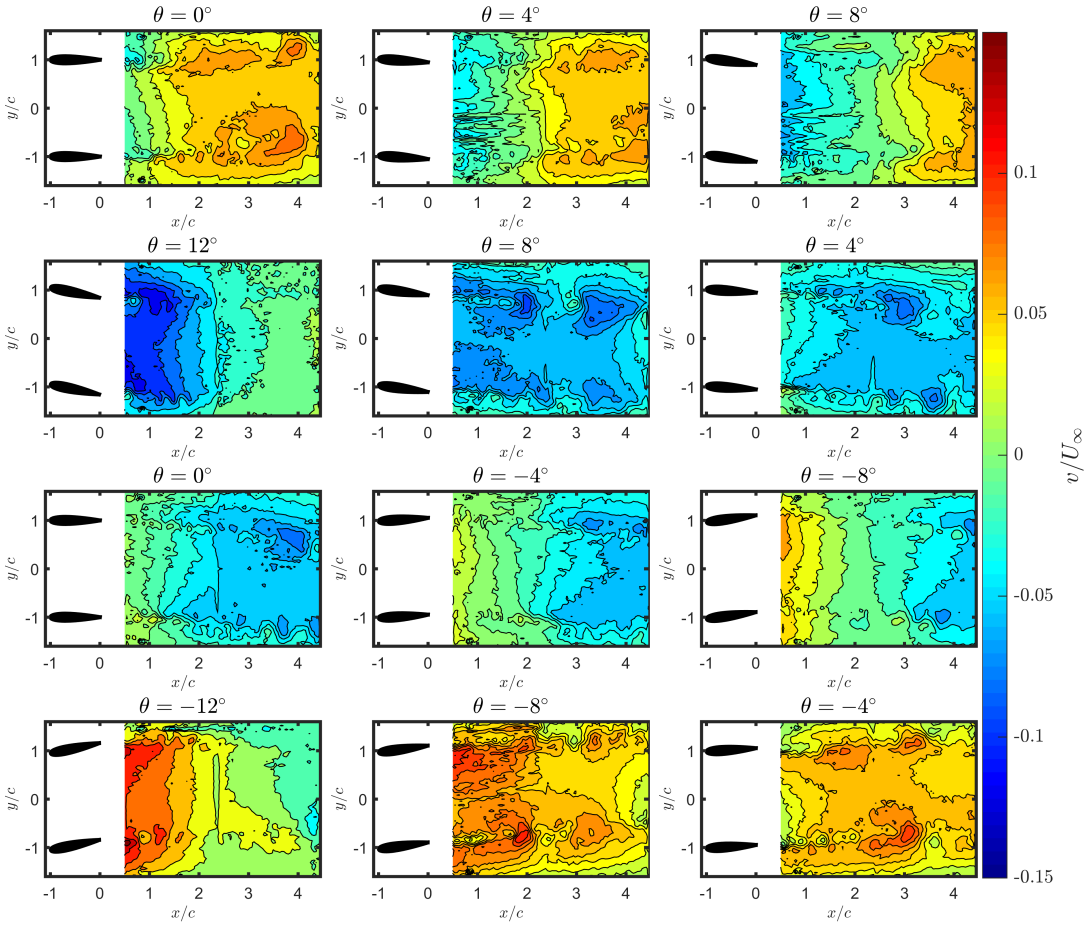


Figure A.8: PIV measurement results for the case $f = 7.5$ Hz, $U_\infty = 10$ m/s, $d = 2c$, $\bar{\theta} = 12°$. Variation of transverse velocity component.

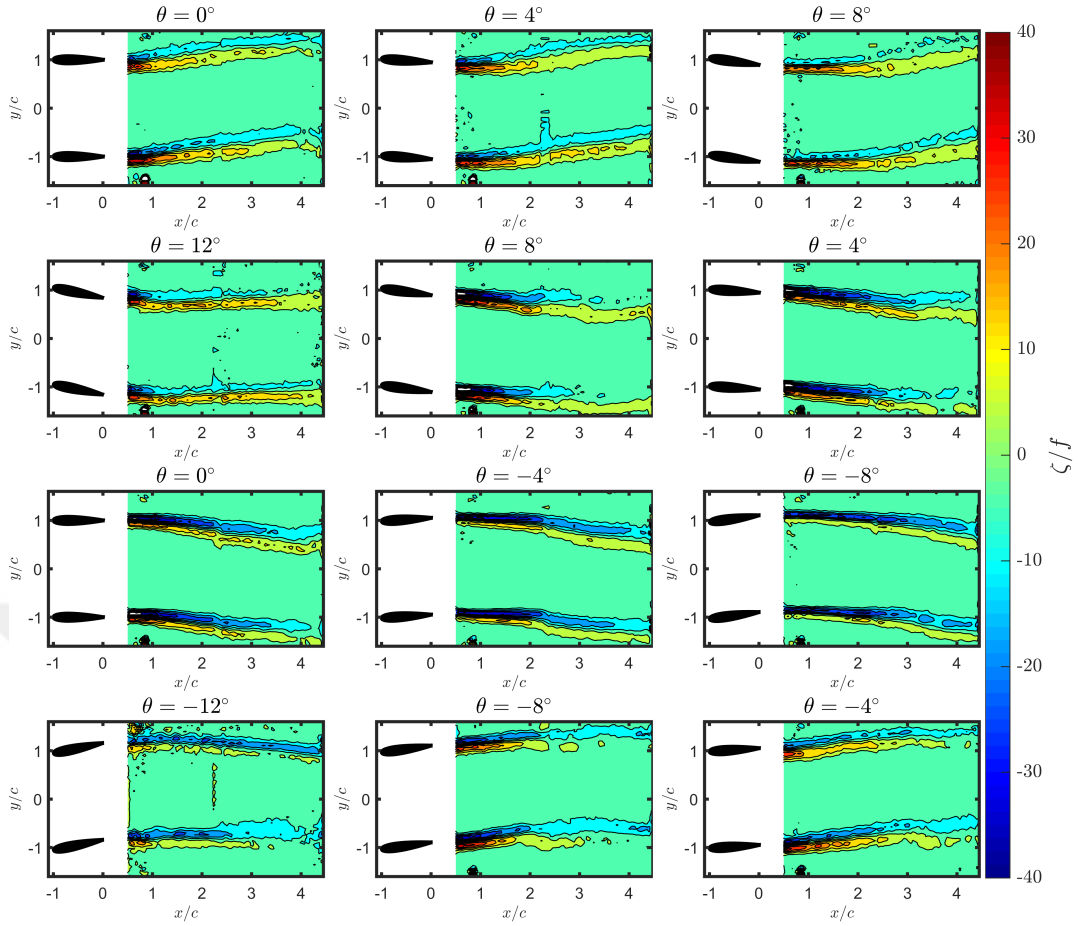


Figure A.9: PIV measurement results for the case $f = 7.5$ Hz, $U_\infty = 10$ m/s, $d = 2c$, $\bar{\theta} = 12°$. Variation of vorticity.

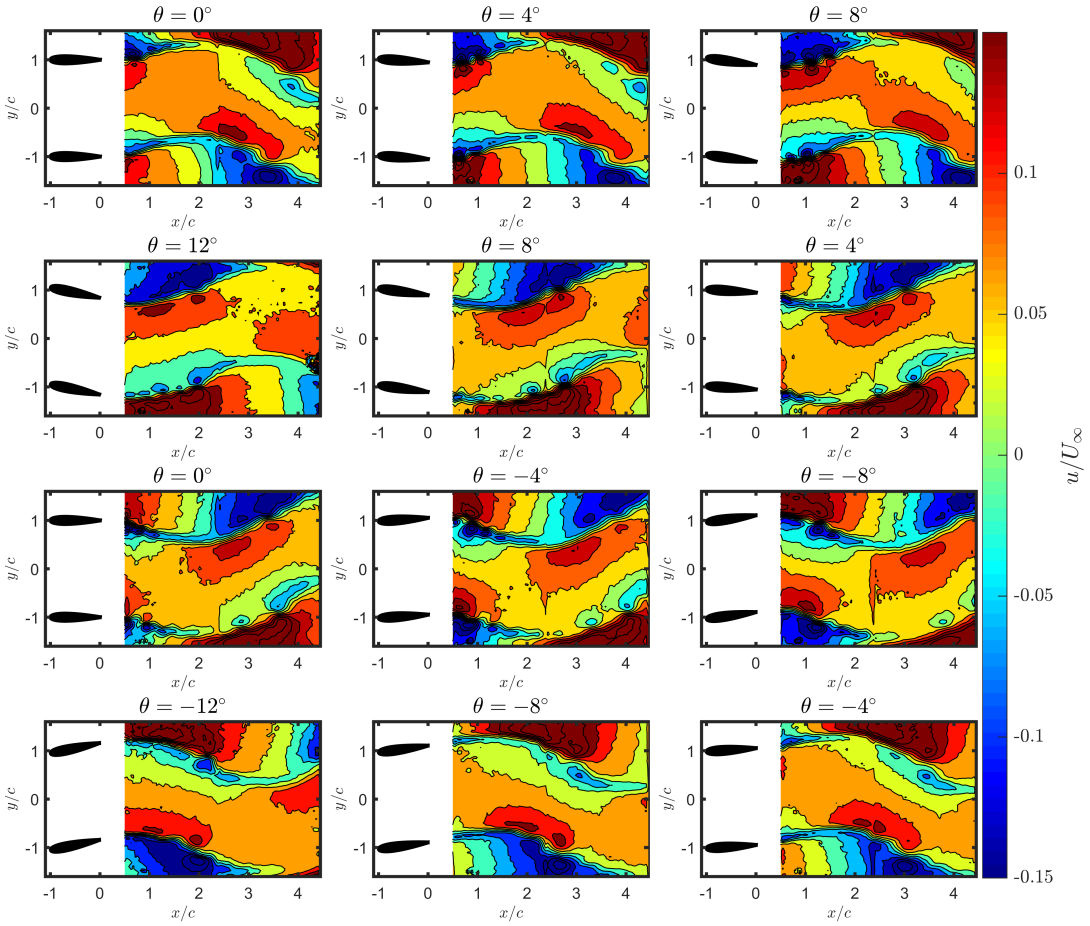


Figure A.10: PIV measurement results for the case $f = 10$ Hz, $U_\infty = 5$ m/s, $d = 2c$, $\bar{\theta} = 12°$. Variation of streamwise velocity component.

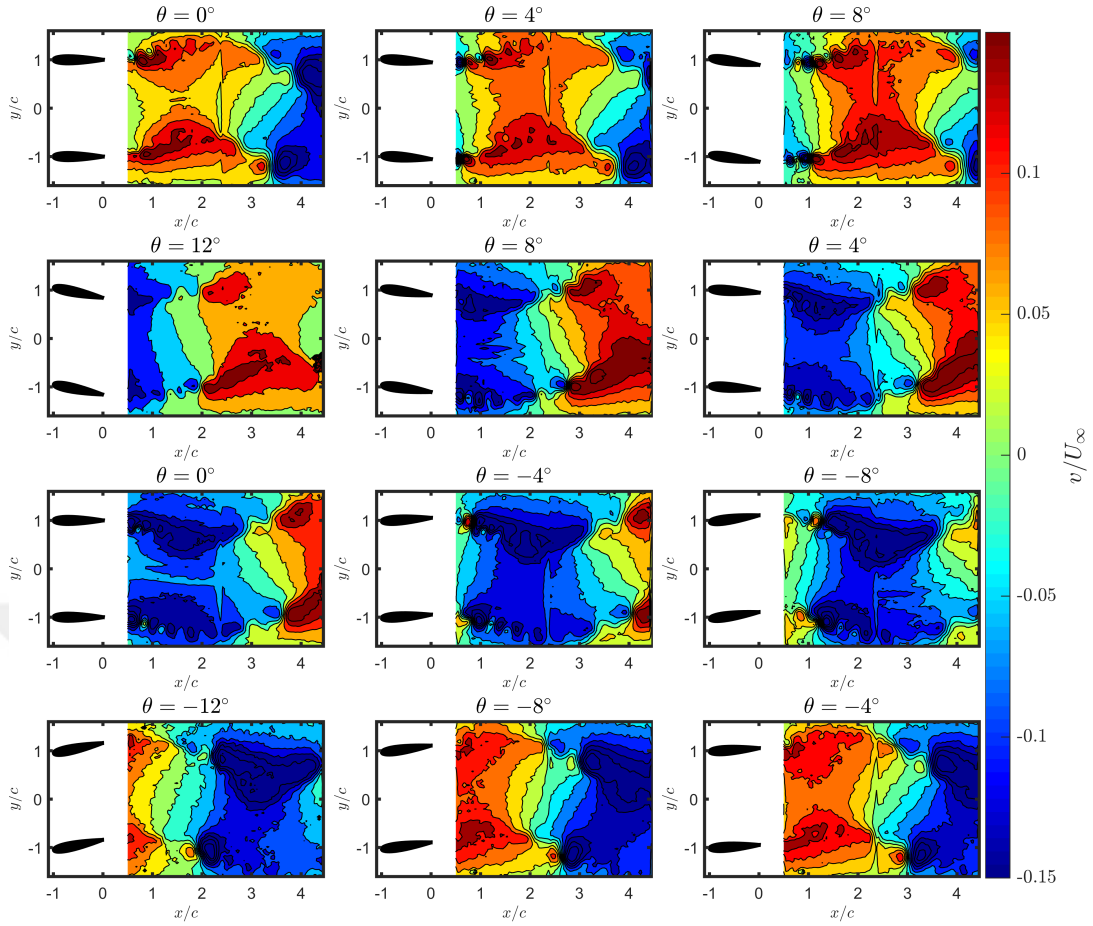


Figure A.11: PIV measurement results for the case $f = 10$ Hz, $U_\infty = 5$ m/s, $d = 2c$ $\bar{\theta} = 12°$. Variation of transverse velocity component.

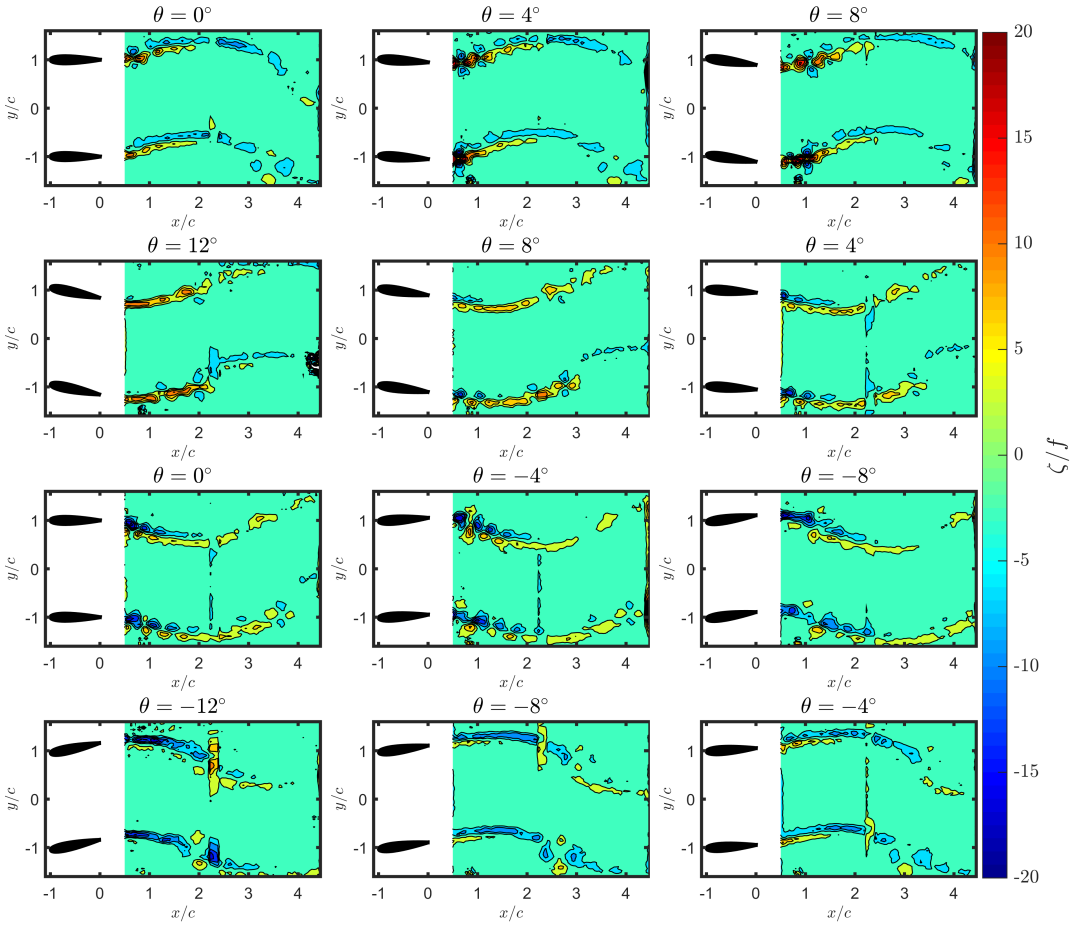


Figure A.12: PIV measurement results for the case $f = 10$ Hz, $U_\infty = 5$ m/s, $d = 2c$ $\bar{\theta} = 12°$. Variation of vorticity.

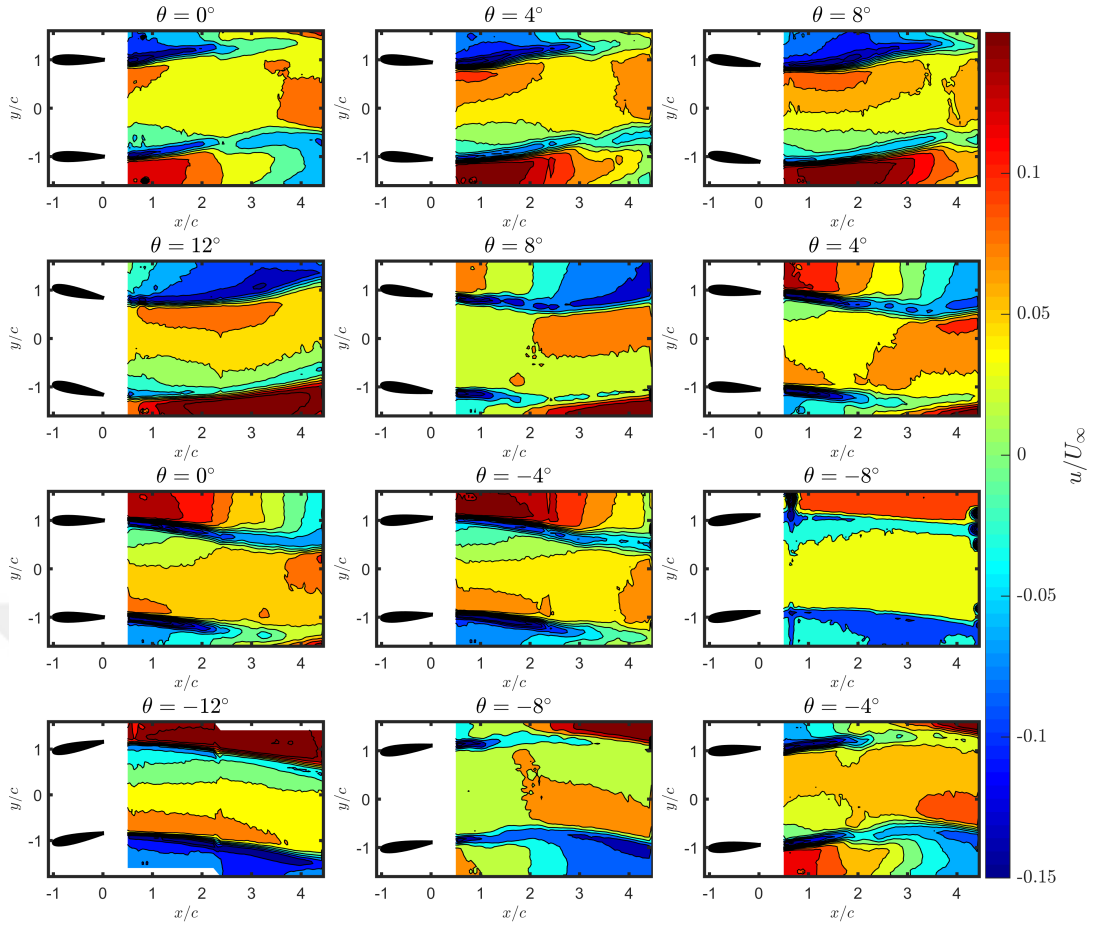


Figure A.13: PIV measurement results for the case $f = 10$ Hz, $U_\infty = 10$ m/s, $d = 2c$, $\bar{\theta} = 12°$ (baseline case). Variation of streamwise velocity component.

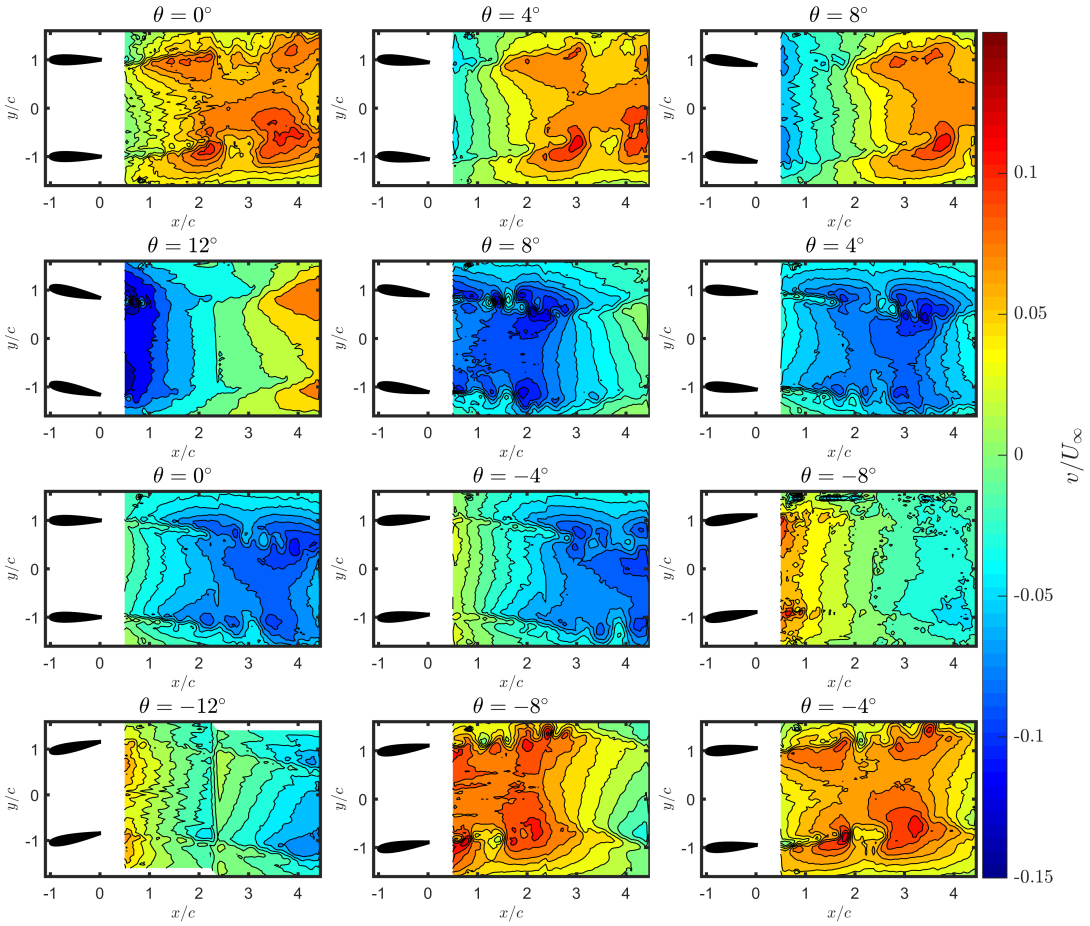


Figure A.14: PIV measurement results for the case $f = 10$ Hz, $U_\infty = 10$ m/s, $d = 2c$, $\bar{\theta} = 12°$ (baseline case). Variation of transverse velocity component.

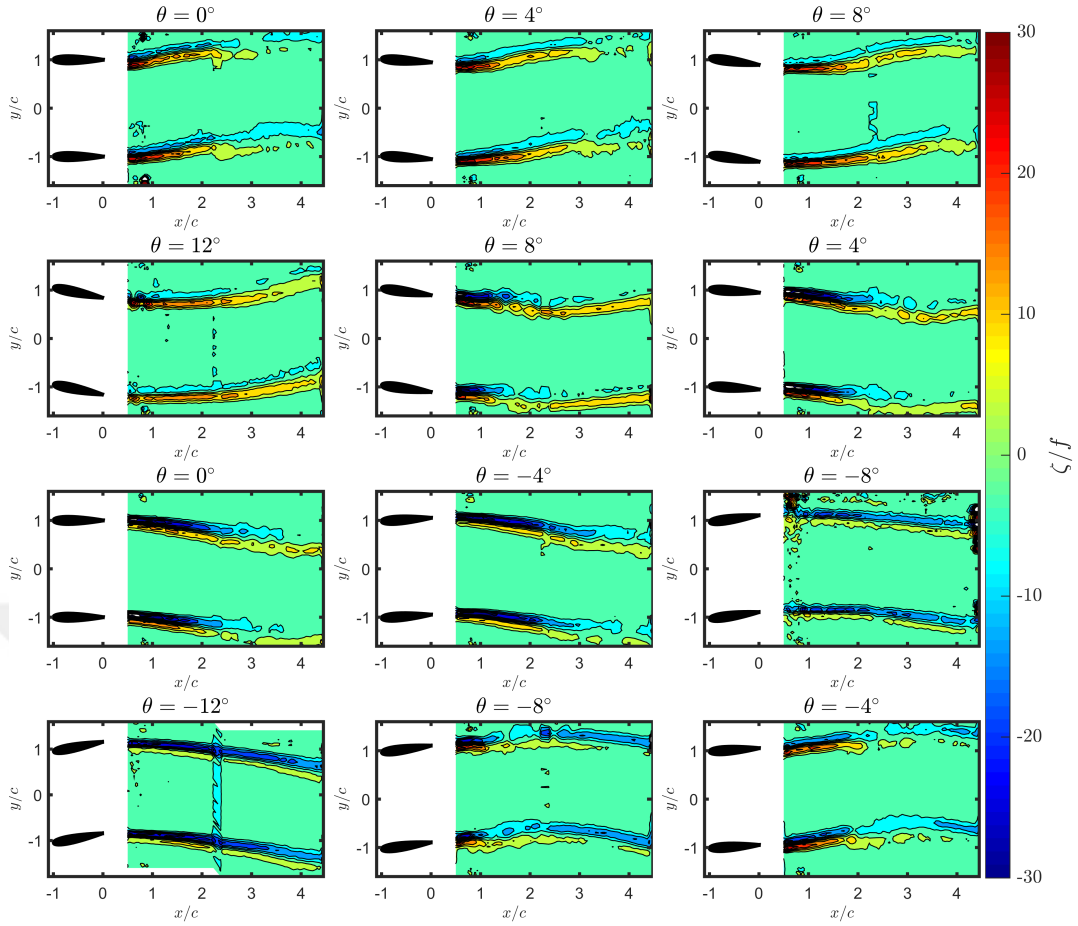


Figure A.15: PIV measurement results for the case $f = 10$ Hz, $U_\infty = 10$ m/s, $d = 2c$, $\bar{\theta} = 12°$ (baseline case). Variation of vorticity.

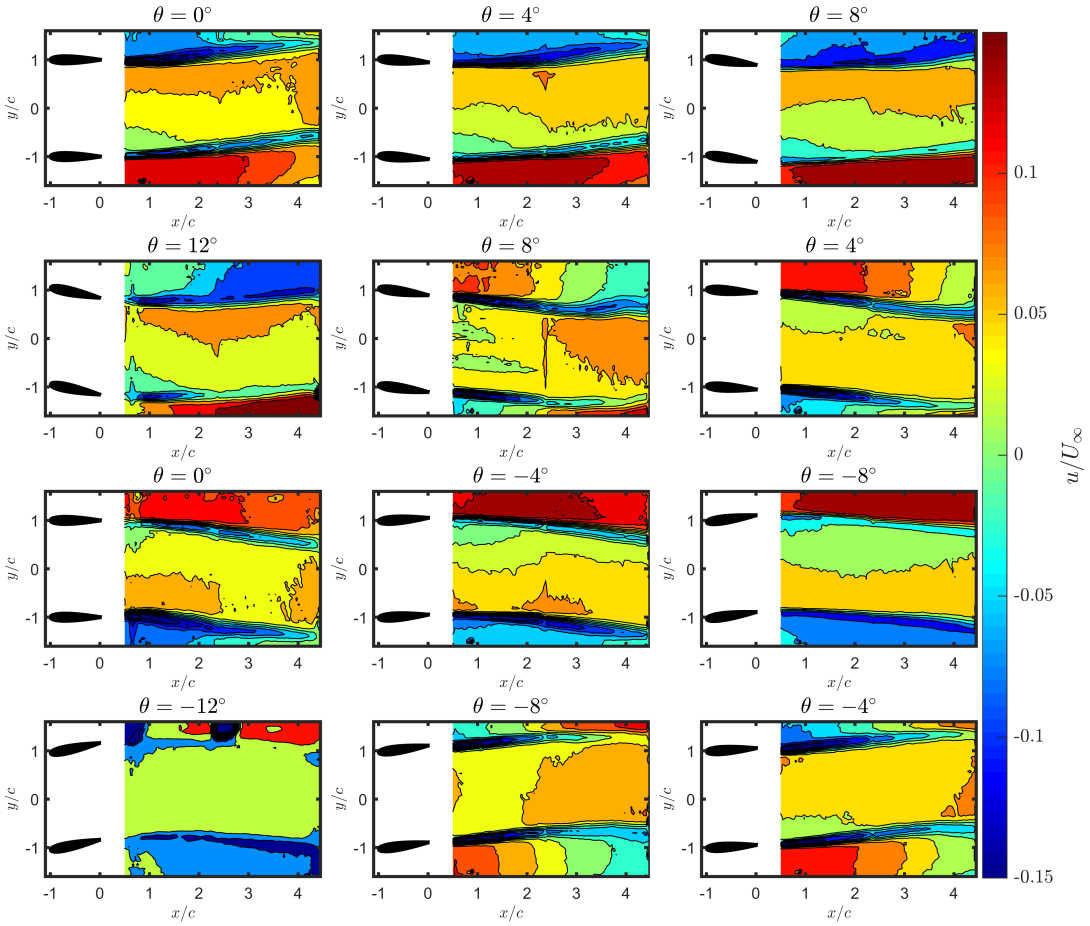


Figure A.16: PIV measurement results for the case $f = 10$ Hz, $U_\infty = 15$ m/s, $d = 2c$ $\bar{\theta} = 12°$. Variation of streamwise velocity component.

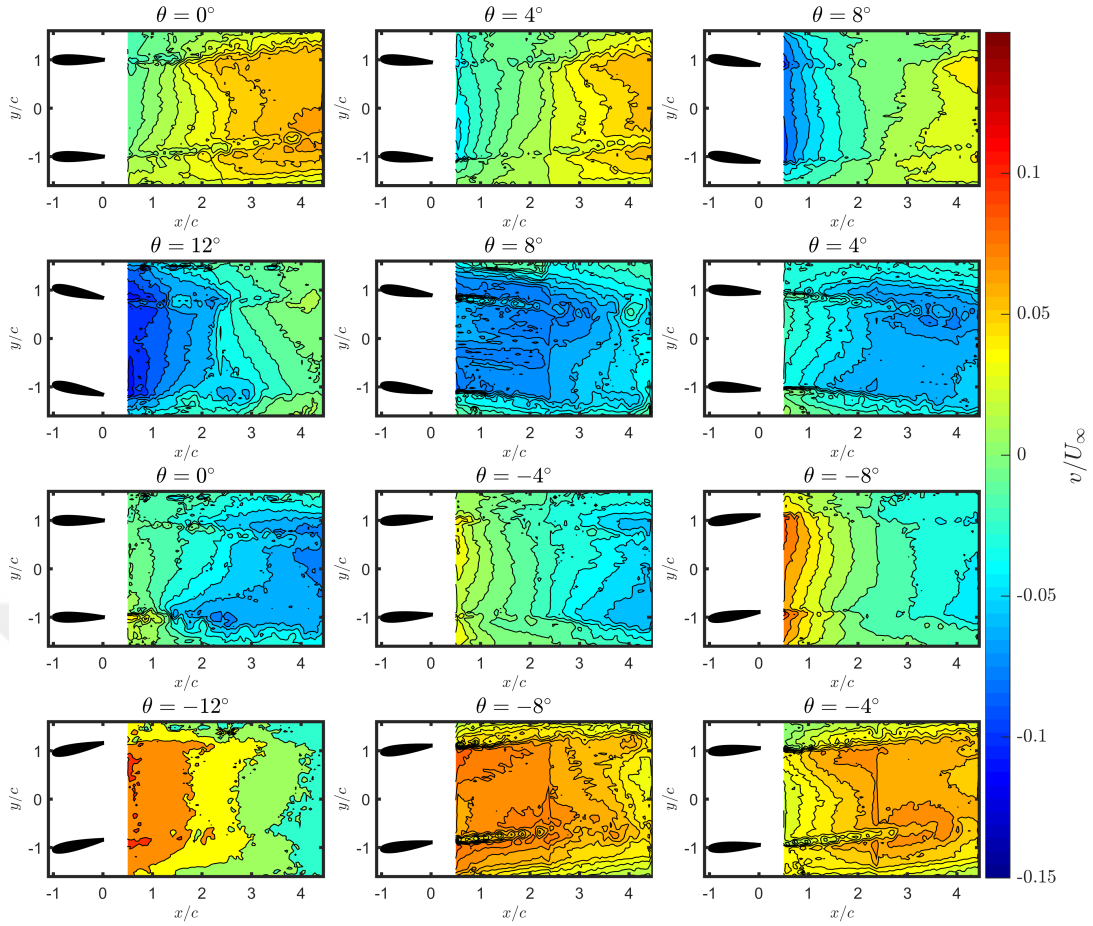


Figure A.17: PIV measurement results for the case $f = 10$ Hz, $U_\infty = 15$ m/s, $d = 2c$ $\bar{\theta} = 12°$. Variation of transverse velocity component.

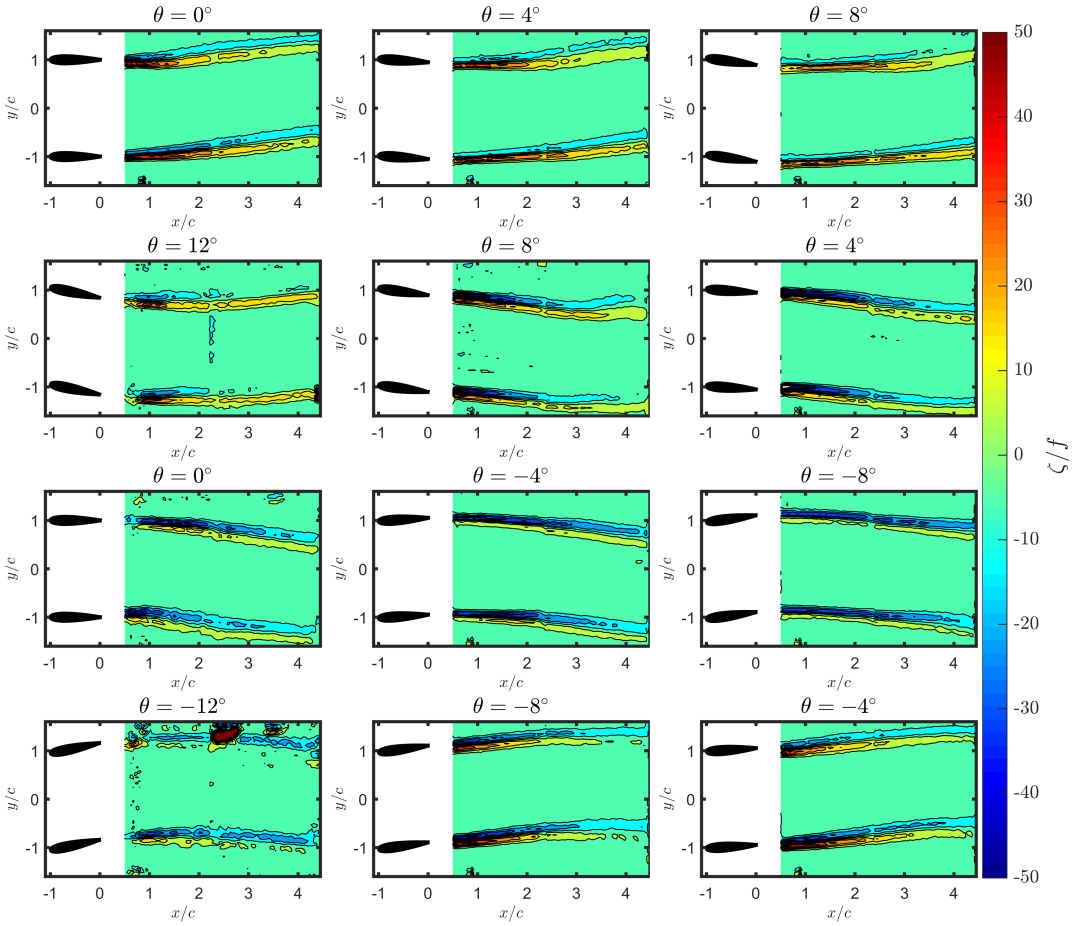


Figure A.18: PIV measurement results for the case $f = 10$ Hz, $U_\infty = 15$ m/s, $d = 2c$ $\bar{\theta} = 12°$. Variation of vorticity.

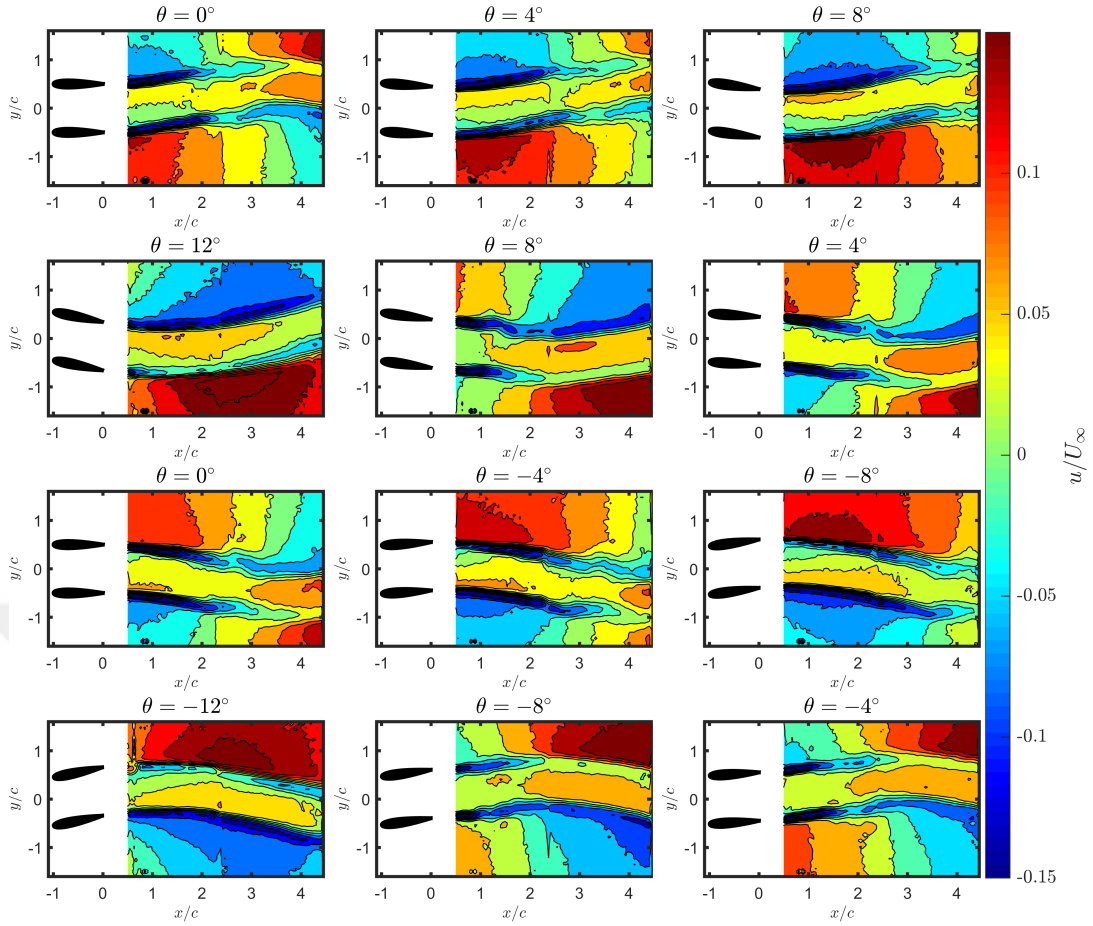


Figure A.19: PIV measurement results for the case $f = 10$ Hz, $U_\infty = 10$ m/s, $d = 1c$ $\bar{\theta} = 12°$. Variation of streamwise velocity component.

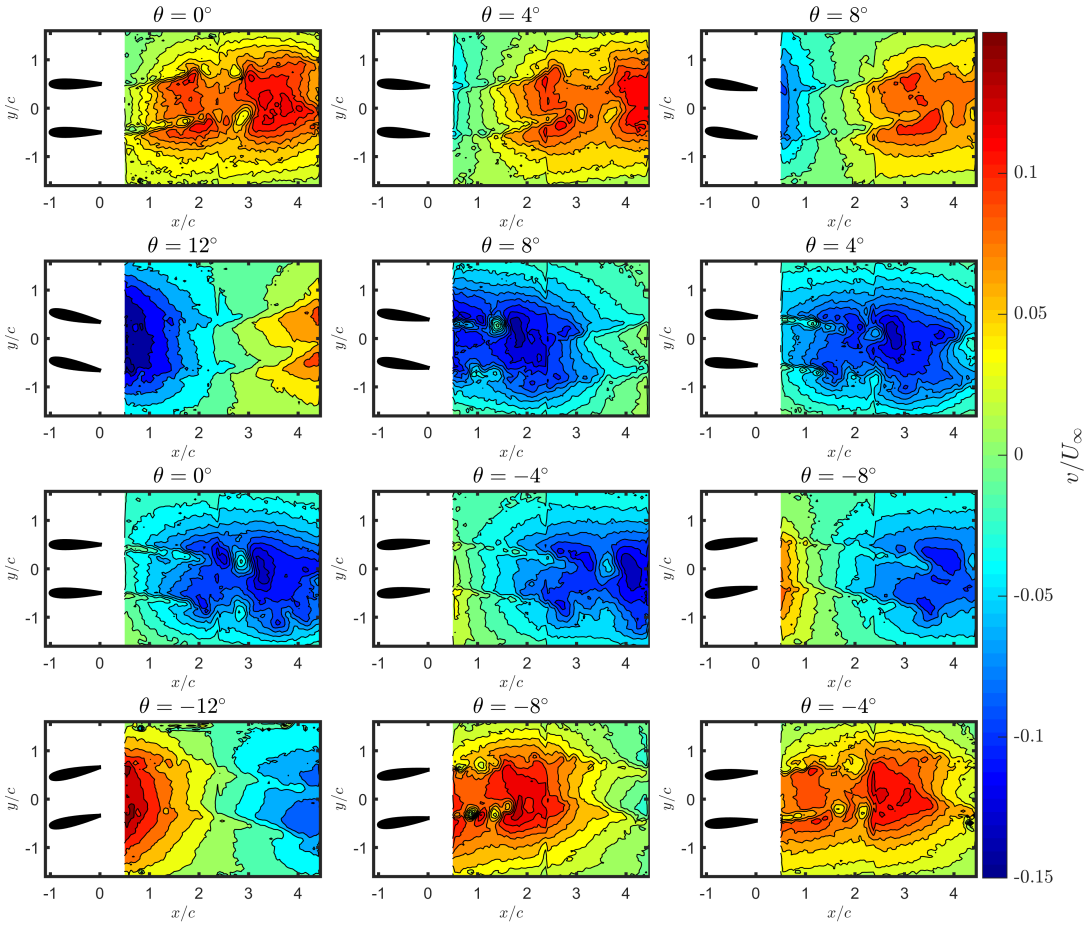


Figure A.20: PIV measurement results for the case $f = 10$ Hz, $U_\infty = 15$ m/s, $d = 1c$ $\bar{\theta} = 12°$. Variation of transverse velocity component.

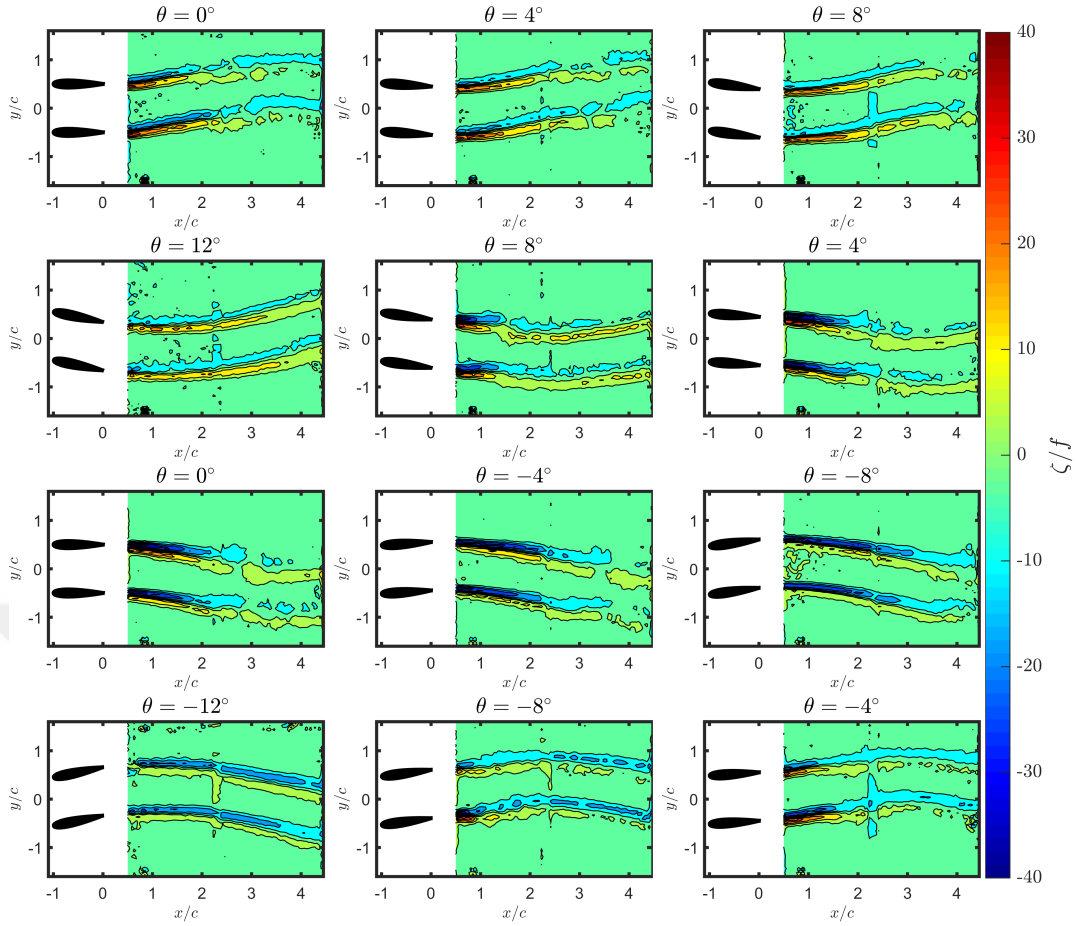


Figure A.21: PIV measurement results for the case $f = 10$ Hz, $U_\infty = 15$ m/s, $d = 1c$ $\bar{\theta} = 12°$. Variation of vorticity.

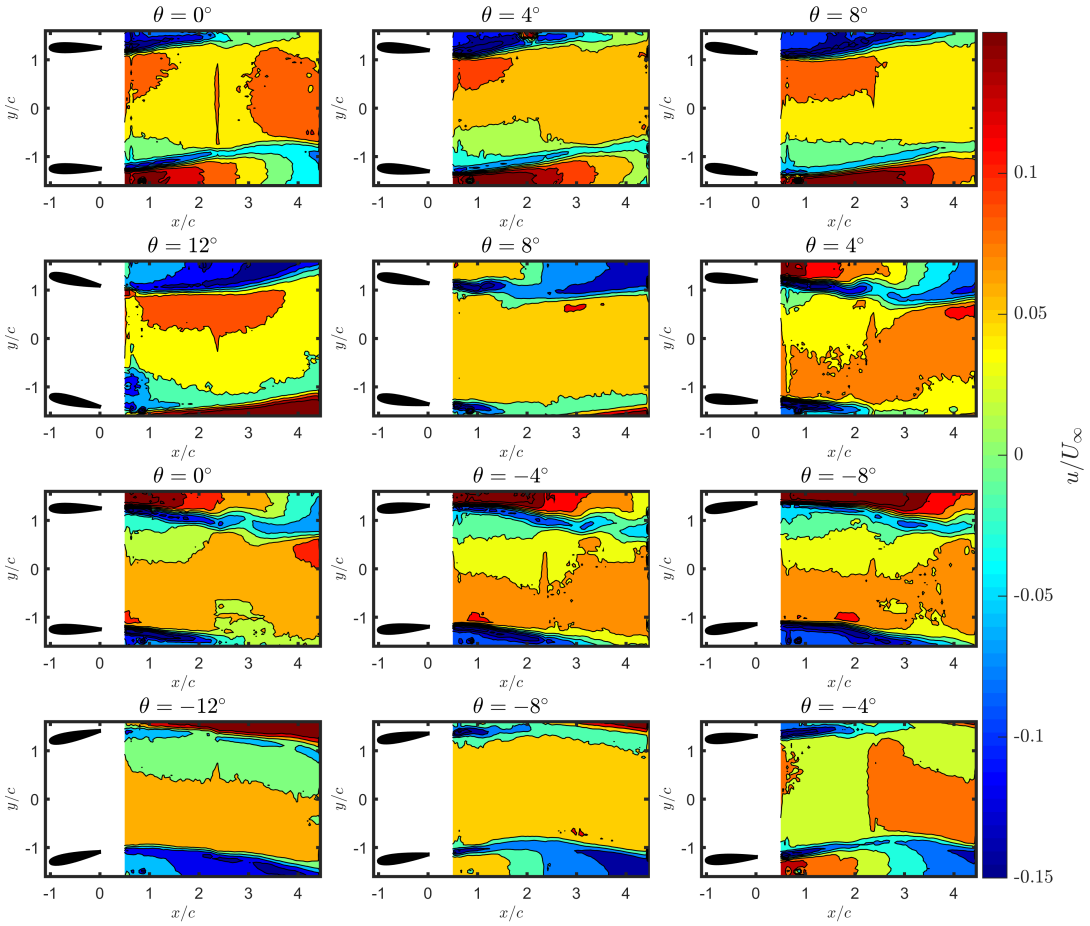


Figure A.22: PIV measurement results for the case $f = 10$ Hz, $U_\infty = 10$ m/s, $d = 2.5c$, $\bar{\theta} = 12°$. Variation of streamwise velocity component.

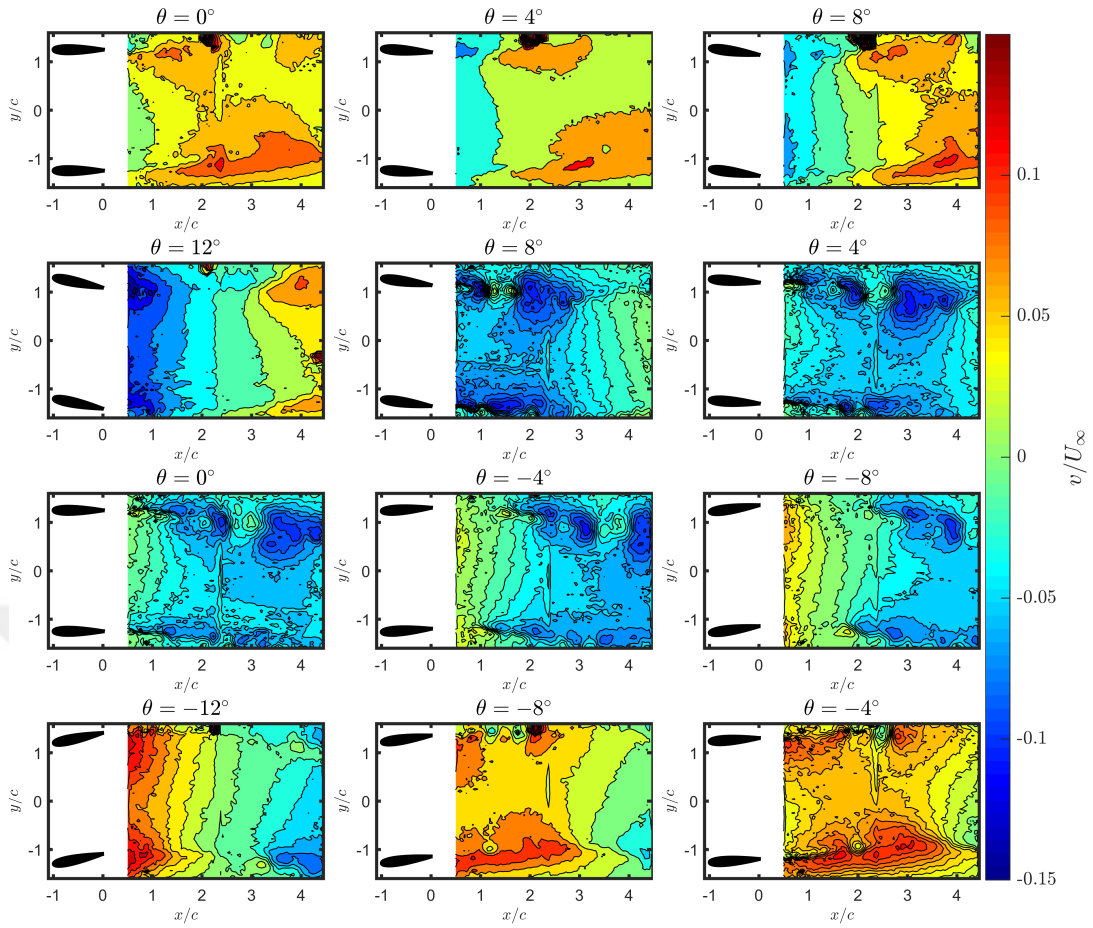


Figure A.23: PIV measurement results for the case $f = 10$ Hz, $U_\infty = 15$ m/s, $d = 2.5c$, $\bar{\theta} = 12°$. Variation of transverse velocity component.

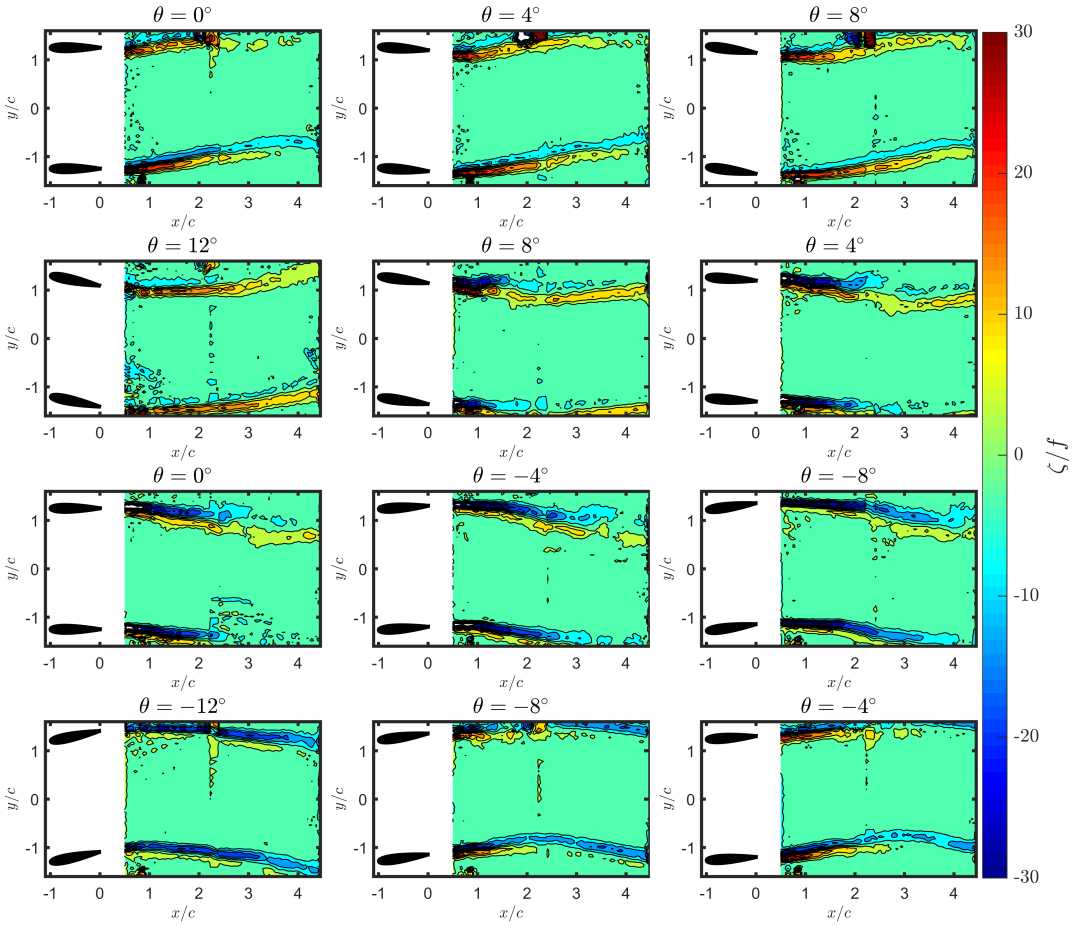


Figure A.24: PIV measurement results for the case $f = 10$ Hz, $U_\infty = 15$ m/s, $d = 2.5c$, $\bar{\theta} = 12°$. Variation of vorticity.

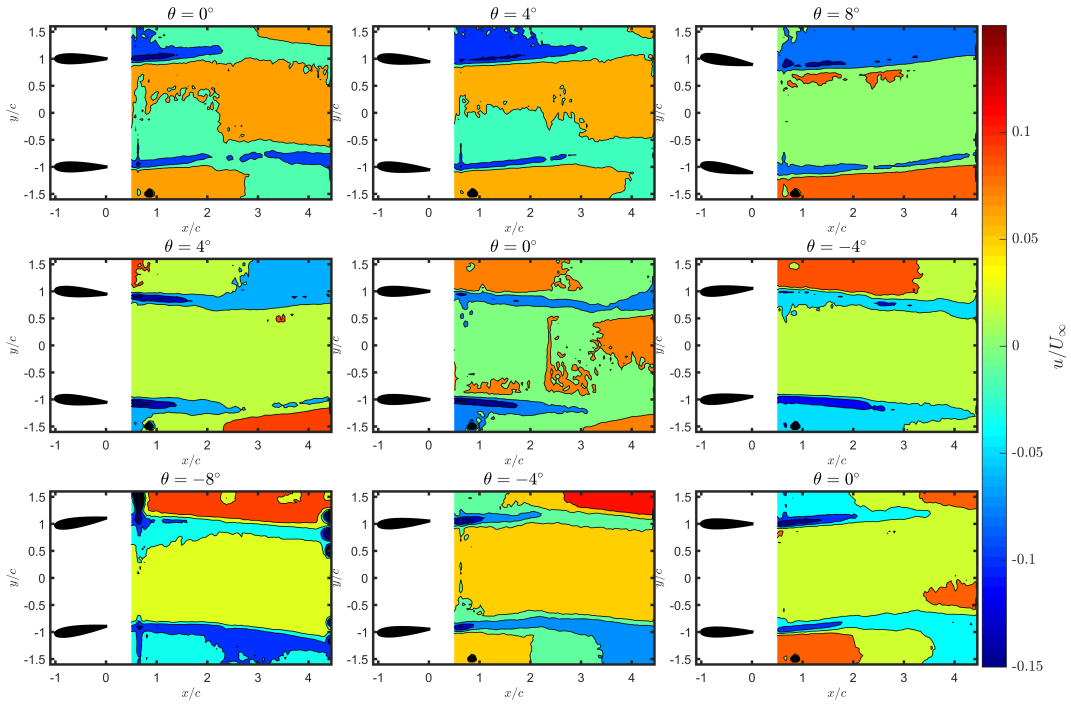


Figure A.25: PIV measurement results for the case $f = 10$ Hz, $U_\infty = 10$ m/s, $d = 2c$, $\bar{\theta} = 8°$. Variation of streamwise velocity component.

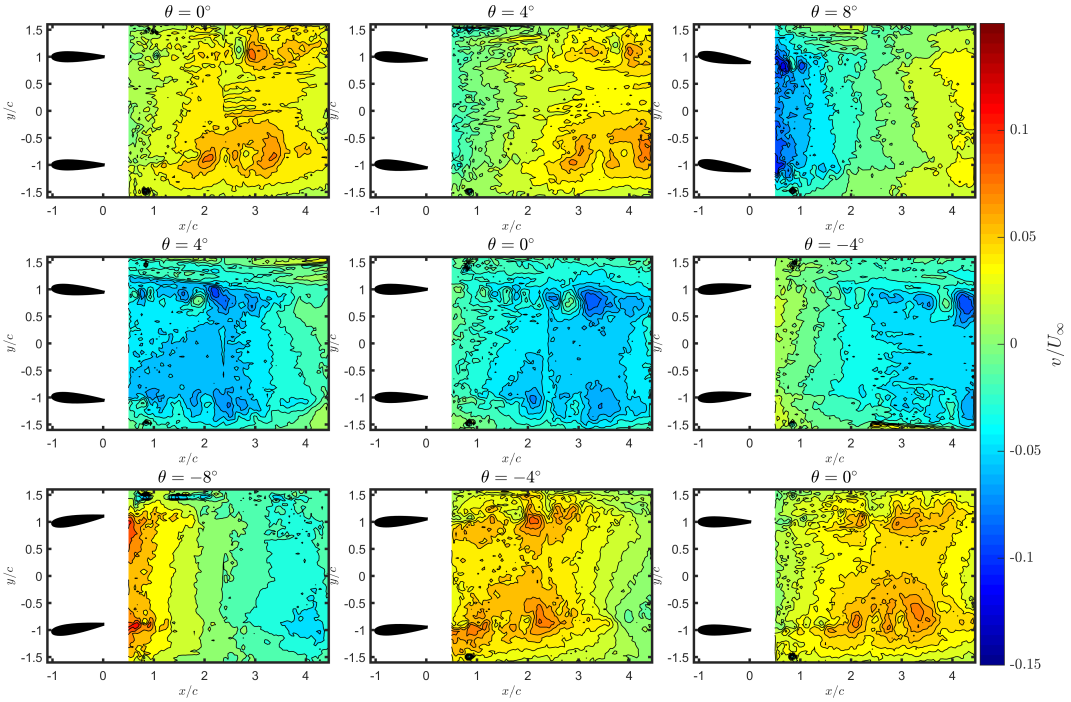


Figure A.26: PIV measurement results for the case $f = 10$ Hz, $U_\infty = 15$ m/s, $d = 2c$, $\bar{\theta} = 8°$. Variation of transverse velocity component.

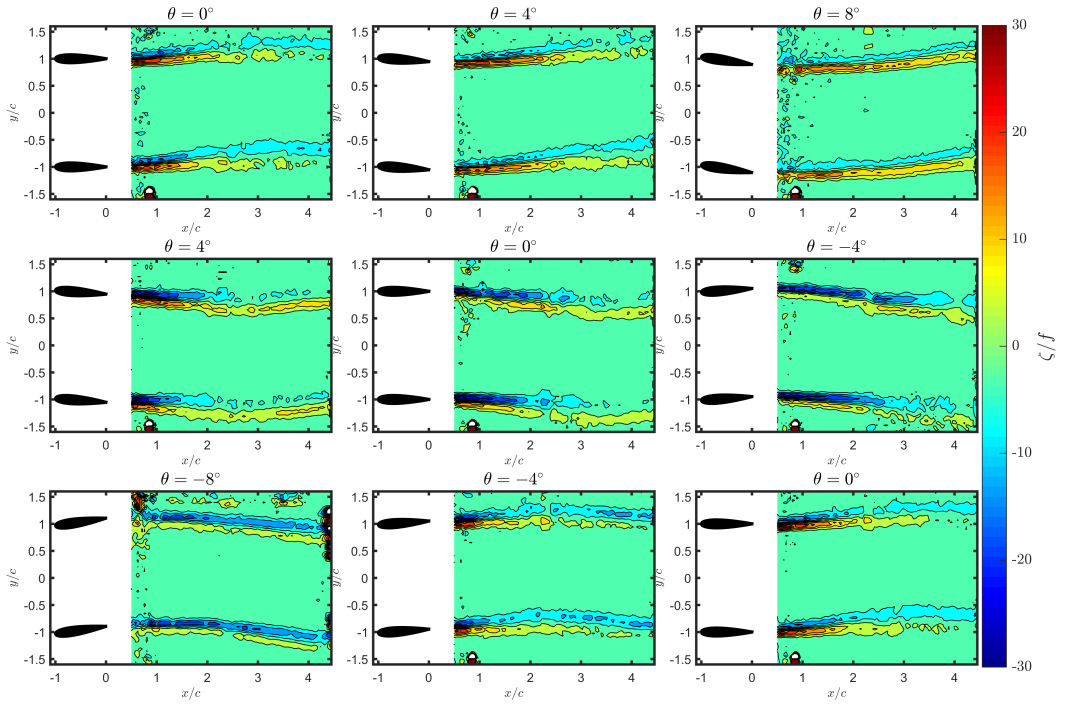


Figure A.27: PIV measurement results for the case $f = 10$ Hz, $U_\infty = 15$ m/s, $d = 2c$, $\bar{\theta} = 8°$. Variation of vorticity.

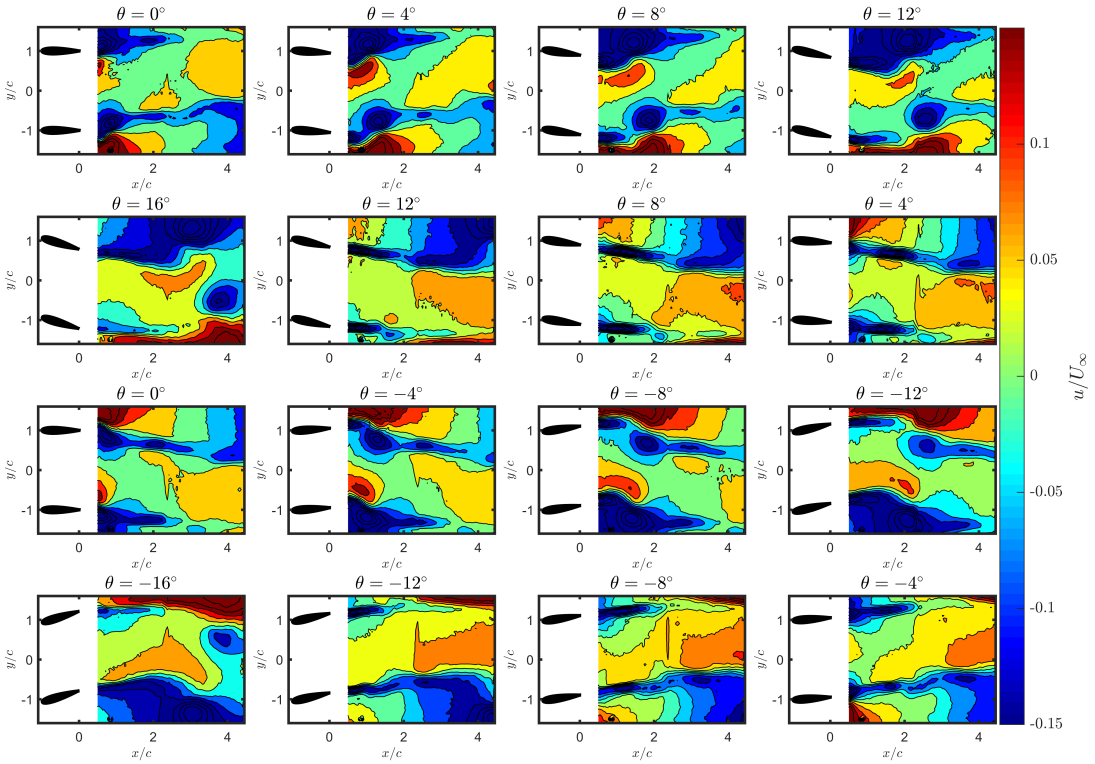


Figure A.28: PIV measurement results for the case $f = 10$ Hz, $U_\infty = 10$ m/s, $d = 2c$, $\bar{\theta} = 16°$. Variation of streamwise velocity component.

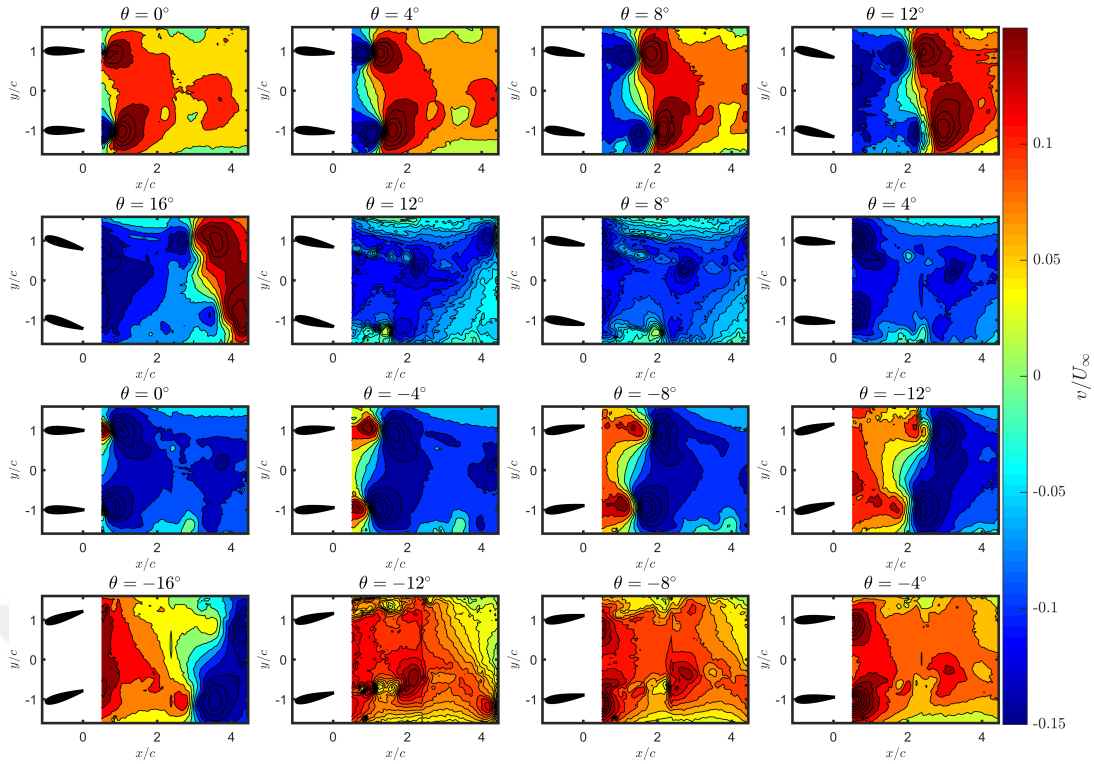


Figure A.29: PIV measurement results for the case $f = 10$ Hz, $U_\infty = 15$ m/s, $d = 2c$, $\bar{\theta} = 16°$. Variation of transverse velocity component.

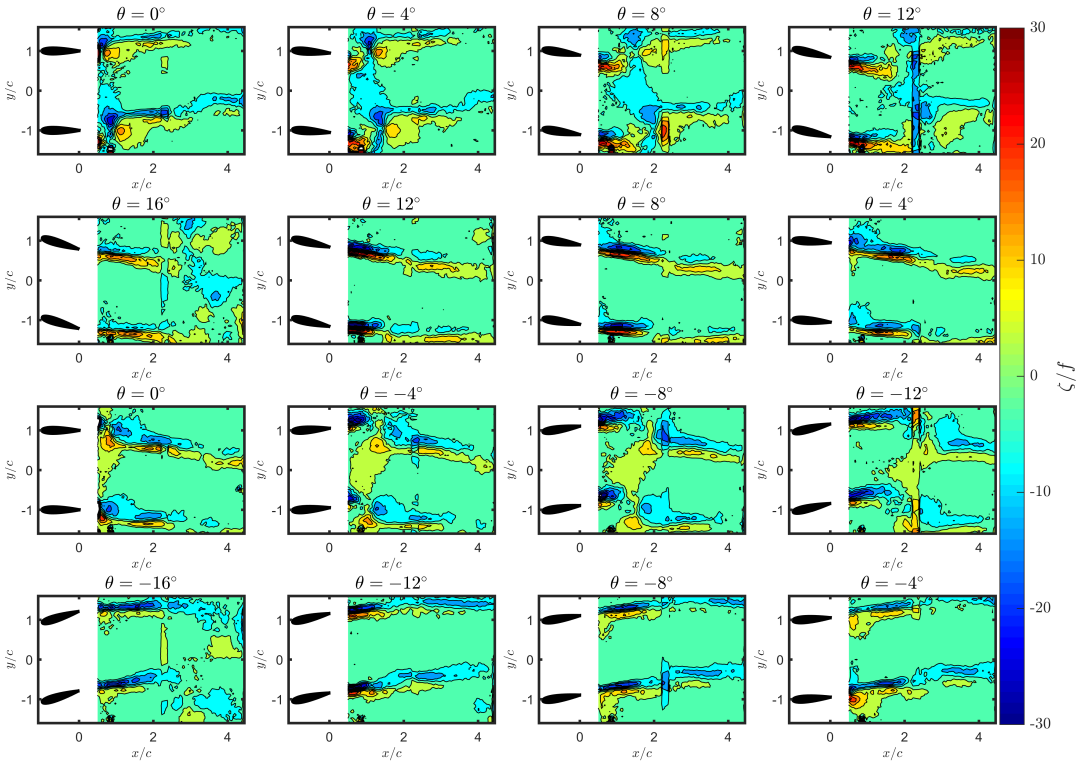


Figure A.30: PIV measurement results for the case $f = 10$ Hz, $U_\infty = 15$ m/s, $d = 2c$, $\bar{\theta} = 16°$. Variation of vorticity.

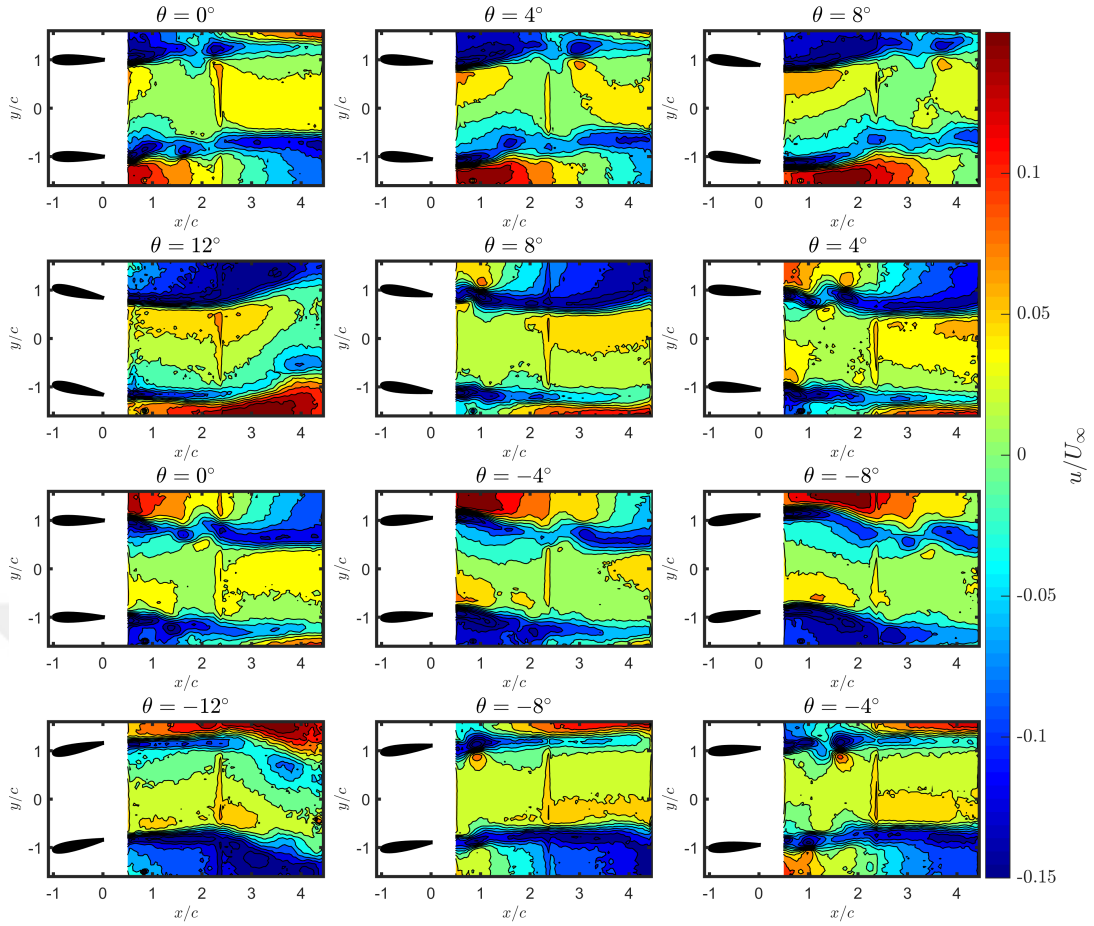


Figure A.31: PIV measurement results for the case $f = 5$ Hz, $U_\infty = 5$ m/s, $d = 2c$, $\bar{\theta} = 12°$. Variation of streamwise velocity component.

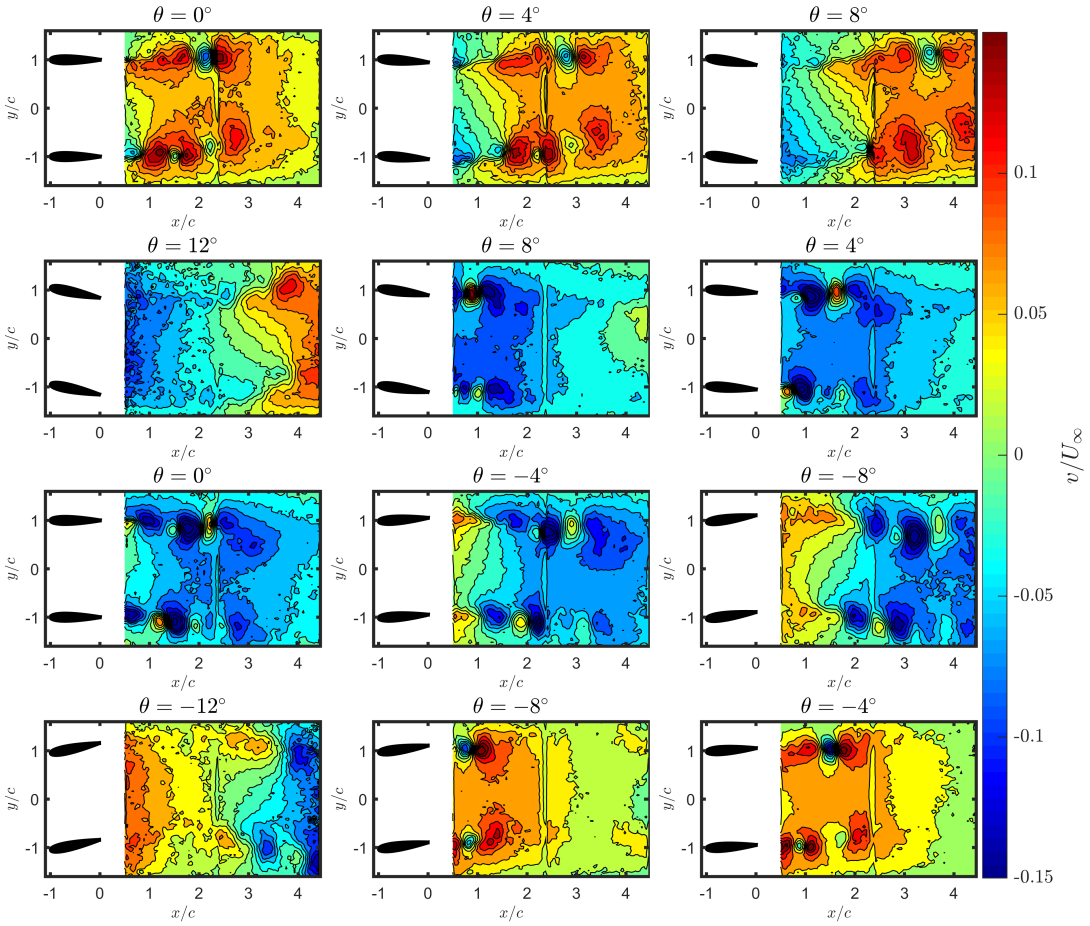


Figure A.32: PIV measurement results for the case $f = 5$ Hz, $U_\infty = 5$ m/s, $d = 2c$, $\bar{\theta} = 12°$. Variation of transverse velocity component.

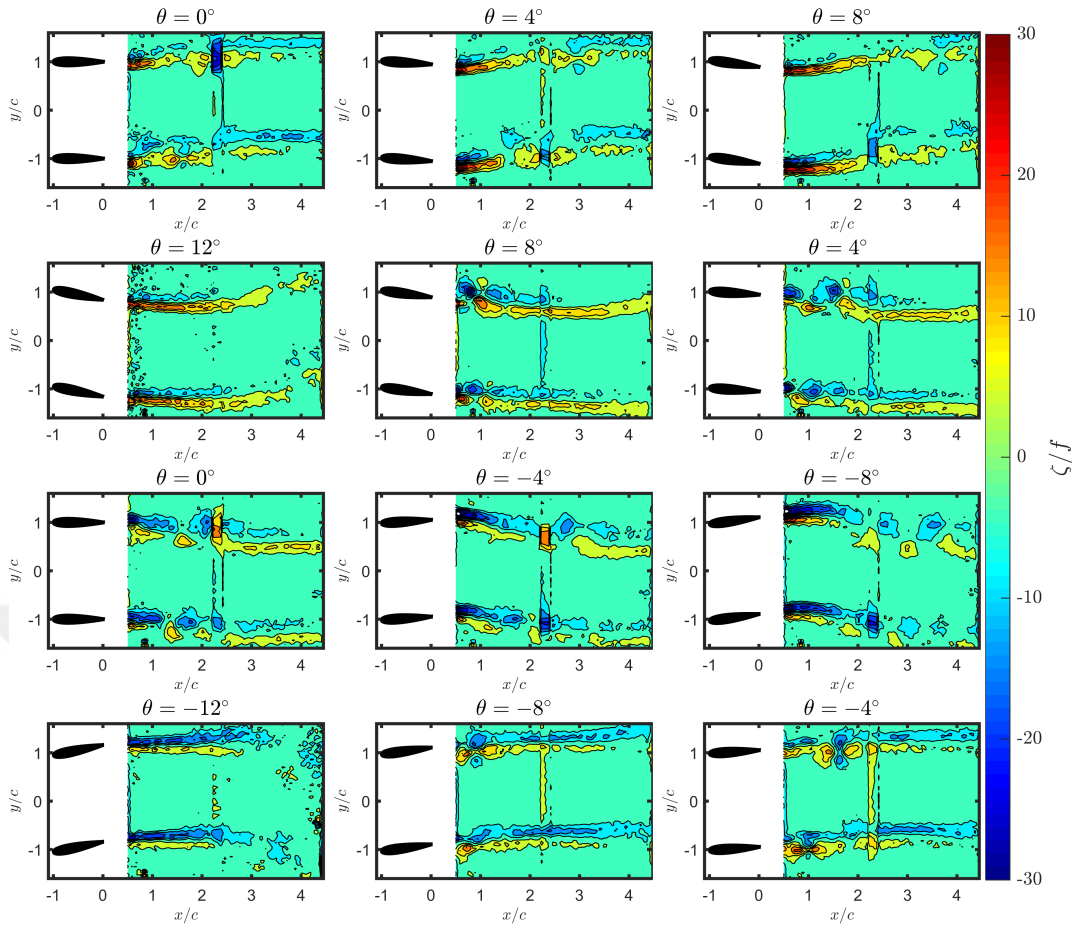


Figure A.33: PIV measurement results for the case $f = 5$ Hz, $U_\infty = 5$ m/s, $d = 2c$, $\bar{\theta} = 12°$. Variation of vorticity.